Microwave Antennas for Infrastructure Health Monitoring

Zahra Esmati

B.Sc. Electrical Engineering

A thesis submitted in fulfillment of the

requirements for the degree of

Master of Philosophy

WESTERN SYDNEY
UNIVERSITY
W

Centre for Infrastructure Engineering

School of Computing, Engineering and Mathematics

Western Sydney University, Australia

2017

Acknowledgments

Statement of Authentication

The work presented in this thesis is, to the best of my knowledge and belief, original except as acknowledged in the text. I hereby declare that I have not submitted this material, either in full or in part, for a degree at this or any other institution.

……………………………………………
(Signature)

……………………………………………
(Date)

Table of contents

List of tables

List of figures

List of abbreviations

IHM	Infrastructure Health Monitoring
WPT	Wireless power Transmission
WSNs	Wireless Sensor Networks
RFID	Radio Frequency Identification
GPS	Global Positioning System
AVA	Antipodal Vivaldi Antenna
CAVA	Conventional Antipodal Vivaldi Antenna
MAVA	Modified Antipodal Vivaldi Antenna
RAVA	Resonant Antipodal Vivaldi Antenna
EM	Electromagnetic
TSA	Tapered Slot Antenna
ISM	Industrial, Scientific and Medical
PNA	Performance Network Analyser
PCB	Printed Circuit Board
CST DS	Computer Simulation Technology Design Studio
CST MWS	Computer Simulation Technology Microwave Studio
PIFA	Planar Inverted-F Antenna
SD	Standard Deviation
GPR	Ground Penetrating Radar

Abstract

Infrastructure health monitoring (IHM) is a technology that has been developed for the detection and evaluation of changes that affect the performance of built infrastructure systems such as bridges and buildings. One of the employed methods for IHM is wireless sensors method which is based on sensors embedded in concrete or mounted on surface of structure during or after the construction to collect and report valuable monitoring data such as temperature, displacement, pressure, strain and moisture content, and information about defects such as cracks, voids, honeycombs, impact damages and delamination. The data and information can then be used to access the health of a structure during and/or after construction. Wireless embedded sensor technique is also a promising solution for decreasing the high installation and maintenance cost of the conventional wire based monitoring systems. However, several issues should be resolved at research and development stage in order to apply them widely in practice. One of these issues is that wireless sensors cannot operate for a long time due to limited lifetime of batteries. Once the sensors are embedded within a structure, they may not be easily accessible physically without damaging the structure.

The main aim of this research is to develop effective antennas for IHM applications such as detection of defects such as gaps representing cracks and delaminations, and wireless powering of embeddable sensors or recharging their batteries. For this purpose, modelling of antennas based on conventional antipodal Vivaldi antennas (CAVA) and parametric studies are performed using a computational tool CST Studio (Studio 2015) including CST Microwave Studio and CST Design Studio, and experimental measurements are conducted using a performance network analyser. Firstly, modified antipodal Vivaldi antenna (MAVA) at frequency range of

0.65 GHz – 6 GHz is designed and applied for numerical and experimental investigations of the reflection and transmission properties of concrete-based samples possessing air gap or rebars. The results of gap detection demonstrate ability of the developed MAVA for detection of air gaps and delivery of power to embeddable antennas and sensors placed at any depth inside 350-mm thick concrete samples. The investigation into the influence of rebars show that the rebar cell can act as a shield for microwaves if mesh period parameter is less than the electrical half wavelength. At higher frequencies of the frequency range, microwaves can penetrate through the reinforced concrete samples. These results are used for the investigating the transmission of microwaves at the single frequency of 2.45 GHz between the MAVA and a microstrip patch antenna embedded inside reinforced concrete samples at the location of the rebar cell. It is shown that -15 dB coupling between the antennas can be achieved for the samples with rebar cell parameters used in practice. Secondly, a relatively small and high-gain resonant antipodal Vivaldi antenna (RAVA) as a transmitting antenna and modified microstrip patch antenna as an embeddable receiving antenna are designed to operate at 2.45 GHz for powering the sensors or recharging their batteries embedded in reinforced concrete members. These members included reinforced dry and saturated concrete slabs and columns with different values of mesh period of rebars and steel ratio, respectively. Parametric study on the most critical parameters, which affect electromagnetic (EM) wave propagation in these members, is performed. It is shown that there is a critical value of mesh period of rebars with respect to reflection and transmission properties of the slabs, which is related to a half wavelength in concrete. The maximum coupling between antennas can be achieved at this value. The investigation into reinforced concrete columns demonstrates that polarisation configuration of the two-antenna setup with respect to

rebars and steel ratios as well as losses in concrete are important parameters. It is observed that the coupling between the antennas reduces faster by increasing the value of steel ratio in parallel than in vertical configuration due to the increase of the interaction between electromagnetic waves and the rebars. This effect is more pronounced in the saturated than in dry reinforced concrete columns.

Finally, a relatively high gain 4-element RAVA array with a Wilkinson power divider, feeding network and an embeddable rectenna consisting of the microstrip patch antenna and a rectified circuit are developed. Two wireless power transmission systems, one with a single RAVA and another with the RAVA array, are designed for recharging batteries of sensors embedded inside reinforced concrete slabs and columns with different configurations and moisture content. Comparison between these systems shows that the DC output voltage for recharging commonly used batteries can be provided by the systems with the single RAVA and the system with the RAVA array at the distance between the transmitting antenna and the surface of reinforced concrete members of 0.12 m and 0.6 m, respectively, i.e. the distance achieved when the array is 5 times longer that the distance achieved with a single antenna.

Chapter 1 Introduction

1.1 Background

Infrastructure health monitoring (IHM) involves the use of sensing systems to monitor the performance of the structure and evaluate its health state (Chan & Thambiratnam 2011). For large-scale concrete structures such as bridges, buildings and dams, various methods and systems of IHM have been applied. One of such methods is based on using sensors buried in concrete or mounted on surface of the structure during or after the construction to collect and report valuable volumetric data related to the health of the structure during and/or after construction. For example, embedded sensors can collect data, such as, temperature, displacement, pressure, strain, humidity, and detect cracks and rebar corrosion (Jiang & Georgakopoulos 2012). Therefore, embedded sensors are more suitable for many IHM applications. However, these sensors are connected through wires to a central station to collect and report data. The installation of wires represents up to 25% of the total system cost with over 75% of the installation time (Bernhard et al. 2003). Also, the wires restrict the sensors performance since if the wires get corroded during or after construction then these sensors become inoperative. Wireless sensors which communicate wirelessly as well as receive power remotely without being connected to any wires are one of the promising solutions to provide reliable operation and minimum installation cost. However, powering wireless embedded sensors presents an important and challenging problem since the wireless sensors cannot be used for a long time due to limited life time of batteries. It is impossible to change the batteries of the embedded sensors without damaging the structure. Therefore, new effective wireless powering methods, which can charge

rechargeable batteries wirelessly or can provide connection with passive wireless sensors for communication, are in demand.

1.2 Research aims and objectives

The main aim of this research is to develop antennas for IHM applications such as detection of defects and wireless powering of embeddable sensors or recharging their batteries. The challenge of developing and applying microwave techniques including antennas for IHM is their dependency on electromagnetic properties of structure materials in terms of the operating frequency and performance. Therefore, the objectives of this research are as follows:

* ❖ Design a modified antipodal Vivaldi antenna operating at three frequency bands of the Industrial, Scientific and Medical band with improved gain at low frequencies;

* ❖ Investigate the reflection and transmission properties of concrete-based samples possessing air gap or rebars;

* ❖ Design a relatively small and high-gain resonant antipodal Vivaldi antenna and a modified embeddable microstrip patch antenna as a transmitting antenna and receiving antenna, respectively, for wireless power transmission in concrete structures;

* ❖ Investigate the transmission and reflection properties of reinforced concrete slab and column with different values of steel ratio and moisture content using the developed two-antenna setup.

* ❖ Design embeddable rectenna consisting of a microstrip patch antenna and a rectifier circuit satisfying requirements for recharging batteries of the

embedded sensors when using the developed resonant antipodal Vivaldi antenna as a transmitting antenna;

❖ Develop a resonant antipodal Vivaldi antenna array with improved gain and efficiency to be used as a relatively long-distance transmitting antenna.

❖ Provide a comparative investigation of wireless power transmission systems with the developed single antenna and antenna array for recharging batteries of sensors embedded in different reinforced concrete structures;

1.3 Thesis organisation

This thesis is organised into six chapters as follows:

Chapter 1 Introduction

A brief background of infrastructure health monitoring, the objectives, the outline of the thesis, and a list of publications based on this thesis are presented.

Chapter 2 Literature review

A comprehensive literature review on IHM techniques was performed. Mainly, different types of antennas used for IHM including WPT were reviewed.

Chapter 3 Modified antipodal Vivaldi antenna

A modified antipodal Vivaldi antenna are designed, fabricated and tested to be used for IHM techniques. The antenna is applied to investigate the reflection and transmission properties of concrete-based samples possessing air gap or rebars numerically and experimentally at frequency range of 0.65 GHz – 3.5 GHz.

Chapter 4 Resonant antipodal Vivaldi antenna for wireless power transfer in concrete

A relatively small and high-gain resonant antipodal Vivaldi as a transmitting antenna and a modified embeddable microstrip patch antenna as a receiving antenna are designed to operate at 2.45 GHz in a two-antenna setup for WPT in concrete members. The structural members included reinforced dry and saturated concrete slabs and columns with different values of mesh period of rebars and steel ratio, respectively. Coupling between the antennas with different concrete members is studied.

Chapter 5 Design of rectenna and RAVA array for recharging batteries of sensors embedded inside reinforced concrete

Two WPT systems with the RAVA for recharging batteries of sensors embedded inside reinforced concrete slabs and columns, with different configurations and moisture content are developed. Then, a relatively high-gain 4-element RAVA array along with Wilkinson power divider feeding network are also developed in order to increase the distance between a transmitting antenna and concrete surface.

Chapter 6 Conclusions and future work

Concluding remarks of the thesis and some possible suggestions for future works are provided in the final chapter.

1.4 List of publications

The following papers either published by or submitted to peer-reviewed journals or conference proceedings, and the award are the outcomes of this thesis to date:

1. Esmati, Z., Kharkovsky, S. and Samali, B., "Reflection and transmission of microwaves in reinforced concrete samples irradiated by modified antipodal

Vivaldi antenna", *IET Microwave Antennas and Propag*ation, revision submitted Nov. 2016, (under review).

2. Esmati, Z., Kharkovsky, S. and Samali, B. "Wireless power transmission inside reinforced concrete slab using a resonant antipodal Vivaldi antenna", 18th IEEE International Conference on Antennas Propagation in Wireless Communications (IEEE-APWC), September 19-23, 2016, Cairns, Australia.

3. Esmati, Z. and Kharkovsky, S. "Modified antipodal Vivaldi antenna for infrastructure health monitoring techniques," 15th IEEE International Conference on Ubiquitous Wireless Broadband (ICUWB 2015), October 4-7, 2015, Montreal, Canada.

Award:

Travel award: International conference on electromagnetics in advanced applications (ICEAA 2016) and IEEE-APS topical conference on antennas and propagation in wireless Communications (IEEE-APWC 2016), 19-23 September, 2016, Cairns, Australia.

Chapter 2 Literature review

2.1 Introduction

This chapter provides the literature review for this research. It begins with the introduction of infrastructure health monitoring (IHM), followed by the description of wireless sensor network technologies for IHM applications. Wireless powering methods such as resonant coupling, strong resonant coupling and electromagnetic radiation method are presented and compared. Overviews of different types of antennas, which have been performed to highlight research gaps in the development and application of effective antennas for IHM including WPT in concrete members, are presented.

2.2 Infrastructure health monitoring

Infrastructure health monitoring (IHM) is defined as the use of non-structural sensing system to monitor the performance of the structure and evaluate its health state (Chan & Thambiratnam 2011). Traditionally, visual inspections of structures were the most popular method for inspecting the health of structure which was performed by trained or experienced individuals. Over time, various non-destructive testing and evaluation (NDT/E) methods such as eddy current, ultra sound and other wave propagation based methods (de Medeiros et al. 2015) have been developed. Development of effective, automated damage diagnosis techniques using sensor technology has become one of the major requirements. Wireless Sensor Networks (WSNs) are natural candidates for IHM systems (Xu, N et al. 2004). They are utilised to detect the presence, location, severity, and consequence of damage in structure.

2.3 Wireless sensors network for IHM applications

Developing WSN represents effective and economically-viable solutions for a various applications such as industrial monitoring, medical monitoring, environmental monitoring, object tracking, fire forest detection and natural disaster prevention (Bhuiyan et al. 2015). Most of the available sensors which can be buried in concrete or mounted in surface of structure during or after the construction to collect and report valuable monitoring data such as temperature, displacement, pressure, strain, and humidity are operated by wire and cause practical limitations to be embedded into the structures (Deivasigamani et al. 2013). Wireless sensors can eliminate the wiring problem of the traditional IHM systems and reduce the maintenance costs associated with it (Wu, J et al. 2010). In addition, if the wires of sensors get corroded then these sensors become inoperative. Therefore, the features of the flexibility and the capability of self-organization of wireless sensors are the main motivation of using WSNs instead of the wired sensor networks in industry. Wireless monitoring systems for large structures can be categorised into the following two configurations (Wang, D-H & Liao 2006): (a) health monitoring systems with surface mounted wireless sensors and (b) IHM systems with wireless embedded sensors. First wireless embeddable sensor platform (WESP) and first installation of WESP devices in a bridge for detection of the corrosion of rebars in concrete is shown in Fig. 2.1. Moreover, the Stonecutters Bridge in Hong Kong has been monitored by more than 1500 wireless sensors mounted and embedded inside bridge as shown in Fig. 2.2. This IHM system constitutes the most rigorously monitored bridge in the world (Ni, Wong & Xia 2011).
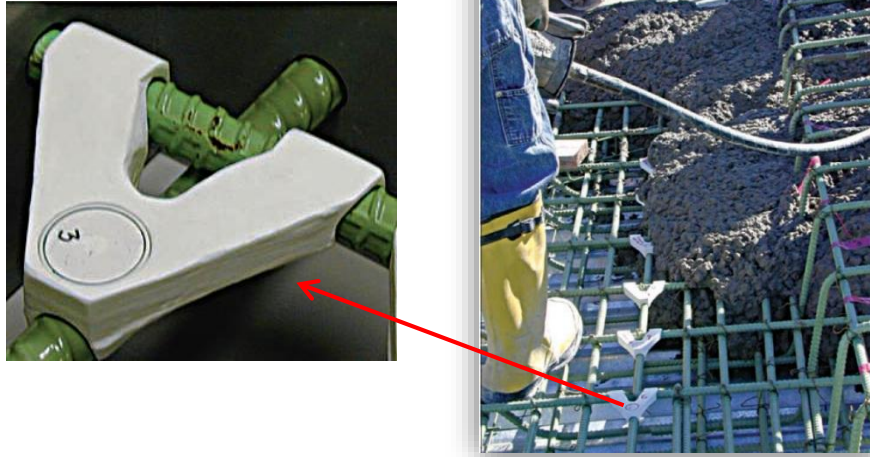
Figure 2. 1 Wireless embeddable sensor platform unit in holder mounted to rebar in bridge (Carkhuff & Cain 2003).
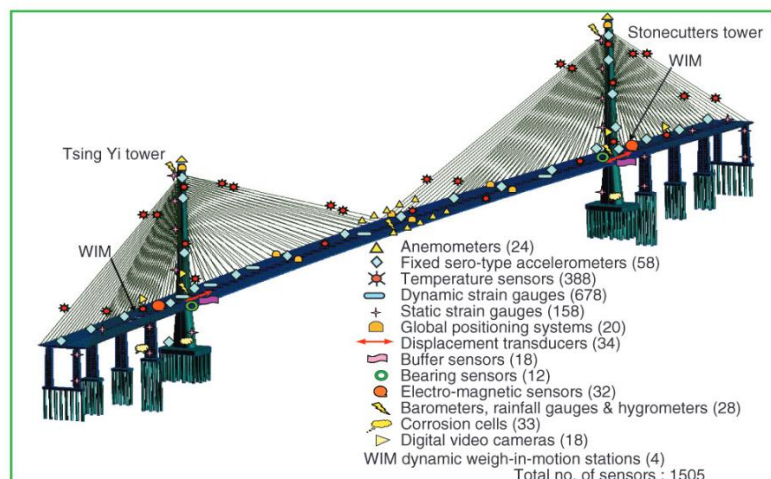
Figure 2. 2 IHM systems for Stonecutter bridges in Hong Kong (Ni, Wong & Xia 2011).

The advantages of the WSNs can be summarised as follows: they store a limited source of energy, eliminate the wiring problem of the traditional IHM systems and reduce the deployment time and cost, work efficiently under the harsh conditions, and it has deployment up to large scale (Bhattacharyya, Kim & Pal 2010). Therefore, wireless embedded sensor networks become a practical tool for IHM of large, complex civil structures (Kijewski-Correa, Haenggi & Antsaklis 2006).

8

Wireless embedded sensors monitoring systems represent many merits that can improve the construction industry. However, powering of the wireless sensors embedded inside concrete is a challenging problem since the batteries of the embedded sensors have a limited life-time. Replacement of the batteries of the sensors embedded inside concrete structure is difficult or even impossible without damaging the structure. Therefore, new effective wireless powering methods, which can charge rechargeable batteries wirelessly or can provide connection with passive wireless sensors for communication, need to be developed.

2.4 Wireless powering methods

Various wireless powering methods have been proposed previously and could be categorised into two types: (a) power scavenging from ambient energy sources and (b) power receiving from certain power sources through WPT methods (Wu, K, Choudhury & Matsumoto 2013).

2.4.1 Power harvesting from ambient energy sources

Energy harvesting gained significant interest in recent years due to the widespread availability of inexpensive and low-power RF chipsets and microcontrollers that could form the core of a self-powered sensor system (Sazonov et al. 2009). Solar energy is one of the most popular technologies for powering remote sensor nodes. As an example, in (Raghunathan et al. 2005), the issues which is arising from solar energy harvesting is studied. Unfortunately, solar energy is not the best solution for supplement battery supplies of some sensors such as bridge sensors, which quite often need to be located in places with extremely low light intensities. Other energies

targeted for harvesting usually include energy of vibration (Daniel Tomicek 2013) and wind (Priya 2005). Piezoelectric energy harvesters rely on the piezoelectric effect in which charge is generated on an active material when mechanically stressed. For instance, (Sazonov et al. 2009) proposed a generator capable of achieving 12.5 mW power in the resonant mode with the frequency of excitation at 3.1 Hz, with 10 mm displacement of the moving mass, which is sufficient to charge a wireless sensor on a bridge. However, the positioning of the sensors is significantly restricted by the vibration level that could be achieved by the piezoelectric materials for power conversion. One of the a considerable disadvantage of the piezoelectric sensors is their inability to respond to static loads (Akbari 2014).

2.4.2 Wireless power transmission method

Studies on WPT started as early as a century ago. The first practical WPT system developed by Nikola Tesla in 1904 (Tesla 1904). WPT involves the transferring power from a power source to an electrical load without synthetic conductor, across an air gap. All the WPT systems need a transmitting antenna to send signals and a receiving antenna to receive the signals. Various methods utilised in WPT technology mainly rely on the distance between the transmitting and the receiving antennas, amount of transmitted power and operating frequency. WPT systems are mainly divided into three main categories; inductive coupling, magnetic resonant coupling and electromagnetic radiation.

Inductive coupling technology can transfer several tens of kW with high efficiency (higher than 90%). However, the magnetic field energy and coupling coefficient are rapidly attenuated with the increasing distance which is being limited to centimetres, even millimetres level, due to the loose coupling between the coils.

Magnetic resonant coupling attract more attention than inductive coupling since it can support longer transfer distance. Two factors will tend to restrict the maximum transfer distance for any magnetic-field-based near-field WPT: the mutual inductance between the transmitting coil and the receiving coil, and the parasitic resistance of the coils. In contrast to previous methods, electromagnetic radiation system can transfer the energy more than several tens of meters, but transmitting power is small.

In (Andringa et al. 2005), an embedded wireless corrosion sensor was developed using non-invasive techniques and inductive coupling method was used to charge sensor. The sensor embedded inside concrete involving receiving coil which is magnetically coupled to a reader which connected to a power source outside the concrete. In (Jonah & Georgakopoulos 2011), a coupling magnetic resonant method was used to power sensors embedded in concrete. The power transmission efficiency of approximately 59% and 5.3% was achieved when one coil in air was 10 cm from the air-to-concrete interface and another coil was embedded inside concrete within a 7.5 cm $\times$ 7.5 cm air box at depth of 10 cm and 40 cm, respectively. The results reported in (Jonah & Georgakopoulos 2011) show that this method can be utilised to power embedded sensors in concrete structures. However, the size of the air-box needs to be reduced, since such large air gap inside concrete structure may reduce the strength of structure. Also, the results illustrated, the bandwidth of the system is narrow and cause significantly reduction of its efficiency.

Similar to two previous methods, also some researches have been done using electromagnetic radiation method for WPT to sensors which will be detailed in following sections. The wireless energy transfer with electromagnetic radiation needs a transmitter antenna to transmit the electromagnetic waves and a receiver antenna with a DC rectifier to transform the received energy into DC electrical power.

Antennas are key components of WPT and play the main roles to transmit and receive energy. The following section will give a brief introduction to antenna principles and concrete dielectric properties, and then various antenna types used for IHM application will be discussed.

2.5 Antenna principles

To describe the performance of any antenna, definitions of various antenna parameters are essential (Balanis 2016). The most important parameters of any antenna include the radiation pattern, directivity, efficiency factor, gain, effective aperture, polarsation and the bandwidth (Balanis 2016; Volakis & Johnson 1755).

> **Radiation pattern**

The radiation pattern is the graphical representation of the radiation properties of the antenna as a function position (spherical coordinates) (Balanis 2016; Gilbert & Volakis 2007; Huang & Boyle 2008). The radiation pattern of antenna characterises how the antenna radiates energy out into space or how it receives energy.

Antenna patterns can be categorised to three types (Balanis 2016):

i.   Isotropic pattern: Antenna pattern which produced by an isotropic radiator, defined by uniform radiation in all directions. Antennas with isotropic radiation patterns don't exist in practice, but are sometimes discussed as a means of comparison with real antennas.

ii. Directional pattern: having the property of radiating or receiving electromagnetic waves more effectively in some directions than in others.

iii. Omnidirectional pattern: Antenna pattern which is non-directional in a given plane and radiate the same pattern all around the antenna in a complete 360 degrees pattern.

For a linearly polarised antenna, performance is often described in terms of its principal E- and H-plane patterns. The E-plane is defined as "the plane containing the electric field vector and the direction of maximum radiation," and the H-plane as "the plane containing the magnetic-field vector and the direction of maximum radiation." (Balanis 2016). The E-plane and H-plane radiation patterns are the most important patterns for an antenna (Huang & Boyle 2008). The 3D radiation pattern of an electrically short current element is illustrated in Fig. 2.3.
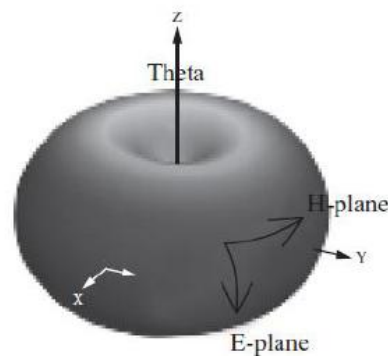
Figure 2.3 The 3D radiation pattern of an electrically short current element (Huang & Boyle 2008).

> **Directivity**

Antenna directivity in the IEEE Standard Definitions of Terms for Antennas (Balanis 2016; Gilbert & Volakis 2007) defined as:

"The ratio of the radiation intensity in a given direction from the antenna to the radiation intensity averaged over all directions. The average radiation intensity is equal to the total power radiated by the antenna divided by 4π. If the direction is not specified, the direction of the maximum radiation intensity is implied."

Directivity of antenna can be defined as the ratio of its radiation intensity in a given direction over that of an isotropic source (Balanis 2016) as can be calculated by following equation:

$$D = \frac{U}{U_0} = \frac{4\pi U}{P_{rad}}$$ (2.1)

where

D = directivity

U = radiation intensity (W/unit solid angle)

U_0 = radiation intensity of an isotropic source (W/unit solid angle)

P_{rad} = total radiated power by antenna (W)

➢ **Antenna efficiency**

Like other microwave components, antennas can suffer from losses. Antenna efficiency is used to consider losses at the input terminals and within the structure of the antenna which occurred because of reflection loss as a reason of mismatch between the transmission line and the antenna, and conduction and dielectric losses as shown in Fig. 2.4 (Balanis 2016).

Input terminals
(Gain reference)

Output terminals
(Directivity reference)

(a)

(b)
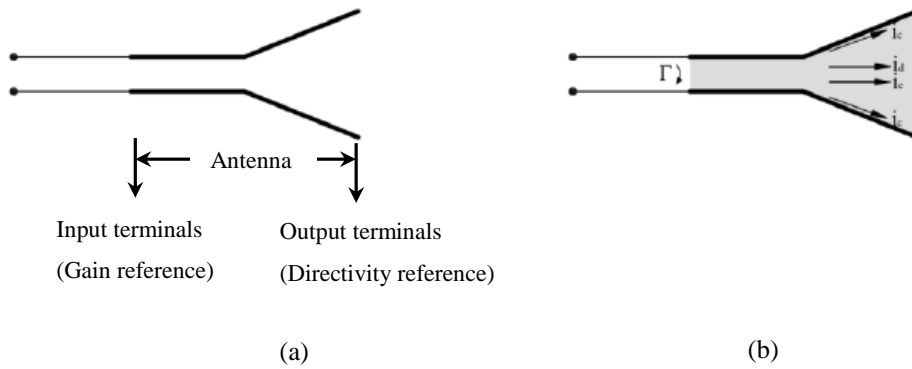
Figure 2.4 Reference terminals and losses of an antenna; (a) antenna reference terminals and (b) reflection, conduction and dielectric losses (Balanis 2016).

The total efficiency of antenna can defined by (Balanis 2016):

14

$$e_0 = e_r e_c e_d \tag{2.2}$$

where

e_0 = total efficiency (dimensionless)

e_r = reflection (mismatch) efficiency = $(1 - |\Gamma|^2)$ (dimensionless)

e_c = conduction efficiency (dimensionless)

e_d= dielectric efficiency (dimensionless)

Γ is voltage reflection coefficient at the input terminals of the antenna.

> **Gain**

Gain is another useful parameter for describing performance of an antenna. It defines the efficiency and the directional capabilities of antenna at the same time, against the directivity which only describes properties of the antenna (Balanis 2016; Huang & Boyle 2008). Gain of an antenna can be calculated using the following equation (Balanis 2016; Huang & Boyle 2008):

$$G = \frac{4\pi U}{P_{in}} \tag{2.3}$$

where

G = gain of antenna

U= radiation intensity (W/unit solid angle)

P_{in}= total input power accepted by the antenna (W)

The relationship between gain and directivity is defined as (Huang & Boyle 2008):

$$G = \frac{P_t}{P_{in}}D = \eta_e D \tag{2.4}$$

where

η_e= radiation efficiency factor of the antenna

P_t= total radiated power by antenna

15

➢ **Bandwidth**

The bandwidth of an antenna is defined as the range of frequencies within which the performance of the antenna, with respect to some characteristic (such as input impedance, pattern, beamwidth, polarsation, gain, beam direction, radiation efficiency), conforms to a specified standard (Balanis 2016). Different types of antennas have different bandwidth limitations. The bandwidth of antenna can be defined in terms of percentage of the centre frequency of the band:

$$BW = 100 \times \frac{F_H - F_L}{F_C} \qquad (2.5)$$

where

F_H = the highest frequency in the band

F_L = the lowest frequency in the band

F_C = the centre frequency in the band

➢ **Polarisation**

The polarisation of an antenna refers to the orientation of the electric field vector of the radiated wave (Kraus 1988). Depending on the current moves in the antenna there are three types of polarisation (Balanis 2016):

- Linear polarisation: the electric field of EM is confined to a single plane along the direction of propagation.

- Circular polarsation: It can be obtained when the magnitudes of the two linear components are the same but have a phase difference of $\pi/2$.

- Elliptical polarsation: It can be achieved when the combination of two linear components with different amplitudes and/or a phase difference that is not $\pi/2$.

➢ **Linear polarsation mismatch**

In order to maximise the transfer power between a transmitter and a receiver antenna, both antennas must align properly with same polarisation. When the antenna are misaligned or do not have the same polarisation, power reduction will happen which will reduce the overall system efficiency and performance.

When the transmitter and receiver antenna are linearly polarised, physical misalignment of antennas will cause polarisation mismatch loss which can be defined by (Balanis 2016):

$$\text{Polarsation mismatch loss (dB)} = 20 \log (\cos \theta) \qquad (2.6)$$

where

θ = the misalignment angle between antennas

2.6 Types of antennas

There are numerous types of antennas developed for many different applications; they can be classified into four groups.

➢ **Wire antennas**

Wire antennas, linear or curved, are some of the oldest, simplest, cheapest, and in many cases the most versatile for many applications (Balanis 2016). Wire antennas can include dipoles, loops, helical, sleeve dipoles, Yagi-Uda arrays and commonly have a low gain and operate at lower frequencies (HF to UHF) (Huang & Boyle 2008). Wire antennas are probably the most recognisable, as they are ubiquitous and typified by TV aerials, car aerials etc.

➤ Aperture antennas

Aperture antennas are most common at microwave frequencies (Balanis 2016; Huang & Boyle 2008). They may take the form of a waveguide or a horn whose aperture may be square, rectangular, circular, elliptical, or any other configuration (Balanis 2016; Bird 2016). The pattern has a narrow main beam which leads to high gain. For a fixed aperture size, the main beam pattern narrows down as frequency increases. These types of antennas are very useful in aerospace and spacecraft applications, because they can be flush mounted on the surface of the spacecraft or aircraft. Examples of these antennas include parabolic reflector, horn antennas, lenses antennas and Fabry–Pérot resonator antenna (Bird 2016; Huang & Boyle 2008).

➤ Microstrip antennas

Microstrip antennas received considerable attention starting in the 1970s, although the idea of a microstrip antenna can be traced to 1953 (Brown, J & Jull 1961). Microstrip antennas consist of a very thin metallic strip (patch) placed a small fraction of a wavelength above a ground plane. Microstrip antennas are low profile, simple and inexpensive to manufacture, conformable to planar and nonplanar surfaces, mechanically robust when mounted on rigid surfaces (Balanis 2016; Huang & Boyle 2008). Microstip antennas also have some disadvantages such as low efficiency, low power, high Q, poor polarsation purity, spurious feed radiation and very narrow frequency bandwidth which which limit their application in certain specified areas (Balanis 2016; Gilbert & Volakis 2007). Microstrip antennas can be divided into four basic categories (Singh & Tripathi 2011): microstrip patch antennas, microstrip dipoles, printed slot antennas and microstrip travelling-wave antennas. Microstrip antennas are spreading widely in all the fields and areas. For instance, microstrip patch antenna has been used for several applications such as mobile and satellite

communication, Global Positioning System (GPS), Radio Frequency Identification (RFID), radar, medical and rectenna application.

➢ **Array antennas**

Many applications require radiation characteristics that may not be achievable by a single element (Balanis 2016; Huang & Boyle 2008). Array antenna is a set of two or more antennas which are arranged in a regular structure to achieve improved performance over that of a single antenna. Element spacing and the relative amplitudes and phases of the element excitation determine the array's relative properties. Array antennas can be divided to four categories: Linear, circular, planar and conformal array. Typical elements in an array are dipoles, monopoles, slots in waveguides, open-ended antennas and microstrip radiators.

2.7 Concrete dielectric properties

Concrete is a composite material with changeable properties. The ingredients mixing ratio of concrete is variable and depends on the properties of ingredients and mix design. Concrete is prepared by mixing three basic ingredients such as cement, aggregates and water.

Every material has a unique set of EM properties affecting the way in which the material interacts with the electric and the electromagnetic fields of the EM waves. The dielectric material can be characterised by two independent electromagnetic properties namely, complex permittivity ε and the complex permeability μ^*. However, most common dielectric materials including concrete are nonmagnetic material, thus its complex permeability μ^* is almost equal to the permeability of free space ($\mu_0 =$

$4\pi \times 10^{-7}$ Henry/meter). Therefore, this research will focus on the effective complex permittivity which is defined as (Pozar 2012):

$$\epsilon = \left(\epsilon' - j\epsilon''_{eff}\right),$$

$$\epsilon = (\epsilon_o \epsilon_r - j\epsilon'' + \sigma/\omega) \text{ or}$$

$$\epsilon = \left(\epsilon_o \epsilon_r - j\epsilon_0 \epsilon''_r + \frac{\sigma}{\omega}\right), \tag{2.7}$$

where

$\epsilon' =$ real part of the effective complex permittivity

$\epsilon''_{eff} =$ imaginary part of the effective complex permittivity

$\epsilon_0 =$ permittivity of free space

$\epsilon_r =$ relative dielectric constant

$\epsilon'' =$ effective loss factor of the material

$\epsilon''_r =$ relative loss factor

$\sigma =$ conductivity of the material (S/m)

$\omega =$ angular frequency (radian).

The dielectric constant is a measure of how much energy from an external electric field is stored in a material. The imaginary part of the relative complex permittivity ε''_r is a measure of how dissipative or lossy a material is to an external electric field and is referred to the relative loss factor. The loss factor, ε''_r, is always > 0 and is usually smaller than ε'_r for dielectric materials (Buyukozturk 1997). The ratio of the energy lost to the energy stored in a material is given as loss tangent:

$$\tan \delta = \frac{\epsilon'' + \frac{\sigma}{\omega}}{\epsilon'} = \frac{\varepsilon''_r}{\varepsilon'_r}. \tag{2.8}$$

> ➤ **Velocity of the wave inside concrete**

In vacuum or air, EM waves travel at the velocity of light. The velocity is varied and specified by the medium through which the wave is propagating. Velocity of the waves within lossless material other than vacuum is lower than the velocity in free space as can be defined by (Shaari, Millard & Bungey 2004):

$$v = \frac{c}{\sqrt{\varepsilon'_r}} \tag{2.9}$$

where

v = the velocity of the wave inside material

c = the velocity of light in free space (3×10^8 m/sec)

> ➤ **Wavelength inside concrete**

The wavelength, λ, is a function of the oscillation frequency, f, and the wave velocity, which is determined by ε'_r of the medium as defined in Eq. 2.10:

$$\lambda = \frac{v}{f} =$$

$$= \frac{c}{f\sqrt{\varepsilon'_r}} \, . \tag{2.10}$$

In the lossy material effective wavelength can be defined by

$$\lambda_{eff} = \frac{c}{f\sqrt{\varepsilon_0(\varepsilon'_r - j\left(\varepsilon''_r + \frac{\sigma}{\varepsilon_0\omega}\right))}} \, . \tag{2.11}$$

> ➤ **Penetration depth in concrete**

Penetration depth is a measure of how deep light or any EM radiation can penetrate into a material. It is defined as a distance through a lossy dielectric over which the field strength falls by 1/e, where e is the natural logarithm constant, due to energy

absorption. For a given material, penetration depth will generally be a function of wavelength and it is defined as:

$$\delta_p = \frac{1}{\alpha} \qquad (2.12)$$

where the δ_p is penetration depth and α is attenuation. It determines the amplitude loss of the waves in a dielectric material and changes as a function of conductivity and real part of complex permittivity, which in term varies as frequency changes (Buyukozturk 1997). The attenuation can be defined as (Shaari, Millard & Bungey 2004):

$$\alpha = \left(\frac{\omega}{c}\right) \left[\left(\frac{\varepsilon_r'}{2}\right)\left(\sqrt{1 + \left(\frac{\varepsilon_r''}{\varepsilon_r'}\right)^2} - 1\right)\right]^{1/2} \qquad (2.13)$$

As can be seen from Eq. 2.13 the attenuation not only depends on ε_r' and ε_r'' of material, also depends on frequency ($\omega = 2\pi f$). Therefore, both of them should be consider at this case. It should be noted that higher moisture content has larger effective conductivity value. For example, as the moisture content of concrete increases from 0.2% to 12%, effective conductivity of concrete increases almost 20 times at 2 GHz. The increase of effective conductivity leads to more power losses.

2.8 Antennas for wireless power transmission to IHM sensors

Antenna is a key component of any WPT system. In recent years, wireless transmission techniques have been developed using different types of antennas. The block diagram of the WPT system is shown in Fig. 2.5. WPT using EM radiation method requires a transmitting antenna as a source of EM radiation; a rectenna consists of a receiving antenna with a rectifier to transform the microwave energy into DC electrical power. It is necessary to design antennas with high directivity and gain to meet the demands of WPT links. In addition, the transmitting and receiving antennas must be compact,

lightweight and characterised by a gain stability and low distortion. The slotted waveguide antenna (Goto 1990), microstrip patch antenna (Airani et al. 2016), parabolic dish antenna (Biswas et al. 2012; Hsin-Loug & Ta-Lun 2001) and tapered slot antennas (Nikolaou et al. 2005; Wang, Y et al. 2016) are the most popular type of transmitting antenna (Dhake & Dandavate 2012).
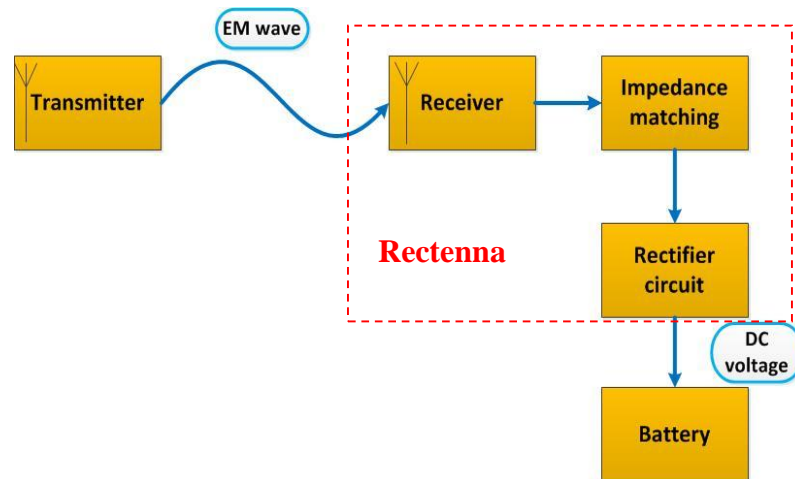
Figure 2.5 Functional block diagram of wireless power transmission.

➢ **Rectenna**

In the early of 1960s, the concept of rectenna (rectifying antenna), was conceived by W.C. Brown (Brown, WC 1980). Rectenna consists of a receiving antenna and rectifier circuit. It receives and converts microwave power to DC power. As a receiving terminal of the power transmission system, the rectenna is beneficial where power require to be delivered to a load through the space, where physical transmission lines are not feasible and also in applications where DC power needs to be distributed spatially. The power distribution is achieved by the dispersive nature of microwave energy in space, eliminating the need for physical interconnects to individual load elements (Epp et al. 2000). For instance, autonomous movement of the robots inside the pipes with energy supplied by microwaves in order to check the cracks (Shibata,

Sasaya & Kawahara 2001) and space power satellite (Han, Park & Itoh 2004a, 2004b) are another applications of the rectenna systems. Rectennas are highly efficient at converting microwave energy to electricity. In laboratory environments, efficiencies of over 85% have been observed. There are many kinds of rectennas with different configuration, as shown in Fig. 2.6.

(a)	(b)	(c)

(d)	(e)	(f)
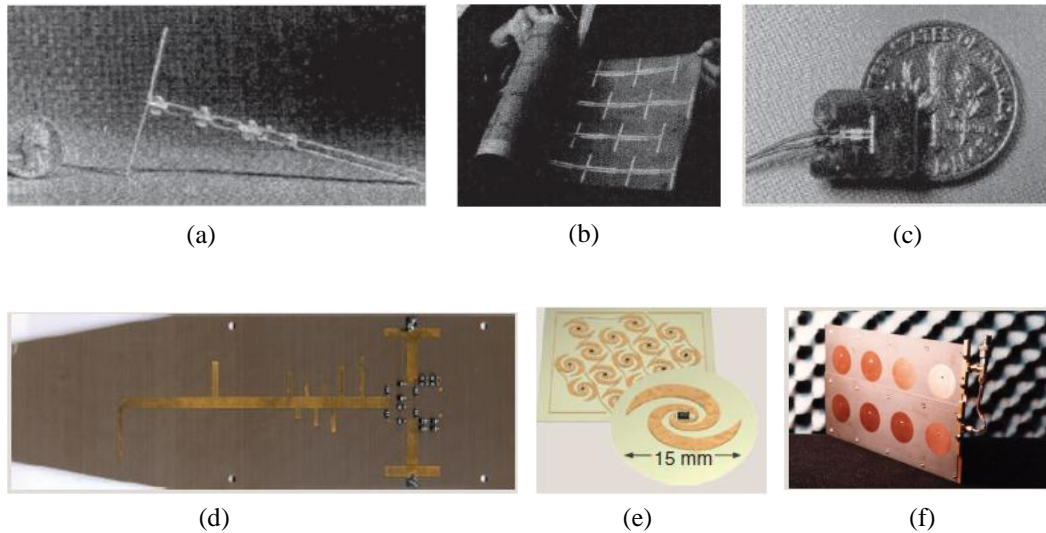
Figure 2.6 Various rectennas: (a) 2.45 GHz Brown's rectenna (Brown, WC 1976), (b) 2.45 GHz Brown's Thin-Film rectenna (Brown, WC 1986), (c) 35 GHz Texas A&M University's rectenna (McSpadden, Fan & Chang 1997), (d) 2.45 GHz Kyoto University's rectenna (Shinohara, N et al. 1998), (e) 8.5 GHz −12.2 GHz University of Colorado's rectenna (Hagerty et al. 2000), and (f) 2.45 GHz Hokkaido University's rectenna (Itoh, K 1984; Shinohara, Naoki 2011).

Lately, there are reports on powering the wireless sensors using rectennas (Ali, M, Yang, G & Dougal, R 2005; Zhang et al. 2014). The WPT by EM radiation method for IHM sensors was deployed in field experiments on the Alamosa Canyon Bridge in 2007 (Farinholt, Park & Farrar 2009). Since a directional antenna is most amenable for the transmitting and receiving antennas, both parabolic grid reflector and Yagi-type antennas with 15 dBi and 19 dBi gain, respectively, were used as a transmitting antenna in (Farinholt, Park & Farrar 2009) and Eighteen and 36 element microstrip patch antenna arrays were utilised as a receiving antennas as shown in Fig. 2.7(a). The sensor node could be charged to 3.6 V in 27 s when the power source is 1 W and 1.2

m away. This power level was sufficient to power two piezoelectric sensors and transmit data back to a base station on the bridge. The energy transmission equipment was mounted within the mobile host vehicle, as shown in Fig. 2.7(b). While in (Mascareñas et al. 2008) a 14.5 dBi Yagi antenna transmits 1W power at 2.5 GHz to a 19 dBi patch antenna 2 m away, in order to power the sensors mounted on the surface of Alamosa Canyon Bridge. The typical time for the 0.1F capacitor to be charged to 3.5 V is 95 s.
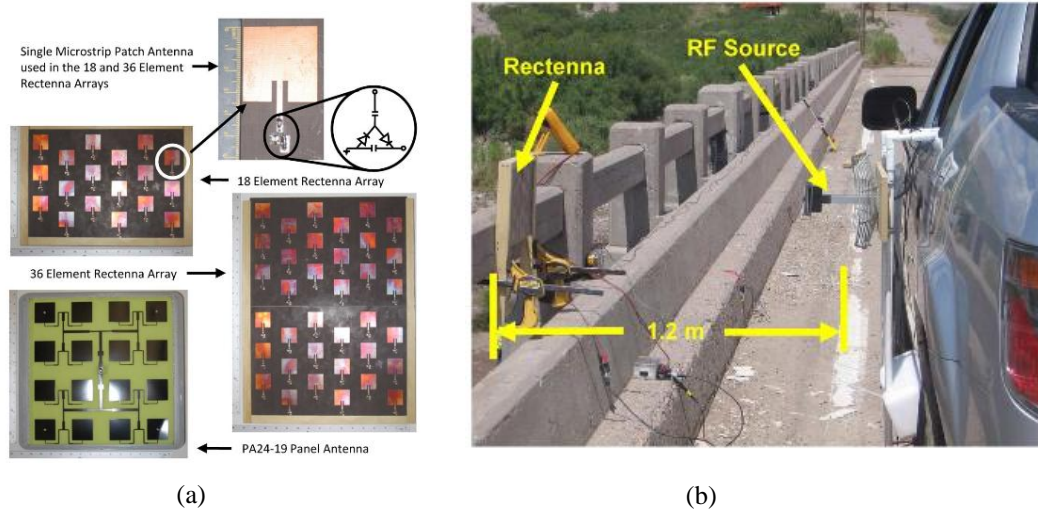
Figure 2.7 (a) Eighteen and 36 element rectenna arrays and (b) wireless energy delivery system tested on Alamosa Canyon Bridge, NM (Farinholt, Park & Farrar 2009).

The feasibility of sending wireless power to a buried rectenna within concrete was studied in (Shams & Ali 2007) using a 4×4 transmit patch antenna array with 13.6 dBi peak gain for operation at 5.7 GHz. The rectenna consisted of a stacked microstrip patch antenna as a receiving antenna and a half wave rectifier as a rectifying circuit, as shown in Fig. 2.8. Dry and wet concrete samples with various cover thicknesses and airgaps were considered in (Shams & Ali 2007), and maximum power of 10.37 mW was received at 0.6 m for input power of 7 W. However, by increasing the thickness and moisture of concrete the amount of received power was not sufficient for powering

an embedded sensor. Also, a U-slot microstrip patch antenna operating in the 2.4 GHz ISM frequency band embedded in concrete samples in (Bernhard et al. 2003) to develop a wireless embedded sensor system to monitor and assess corrosion in the tendons of prestressed concrete girders.
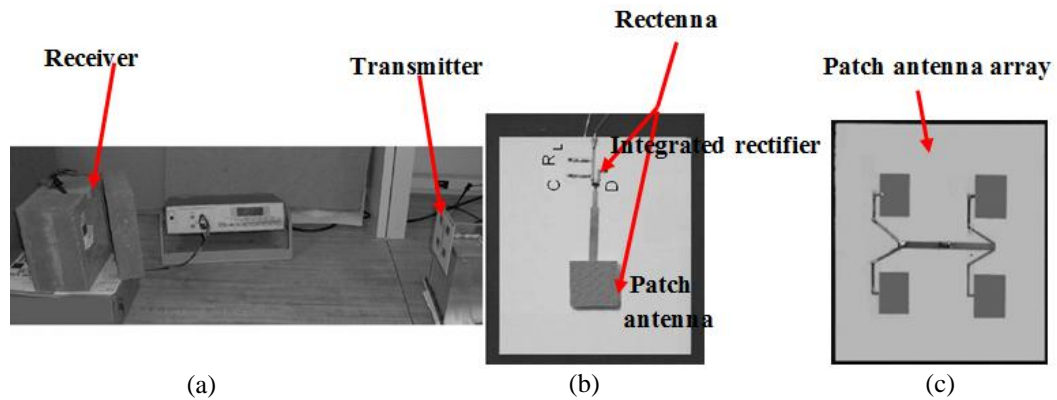
Figure 2.8 Photograph of (a) the WPT setup, (b) rectenna and (c) transmitting patch antenna array (Shams & Ali 2007).

A circularly polarised microstrip patch antenna is designed for WPT in (Ali, Mohammod, Yang, G & Dougal, R 2005) to operate as a rectenna working at 5.5 GHz for data telemetry in the 5.15 GHz - 5.35 GHz WLAN band. Moreover, the characteristics of an embedded microstrip patch antenna such as return loss, transmission loss, radiation pattern and gain within concrete was studied in (Shams, Ali & Miah 2006; Shams, Miah & Ali 2007) as function of an air gap and the dielectric property of a concrete at frequency of 2.45 GHz. As can be seen from Fig. 2.9, for efficient operation of the patch antenna inside concrete the air gap of $d = 15$ mm was required since the thickness of the concrete cover (D) has minimal effect on the resonant frequency of the embedded antenna. However, such air gap inside concrete may cause significant reduction of its durability. Increasing concrete cover cause gain enhancement of the embedded antenna since the concrete cover act as a superstrate. However, the enhancement of the gain due to superstate effect will be reduced by the

loss as concrete cover becomes thick. Also, the effect of concrete cover thickness on coupling between two patch antennas was investigated while antennas was tuned at 2.45 GHz as shown in Fig. 2.9(b). Experimental transmission characteristics illustrated that the attenuation superseded antenna gain improvement as concrete cover became thicker. Also, in (Salama & Kharkovsky 2013) the performance of the embedded patch antenna inside concrete and feasibility of proposed embedded antenna along with a rectifier circuit for a wireless microwave power transmission was investigated. In (Jin & Ali 2009), the return loss and transmission characteristics of two dipole antennas and planar inverted-F antennas (PIFA) inside a sample of a dry and saturated concrete bridge pier with two rebars were investigated. The antennas represented transmit receive system inside a cylindrical concrete pier of 400 mm height and 228 mm radius. Separation between the two antennas inside concrete pier is about 251 mm as shown in Fig. 2.10. The 915 MHz frequency band was selected because of its applicability to RFID technology. It was found that when dipoles and PIFAs antennas are located inside concrete, antennas had desired return loss characteristics. However, dipoles antennas did not function properly in concrete samples with rebars. In overall, PIFAs antennas represented better results in comparison with dipoles antennas embedded inside dry and saturated concrete pier (Jin & Ali 2009).

(a)

(b)
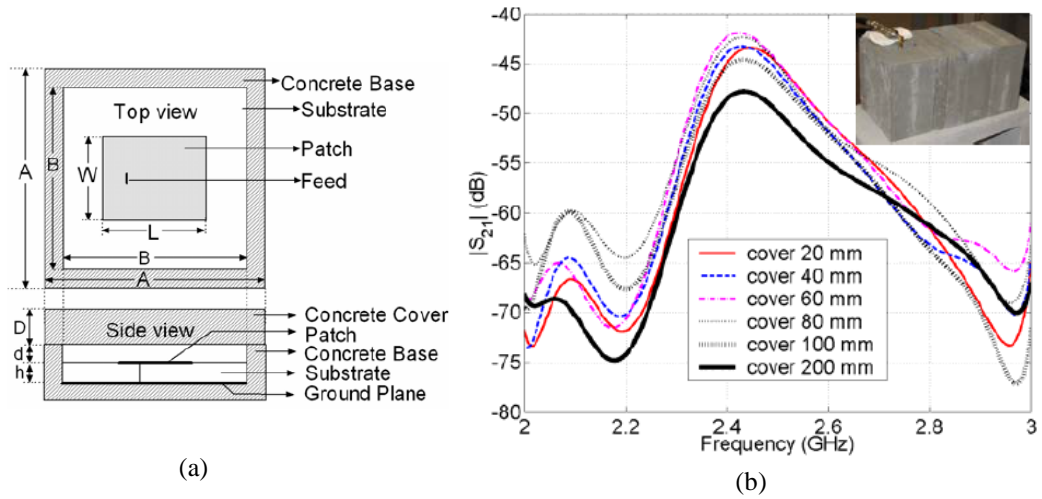
Figure 2.9 (a) Patch antenna inside concrete slab and (b) effect of concrete cover thickness on S_{21} (Shams, Miah & Ali 2007).

(a)

(b)

(c)
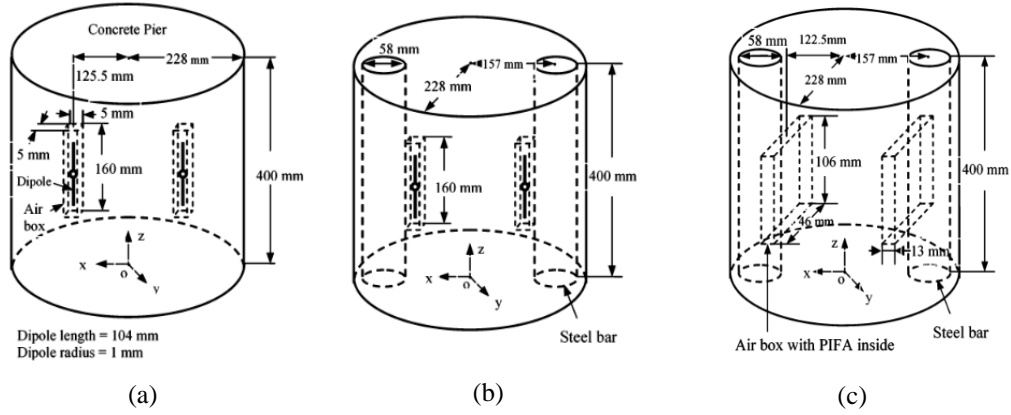
Figure 2.10 Vertical dipole antennas embedded (a) inside concrete, (b) inside reinforced concrete with steel rebars, and (c) location box of planar PIFAs adjacent to steel rebars (Jin & Ali 2009).

The return loss, gain, transmission loss and radiation patterns of a dipole, PIFA, a microstrip patch antenna and a loop antenna (see Fig. 2.11) are studied in (Jin & Ali 2010) at around 2.45 GHz while antennas are embedded in concrete pier. Either the PIFA or the patch will be good candidates to enable effective communication among embedded sensors themselves. Although the loop antenna demonstrated fairly good
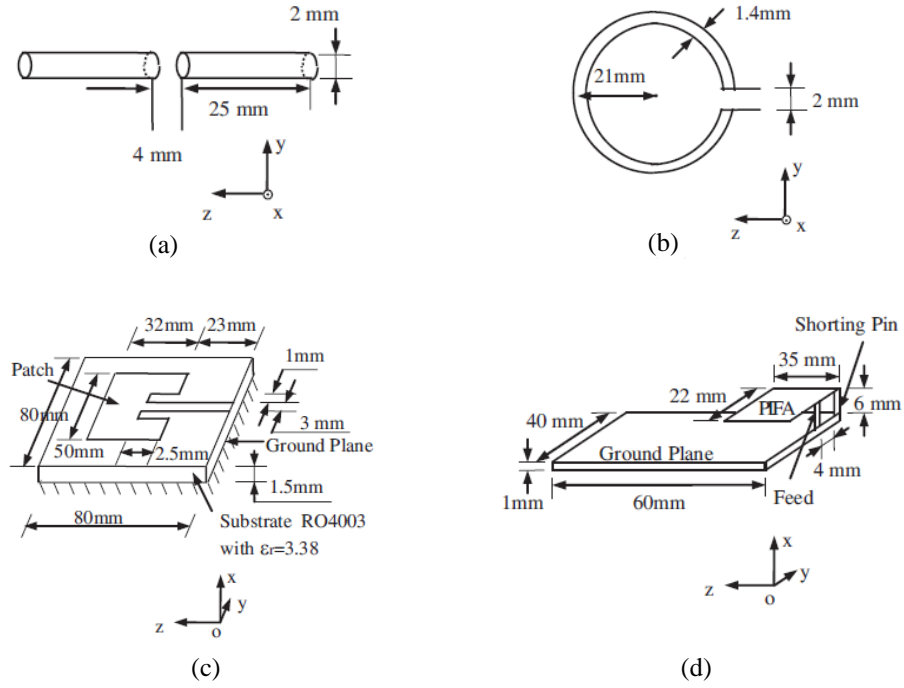
Figure 2.11 Geometrical dimensions of the (a) dipole, (b) loop, (c) microstrip patch, and (d) PIFA antennas under consideration (Jin & Ali 2010).

Performance, it required larger space in comparison with the other antennas and will degrade in performance as the number of embedded rebars increase inside concrete.

In (Jiang & Georgakopoulos 2010, 2012; Jiang, Georgakopoulos & Jin 2012; Jiang, Georgakopoulos & Jonah 2012) the optimisation of wireless powering of sensors embedded in concrete and the effects of reinforcing bars to RF power transfer are studied and analysed numerically. In (Jiang & Georgakopoulos 2010, 2012), transmission and propagation losses for normal and oblique incidences of electromagnetic plane waves on the air-to-concrete interface were numerically investigated. The analysis of results led to recognition of frequency range of 20 MHz - 80 MHz as an optimum one for wireless powering of sensors embedded in concrete and was validated through modelling and simulations of two dipole antennas coupling using full-wave electromagnetic formulation. However, one of the critical parameters of embedded antennas is their size. It is obvious that the embedded dipole used in (Jiang & Georgakopoulos 2010) was large and its application in practice is

questionable. In (Jiang & Georgakopoulos 2011; Jiang, Georgakopoulos & Jin 2012; Jiang, Georgakopoulos & Jonah 2012), the effects of reinforced bars on coupling between two patch antennas were investigated at three typical ISM frequencies and frequency of 915 MHz was recommended as an optimum frequency for WPT to sensors embedded in the reinforced concrete structures. However, experimental verification of these simulated results has not been provided in (Jiang & Georgakopoulos 2012; Jiang, Georgakopoulos & Jin 2012; Jiang, Georgakopoulos & Jonah 2012).

WPT is powering solution that has been widely used for powering wireless sensors. The powering system of sensors embedded in concrete includes air-to-concrete transmission paths and the power receivers are buried inside lossy media. Designing powering systems for embedded sensors is extremely challenging because of the environmental effects, reduced power transmission efficiency and compact size required. As the literature review demonstrates patch antenna is proven to be more suitable for powering sensors embedded in plain and reinforced concrete since they offer larger coupling and they are less sensitive to the changes of concrete's moisture conditions and rebars' configurations (Jiang & Georgakopoulos 2011). However, there are some disadvantages for patch antennas such as relatively narrow impedance bandwidth, low efficiency and low gain.

The requirement for wide operational bandwidth, higher gain and efficiency can be satisfied by travelling wave type antennas which belong to the category of endfire antennas (Waterhouse 2007). Tapered slot antenna (TSA) is one the prominent example of these types of antennas. It can offer an wide bandwidth and high directivity, and because of these features it is frequently utilised in ground penetrated radar, remote sensing, microwave imaging and ultra-wideband communications (Schaubert et al.

1985; Waterhouse 2007). TSA in comparison to traditional directional antennas such as ridged horn antenna (Bruns, Leuchtmann & Vahldieck 2003), log periodic antenna (Ro et al. 2014) and helical antenna (Milligan 2005) has the features of the planar structure, low profile, light weight and being directly integrated with radio frequency devices (Balanis 2016; Waterhouse 2007). TSA with exponentially tapered slot which also known as Vivaldi antenna was introduced by Gibson in 1979 (Gibson 1979) as shown in Fig. 2.12(a) . However, the lower and higher operational bandwidth of the Vivaldi antenna is restricted by the width of the antenna and transition structure from the microstrip to slotline, respectively. In order to improve bandwidth performance of the Vivaldi antenna, Antipodal Vivaldi antenna (AVA) was introduced by Gazit in 1988 (Gazit 1988) (see Fig. 2.12(b)).

(a)   (b)
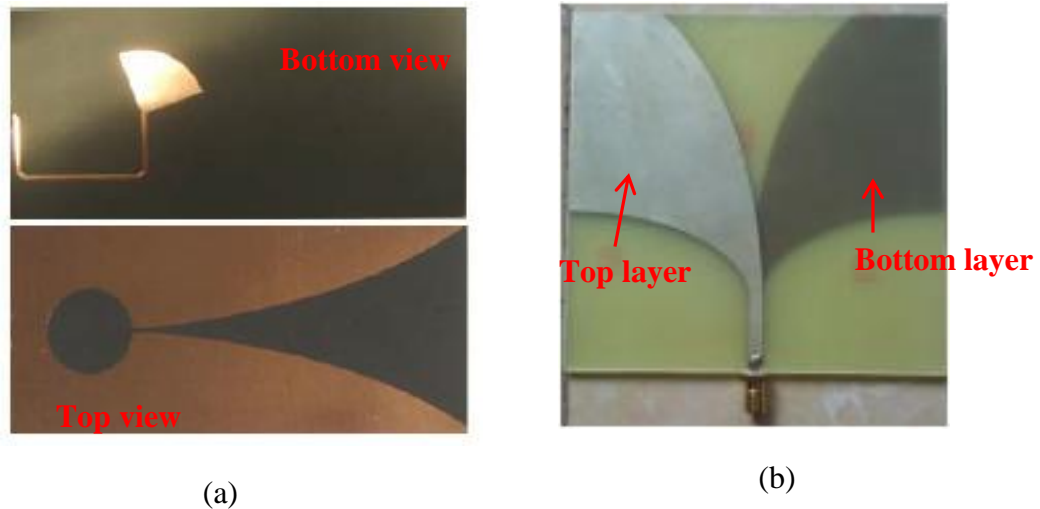
Figure 2.12 (a) Top and bottom view of Vivaldi antenna (Wang, Y & Fathy 2008) and (b) top view of antipodal Vivaldi antenna (Ba, Shirai & Ngoc 2014).

AVA has been developed for different applications in recent years. For instance, in (Li et al. 2016; Natarajan et al. 2016; Wang, Y et al. 2016), different techniques have been used to design AVA for UWB applications. In (Ruvio et al. 2012) the AVA for both sensing and data transmission has been used for pipe telemetry applications.

A novel technique for through the wall imaging using AVA aimed at the detection of stationary target is presented in (Fioranelli et al. 2015; Wang, Y & Fathy 2008; Yang, Wang & Fathy 2008). Moreover, UWB Vivaldi antennas can be used for detection of defects such as voids and cracks in concrete (Moosazadeh & Kharkovsky 2015; Wang, Z & Xie 2012). Also, it has attracted more attention in microwave imaging applications (Kanjaa et al. 2015; Moosazadeh, Kharkovsky & Case 2016; Shao & Adams 2016). AVA is a good candidate for designing an effective external antenna (i.e., transmitting antenna) since it can provide high gain, narrow beam width and broadband characteristics. Moreover, this type of the antenna can be designed to operate as a resonant antenna and/or an ultra-wide band traveling wave radiator at selected frequency ranges (Gibson 1979; Nassar & Weller 2015). For instance, for remote activation of an end device node of WSN, a 2.45 GHz rectenna consists of a Vivaldi antenna and an half wave voltage multiplier was proposed in (Congedo et al. 2013). However, Vivaldi antennas have not been used for WPT inside lossy materials for powering embedded sensors.

2.9 Summary

The literature review shows that our society depends heavily on infrastructure such as buildings, bridges and roadways. Unlike many of the disposable products of today's culture, the civil infrastructure has a lifetime measured in decades of years. Monitoring health of these systems presents unique challenges due to their large size, continuous exposure to the environment, infrequent inspection, and long design life. Many of these important structures are built using steel reinforced concrete. WSNs technologies have enabled the development of sensors that can be mounted on surface or embedded in structure to monitor the structural health of infrastructure. Such sensors can collect

and report valuable volumetric data related to the health of a structure during and/or after construction. However, these wireless sensors cannot be used for a long time due to limited life time of batteries. Therefore, in order to enable longer operational life of wireless embedded sensors, novel wireless powering methods, which can charge the sensor's rechargeable batteries wirelessly, need to be developed. Near field coupling, strongly coupled magnetic resonance and EM radiation methods were proposed for powering sensors embedded in concrete. However, these methods suffer from high losses, since the powering channel is established in heterogeneous media, i.e., concrete with air-to-concrete interface. The attenuation of power happens both at the air-to-concrete interface and inside concrete. Also, in practice, reinforcing bars are embedded in concrete to improve its mechanical stability, but very limited work has been done to analyse the effects of rebars on WPT to reinforced concrete. Different shape and size of reinforcing bars in concrete may significantly affect the efficiency of a receiving antenna. Due to these reasons, the mature technology for wireless communications in air does not provide equal benefits in the complex heterogeneous media case. Therefore, rigorous analysis of rebar effects is necessary for the development of optimum wireless powering systems for embedded sensors. Rectenna inside concrete should be able to receive sufficient power from a transmitting antenna. The antennas which are used for IHM must be directive, have relatively small dimensions, low profile and high efficiency.

Chapter 3 Modified antipodal Vivaldi antenna

3.1 Introduction

In recent publications, several AVAs have been presented with different techniques to improve the performance and bandwidth of the antenna associated with fabrication complexity and cost. In order to increase the gain and the radiation performance of antenna at lower frequency operating band, two pairs of slots and circularly shaped loads are loaded on the two elliptically shaped arms of antenna in (Wang, Z et al. 2016). A parasitic elliptical patch in the flare aperture is used in (Siddiqui et al. 2011) to improve the directivity of antenna. By using elliptical strip conductors described in (Ashraf et al. 2015; Siddiqui et al. 2011), the desired lower cutoff frequency has been achieved. It should be noted that ISM frequency band is very attractive for the investigation of concrete and for wireless powering of sensors embedded in concrete; however, most of the previously reported AVAs operating at ISM bands had a relatively low gain at lower frequencies. For instance, in (Siddiqui et al. 2011) the presented antenna covers the ISM bands, however, the gain of antenna is less than 2.5 dB at lower frequencies although the size of antenna is large.

In this chapter, firstly, a compact conventional AVA (CAVA) is designed and optimised with CST MWS. Secondly, to improve the bandwidth, gain and radiation patterns of the CAVA, a modified antipodal Vivaldi antenna (MAVA) with frequency range of 0.65 GHz - 6 GHz is designed to be used for IHM techniques. The proposed antenna offers high gain and directive radiation patterns at the operating frequency range. This frequency range includes three frequency bands of the Industrial, Scientific and Medical band (ISM band); namely, from 902 MHz to 928 MHz, 2.400 GHz to 2.4835 GHz and 5.725 GHz to 5.875 GHz. The feasibility of the designed antenna for

IHM is investigated by modelling a concrete block with an air gap representing a crack. Furthermore, a two-antenna setup including the MAVA as an external transmitting antenna, and a resonant microstrip patch antenna as a receiving antenna embedded in concrete have been developed to investigate into reflection and transmission of microwaves in reinforced concrete samples numerically and experimentally. Experimental measurements are conducted with an Agilent performance network analyser (PNA).

3.2 Design and performance of modified antipodal Vivaldi antenna

The geometry of the proposed CAVA is shown in Fig. 3.1(a). The designed antenna fed by a microstrip line with width of the W_f which is adjusted to be 1.53 mm in order to match 50-Ω. The antenna is designed on a Roger RT5880 substrate with thickness of 0.508 mm ($\varepsilon_r = 2.2$ and $\tan\delta = 0.0009$). The overall size of the presented antenna is 171×202 mm^2 which is approximately $0.5\lambda \times 0.6\lambda$, where λ is free-space wavelength at 0.9 GHz. In order to design the CAVA two symmetric elliptical tapered arms located on opposite sides of substrate are flared. The dimensions of inner and outer edges of the radiation flares can be determined by following equations:

$$a_1 = \frac{W_{sub} - W_f}{2} \tag{3.1}$$

$$b_1 = 5.713 \times a_1 \tag{3.2}$$

$$a_2 = a_1 - W_f \tag{3.3}$$

$$b_2 = 0.812 \times a_2 \tag{3.4}$$

where a_2, b_1 are major radii and a_1, b_2 are minor radii of four ellipses as shown in Fig. 3.1(a).
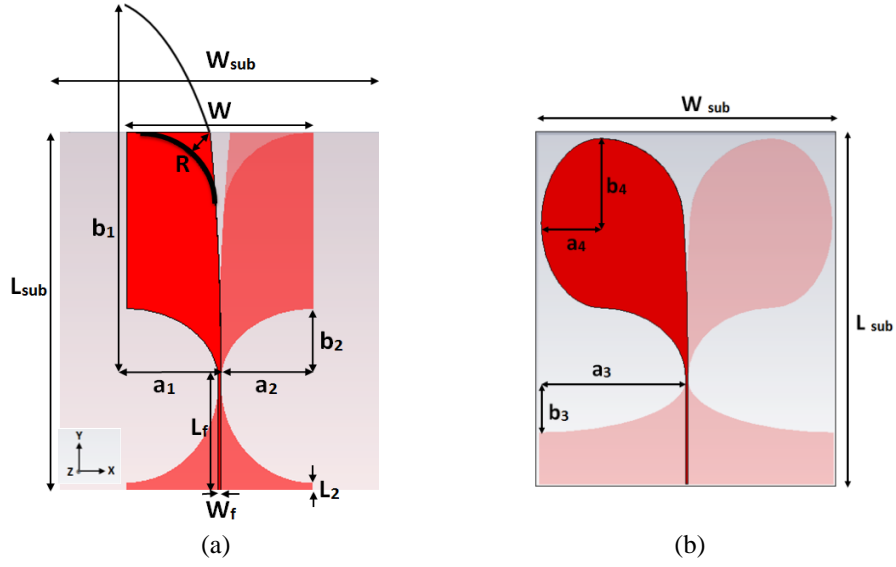
Figure 3.1 Geometry of the proposed antennas; (a) CAVA and (b) MAVA.

The designing ground plane section of the antenna is formed from the intersection of a rectangular-shaped conductor with two antifaced quarter ellipses. In order to achieve optimal bandwidth, opening rate of aperture, R, is optimised to be 45 (no unit). It is worth to point that as the R increases, the lower cut-off frequency decreases; however, it causes a gain reduction of the proposed CAVA. Therefore, there is a trade-off between cut-off frequency and gain of antenna. The AVA cut-off frequency is given by (Bai, Shi & Prather 2011):

$$f_c = \frac{c}{2W\sqrt{\varepsilon_r}} \tag{3.5}$$

According to Eq. 3.5, the cut-off frequency is about 1.01 GHz at $W = 100$ mm. To achieve the lower cut-off frequency of 0.6 GHz, W and L_{sub} should be equal to 168.5 mm and 337.1 mm, respectively, i.e., the size of antenna will be increased. Instead of this, the CAVA has been modified by adding the half ellipse with major radius of b_4 and minor radius of a_4 to extend the bandwidth without changing dimensions of the substrate. Influence of axis radii a_4 on the magnitude of reflection

36

coefficient of the MAVA is shown at Fig. 3.2. It can be seen from Fig. 3.2 that the magnitude of the reflection coefficient decreases as a_4 increases from 20 mm to 40 mm and it has acceptable value ($< $-10 dB) over desired frequency range (0.65 GHz- 6 GHz) at a_4 = 35 mm and 40 mm, respectively. Equal gains and radiation patterns can be achieved at a_4 = 35 mm and 40 mm. However, a_4 = 35 mm is selected as an optimum dimension since it provides smaller dimensions of antenna than a_4 = 40 mm. All optimised dimensions of the proposed antenna are shown in Table 3.1. It can be seen from Fig. 3.3 that the cut off frequency of CAVA and MAVA for $S_{11} \leq $-10 dB is 1.62 GHz and 0.65 GHz, respectively. Thus, MAVA operates over the frequency range from 0.65 GHz to 6 GHz.
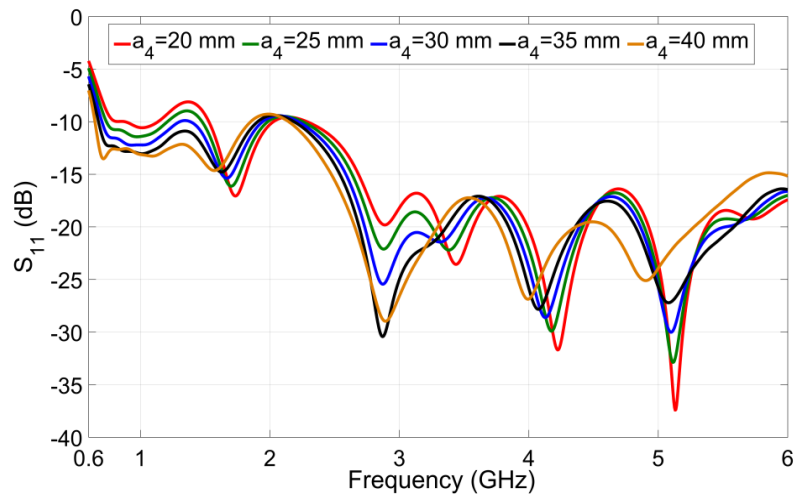
Figure 3.2 Simulated S_{11} versus frequency of the proposed MAVA for the different values of a_4 with b_4 = 49 mm.

Table 3.1 Optimal dimensions of the proposed antenna (units: mm)

Parameter	Value	Parameter	Value	Parameter	Value	Parameter	Value
L_{sub}	202	W_f	1.53	a_2	49.24	b_1	290
W_{sub}	171	L_f	62	L_1	32	a_3	84.24
R	48 (no unit)	a_1	50.77	b_2	40	b_3	30
a_4	35	b_4	49	L_2	32	W	100
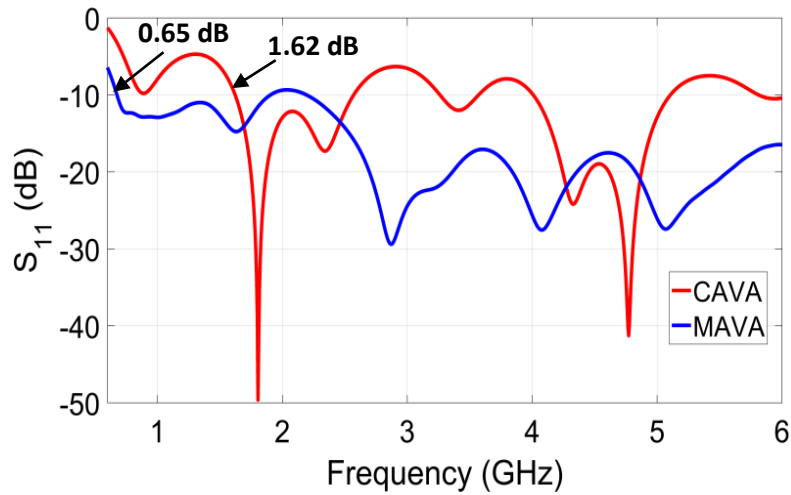
Figure 3.3 Magnitude of the reflection coefficient versus frequency for the CAVA and MAVA.

The optimised antenna was fabricated and a photograph of the fabricated antenna is shown in Fig. 3.4. The measured and simulated magnitude of the reflection coefficient of the proposed antenna in free space is shown in Fig. 3.5. As the figure reveals, the measurement result is in good agreement with the simulation result and the differences may be due to the fabrication error.
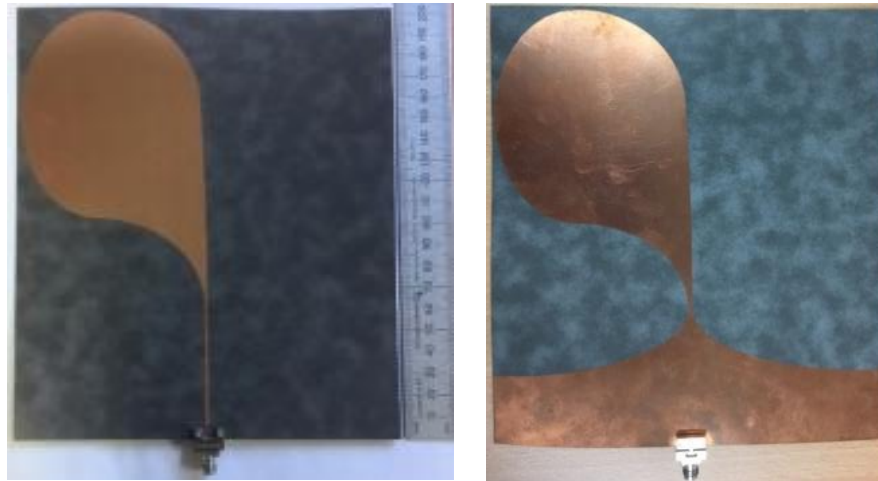
Figure 3.4 Top view (left) and bottom view (right) of the fabricated MAVA.
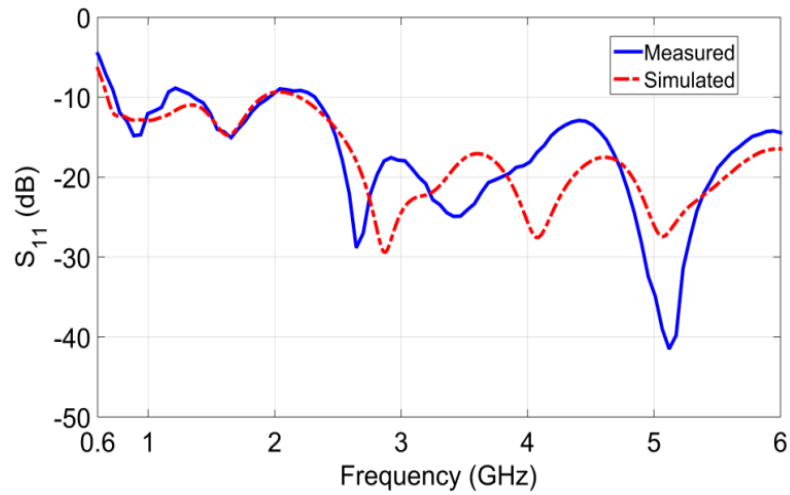
Figure 3.5 Measured and simulated S_{11} (dB) of the MAVA.

The far-field radiation patterns of the proposed antenna at three frequencies are depicted in Fig. 3.6. It can be seen from Fig. 3.6 that the antenna exhibits end-fire characteristics at all frequencies. The Half Power Beamwidth (HPBW) is the angular separation in which the magnitude of the radiation pattern decrease by 50% (or -3 dB) from the peak of the main beam. The half power beamwidth of the antenna is wide at low frequency of 0.8 GHz, it becomes narrower as frequency increases.
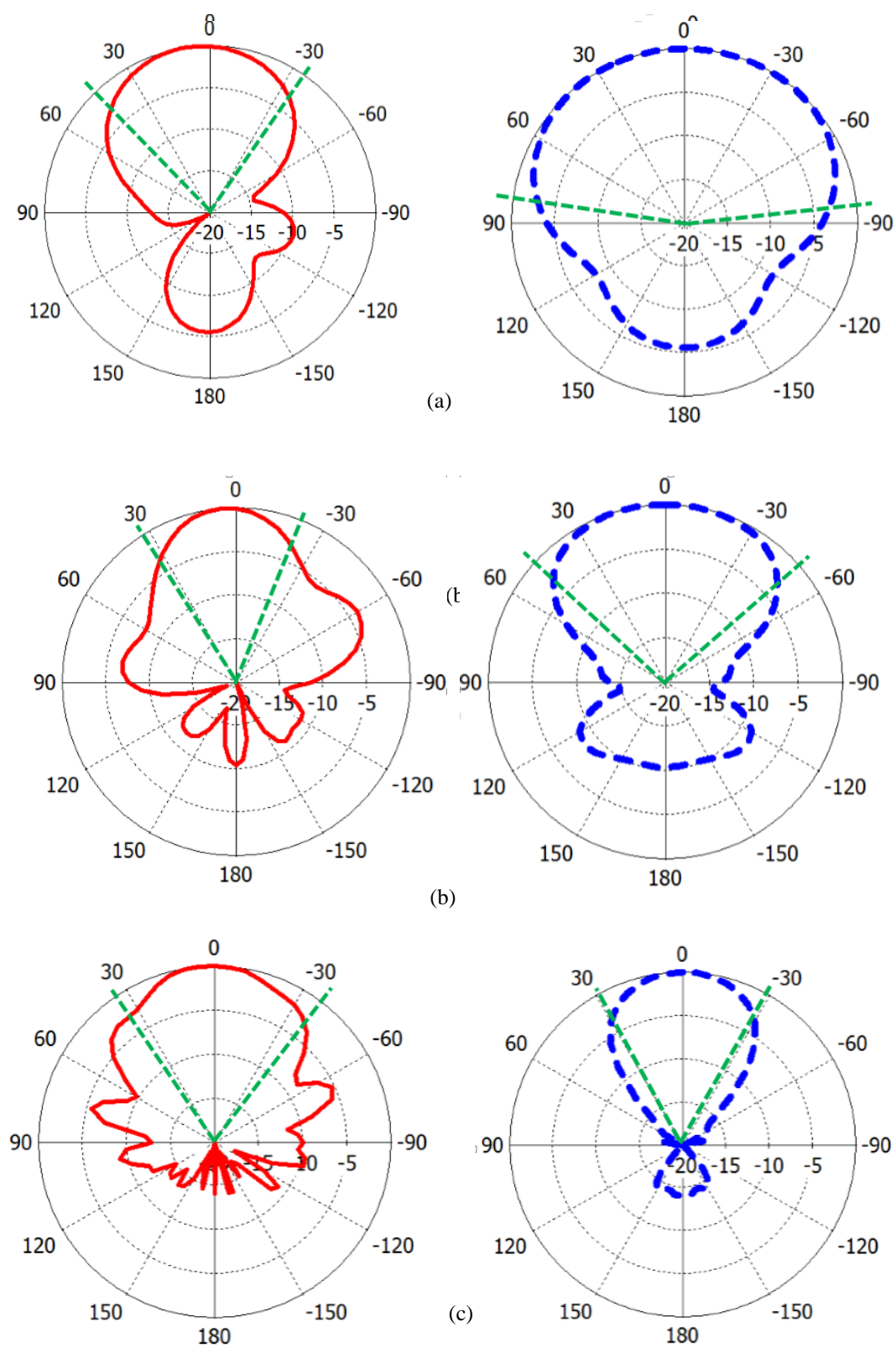
Figure 3.6 E-plane (left) and H-plane (right) radiation patterns of the MAVA at (a) 0.8 GHz, (b) 2.45 GHz and (c) 5.8 GHz.

In order to achieve desired performance of the WPT in concrete, the antenna should operate at relatively low frequency and high gain to provide suitable penetration depth and power at the location of a receiving antenna embedded inside concrete. Table 3.2 shows gain of the proposed antenna compared with the referenced antennas at three different frequencies as well as their dimensions, ε_r of substrate and bandwidth. As can be seen from Table 3.2, some of the referenced antennas (e.g., in (Fioranelli et al. 2015) and (Siddiqui et al. 2011)) have lower gain value compared with the proposed antenna at 0.9 GHz. For instance, in (Siddiqui et al. 2011) the antenna operated from 0.4 GHz to 9.8 GHz; however, the gain of antenna is zero at 0.9 GHz while this antenna has larger dimensions compared to the proposed antenna.

Table 3.2 The specification and performance of the referenced antipodal Vivaldi antennas and MAVA

Ref. No	Gain in dB at frequency of			Dimensions mm^2	ε_r of substrate	Bandwidth, GHz
	0.9 GHz	2.45 GHz	5.8 GHz			
(Fioranelli et al. 2015)	1.5	6.5	-	185×260	10	0.5 - 2
(Wang, Z et al. 2016)	-	4	6	90× 93.5	2.65	1.32 - >17
(Siddiqui et al. 2011)	0	7.5	9	282×307.4	2.33	0.4 - 9.81
(Ashraf et al. 2015)	-	6	8.5	160× 120	2.2	0.8 - 18
MAVA	4	6.5	8.5	171× 202	2.2	0.67 - > 6

3.3 MAVA with concrete sample

In this section, the MAVA is used for IHM techniques at frequency range from 0.65 GHz to 3.5 GHz. The feasibility of the proposed antenna for IHM is investigated by modelling a concrete sample in CST. The proposed MAVA was located at the distance of d from the center of the front face of a concrete sample consisting of a cubic concrete block and a concrete slab as shown in Fig. 3.7(a). An air-dried concrete was considered with dielectric constant of 4.5 and loss tangent of 0.0111 (Shams & Ali 2007). The photograph of measurement set-up with concrete sample and fabricated antenna is shown in Fig. 3.7(b). The sample consists of a concrete block and concrete slab with the dimensions of 250 mm by 250 mm by 250 mm and 250 mm by 250 mm by 100 mm, respectively, made of dry concrete. The PNA is used in the measurements. Firstly, magnitude of the reflection coefficient (S_{11}) of the MAVA at the frequency range from 0.6 GHz - 6 GHz was simulated and measured with and without concrete sample and the results are shown in Fig. 3.8. The results demonstrated changes related to the potential association with resonant wavelengths or standing waves in the concrete block(s). Also, Fig. 3.8 shows that there is a good agreement between simulation (c.f. Fig. 3.8(a)) and measured (Fig. 3.8(b)) results. Moreover, the results show that the magnitude of reflection coefficient of the antenna in free space (i.e., without concrete sample) periodical changes when frequency increases. It can be attributed to the reflection of waves from the aperture of antenna and their interference inside antenna.
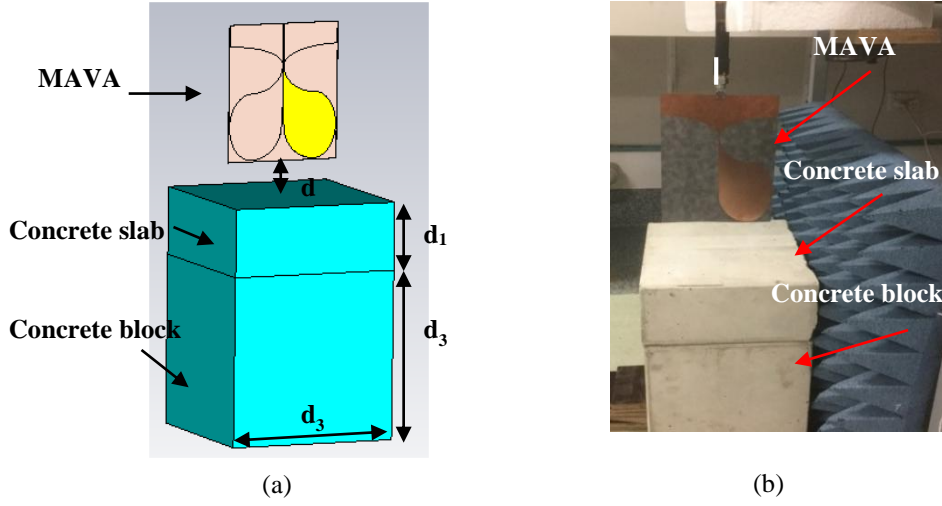
Figure 3.7 (a) Model of the proposed MAVA with the concrete sample in CST and (b) measurement setup with the concrete sample and the fabricated antenna.
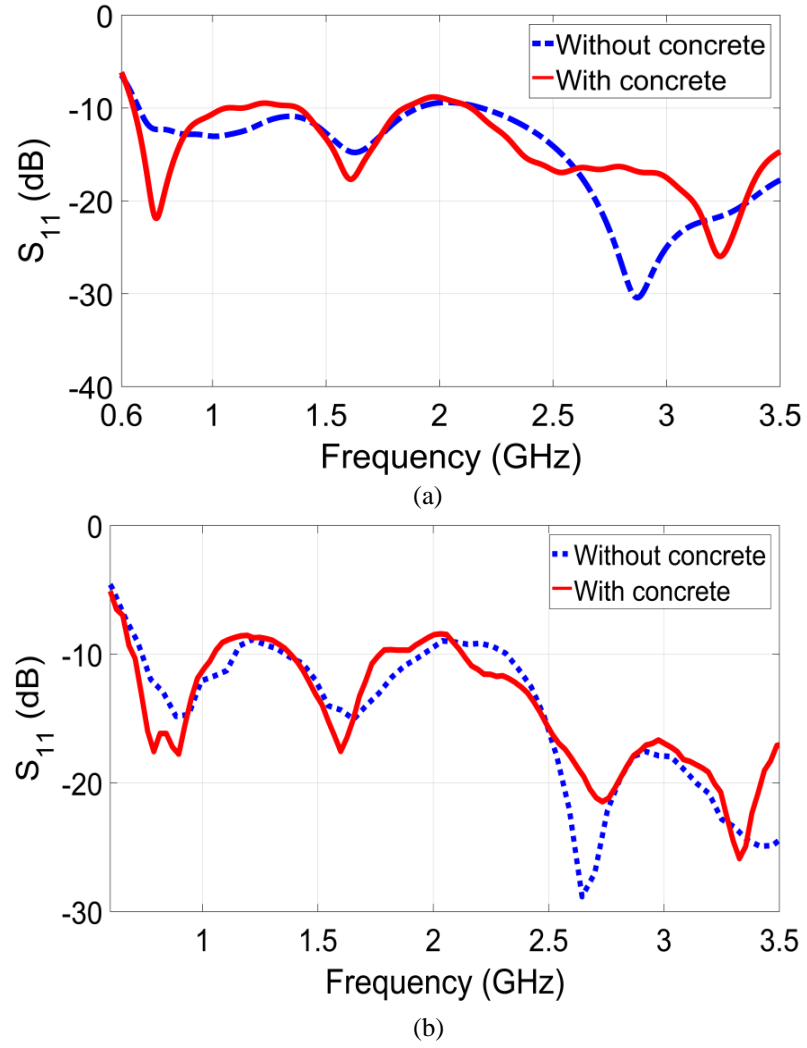
Figure 3.8 (a) Simulated and (b) measured magnitude of the reflection coefficient versus frequency with and without concrete sample at $d = 100$ mm.

3.4 MAVA with concrete sample possessing air gap

In this part, an air gap with thickness of d_2 was created between the block and slab at depth of d_1 as shown in Fig. 3.9. Extensive numerical study on magnitude of the reflection coefficient at different values of d, d_1 and d_2 at $d_1+d_3 = 500$ mm was performed. Fig. 3.10 shows the magnitude of reflection coefficient versus d with and without gap inside the concrete at 0.9 GHz. Thickness of the gap, d_2, is 5 mm here. As Fig. 3.10 reveals, maximum change between two curves occurs at the minimum S_{11} when d is approximately 70 mm. Magnitude of the reflection coefficient versus distance between the front face of concrete block and air gap (d_2) is depicted at Fig. 3.11. As can be seen from Fig. 3.11, the magnitudes of reflection coefficient are -17.27 dB and -9.71dB at 0.91 GHz and 2.37 GHz, respectively, while there is no air gap inside the concrete. When d_1 changes from 10 mm to 450 mm the magnitude of reflection coefficient varies periodically indicating standing wave patterns with different wavelengths corresponding to different operating frequencies.
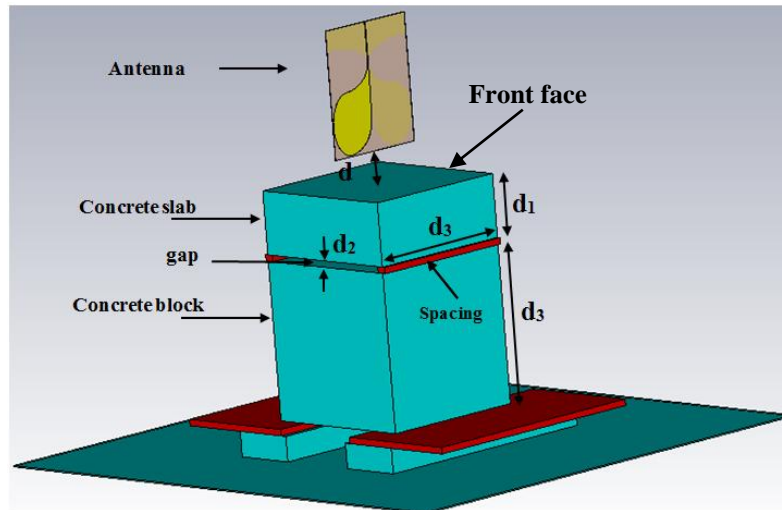
Figure 3. 9 Model of the proposed MAVA with the concrete sample possessing air gap in CST.
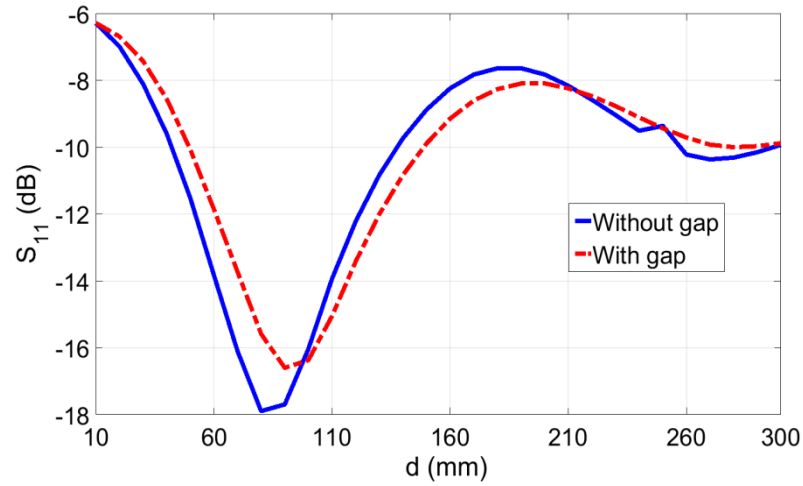
Figure 3.10 Magnitude of the reflection coefficient versus distance between MAVA and front face of the concrete sample, d, at $f = 0.9$ GHz without and with gap at $d_1 = 10$ mm and $d_2 = 5$ mm.

It can be clearly seen from Fig. 3.11 that at each value of the d_1 the magnitude of reflection coefficient is different for different values of gap thickness, i.e. 5 mm and 10 mm, at each frequency, i.e. 0.91 GHz and 2.37 GHz. This result can be used for evaluation gap inside concrete. The changes of amplitude of these patterns can be attributed to the multiple reflections of waves from back and side faces of the concrete block.
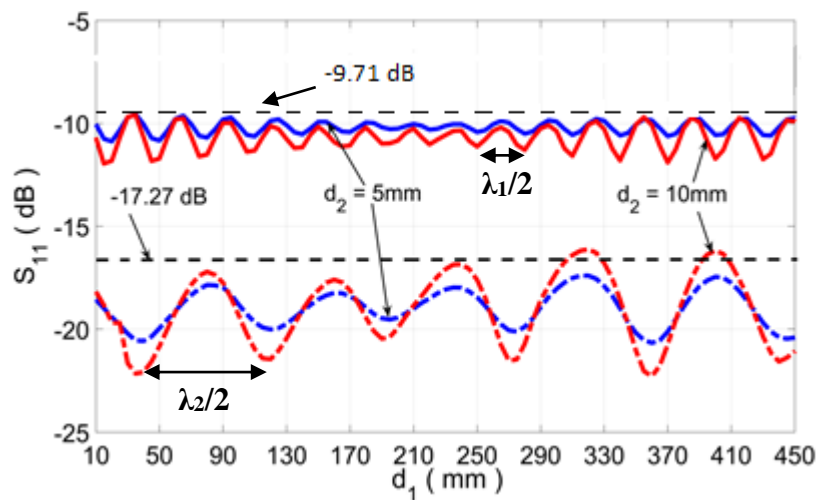
Figure 3.11 Magnitude of the reflection coefficient versus distance between the front face of concrete block and air gap, d_1, at 0.91 GHz (dashed line) and 2.37 GHz (solid line) and at $d_2 = 5$ mm and 10 mm.

Fig. 3.12 shows the magnitude of reflection coefficient versus d_2 at four frequencies. It can be clearly seen from Fig. 3.12 that a small gap (i.e., from 5 mm – 10 mm) creates changes of S_{11} without ambiguity at 2.37 GHz. Overall, Fig. 3.12 demonstrates that operating frequency can be selected for certain applications.
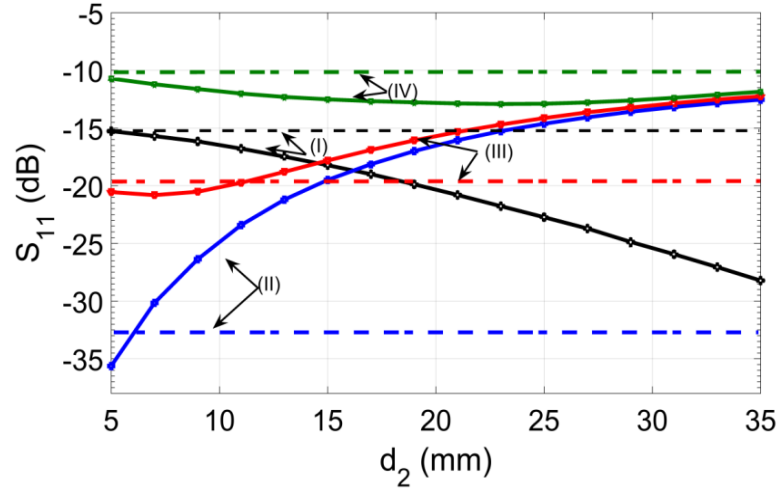
Figure 3.12 Magnitude of the reflection coefficient versus thickness of air gap, d_2, at: (I) f = 0.7 GHz, (II) f = 0.81 GHz, (III) f = 0.91 GHz and (IV) f = 2.37 GHz (d = 70 mm and d_1 = 45 mm). Dash lines show the value of the magnitude of reflection coefficient while there is no gap inside the concrete sample at the selected frequencies.

The electrical field distribution in the proposed antenna, free space and inside the concrete sample with and without gap at two frequencies is shown in Fig. 3.13 when the MAVA radiates EM waves toward the concrete sample. The wavelength inside the concrete, λ_g, is 155.44 mm (59.64 mm) at frequency of 0.91 GHz (2.37 GHz). The size of the samples (d_1+d_3 = 500 mm) are almost 3 (8) times larger than the wavelength inside the concrete. Figs. 3.13(a)-(b) demonstrate standing waves inside the concrete sample with different wavelengths. It can also be clearly seen that air gap inside concrete changes the standing wave patterns at both frequencies.
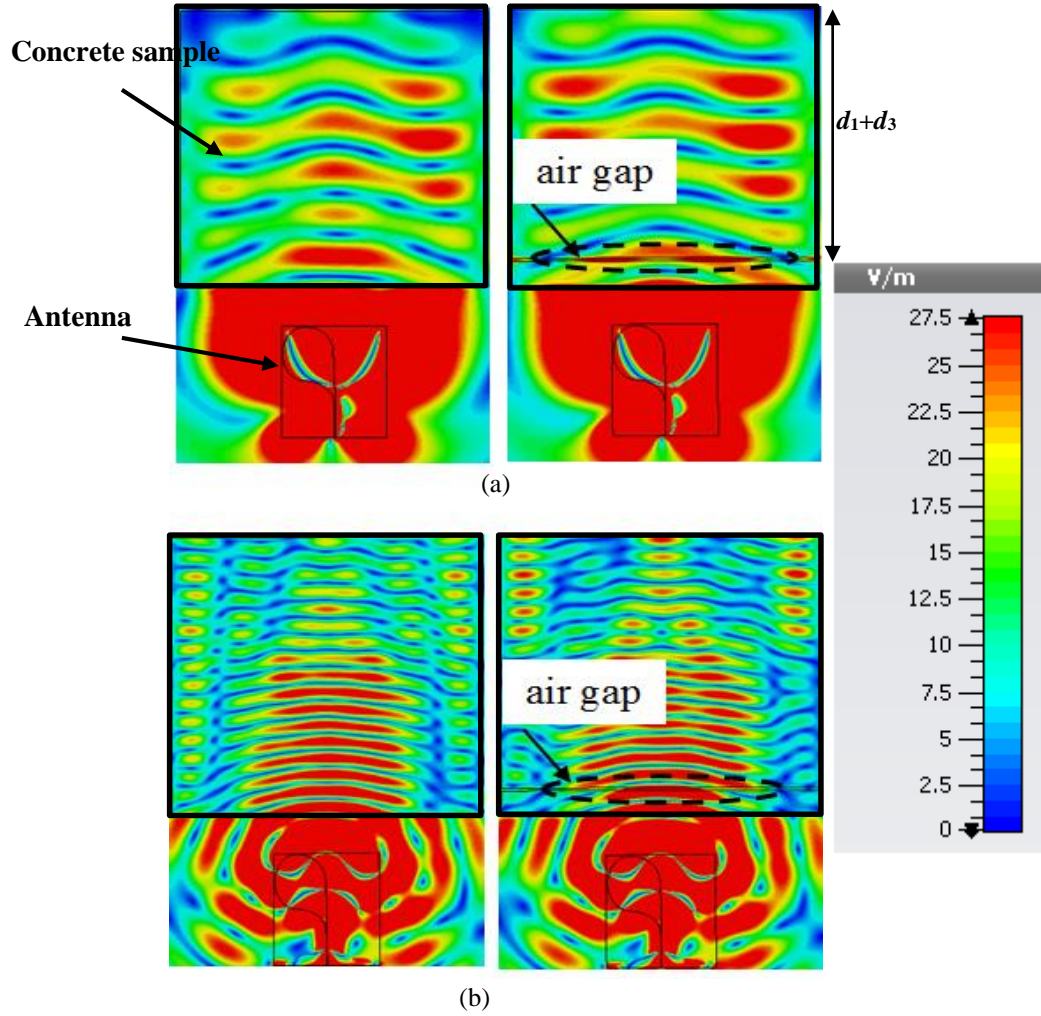
Figure 3.13 Electrical field intensity distribution in the proposed antenna and the concrete sample (left) without and (right) with air gap at $d = 70$ mm and at two frequencies: (a) 0.91 GHz and (b) 2.37 GHz ($d_1 = 45$ mm, $d_2 = 5$ mm).

Measurements of magnitude and phase of the reflection coefficient versus frequency were conducted five times at each selected air gap which located between the concrete block and slab. Also, in order to provide reliably measurement results, the average magnitude and phase of reflection coefficient for each gap were calculated to reduce measurement error attributed to arrangement of the sample with the gap. Measurement setup is similar to that shown in Fig. 3.7(b). Average magnitude of reflection along with standard deviation (SD) versus gap value at four frequencies is shown in Fig. 3.14. It can be seen from Fig. 3.14 that S_{11} (d_2) is almost linear at all frequencies and the maximum and minimum SDs occur at 0.87 GHz and 2.44 GHz, respectively. Fig. 3.15 the measured average phase of reflection coefficient along with SD. It can be seen from Fig. 3.15 that the phase of reflection coefficient versus d_2 is not
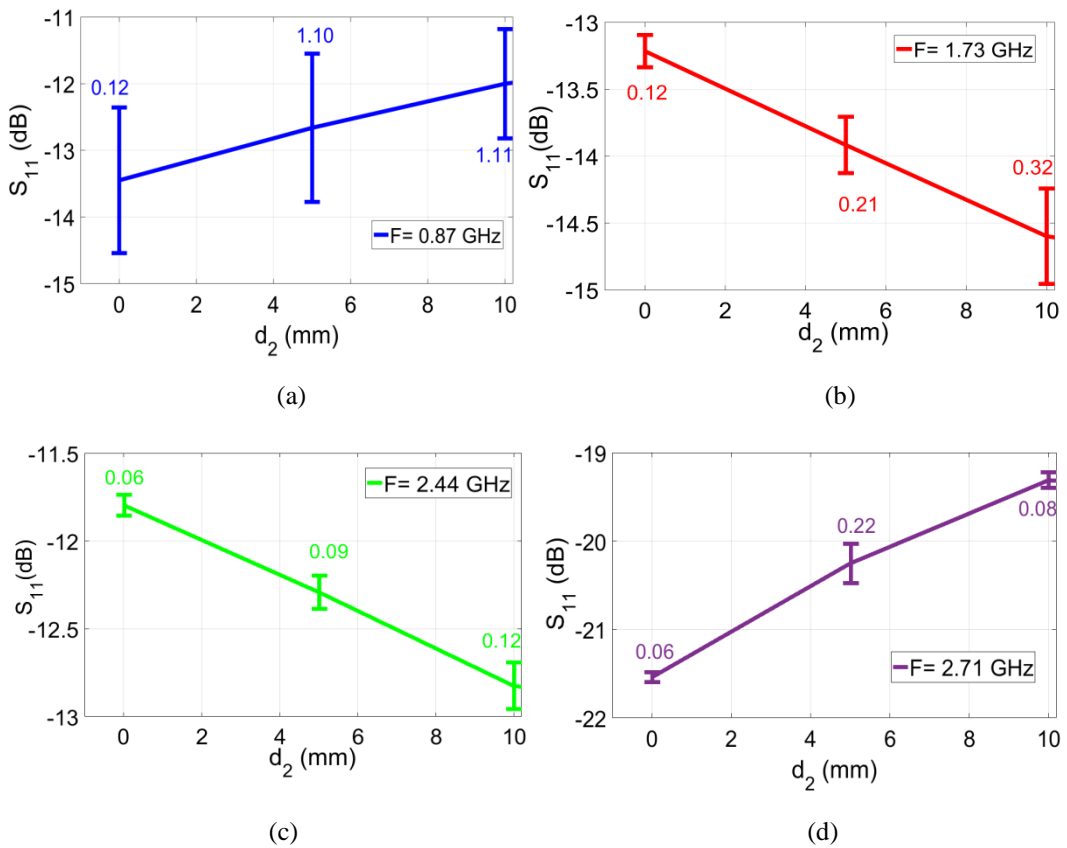
Figure 3.14 Measured average magnitude of the reflection coefficient with standard deviation versus gap value at (a) 0.87 GHz, (b) 1.73 GHz, (c) 2.44 GHz, and (d) 2.71 GHz.

linear at all frequencies and the maximum and minimum SDs occur at 2.44 GHz and
0.87 GHz, respectively. The results show that SD for the magnitude (phase) is >1 dB
(<1 degree) and <0.5 dB (>1 degree) at the low and high frequencies, respectively.
This different behavior of the measured magnitude and phase of reflection coefficient
should be taken into account at certain application of this technique.
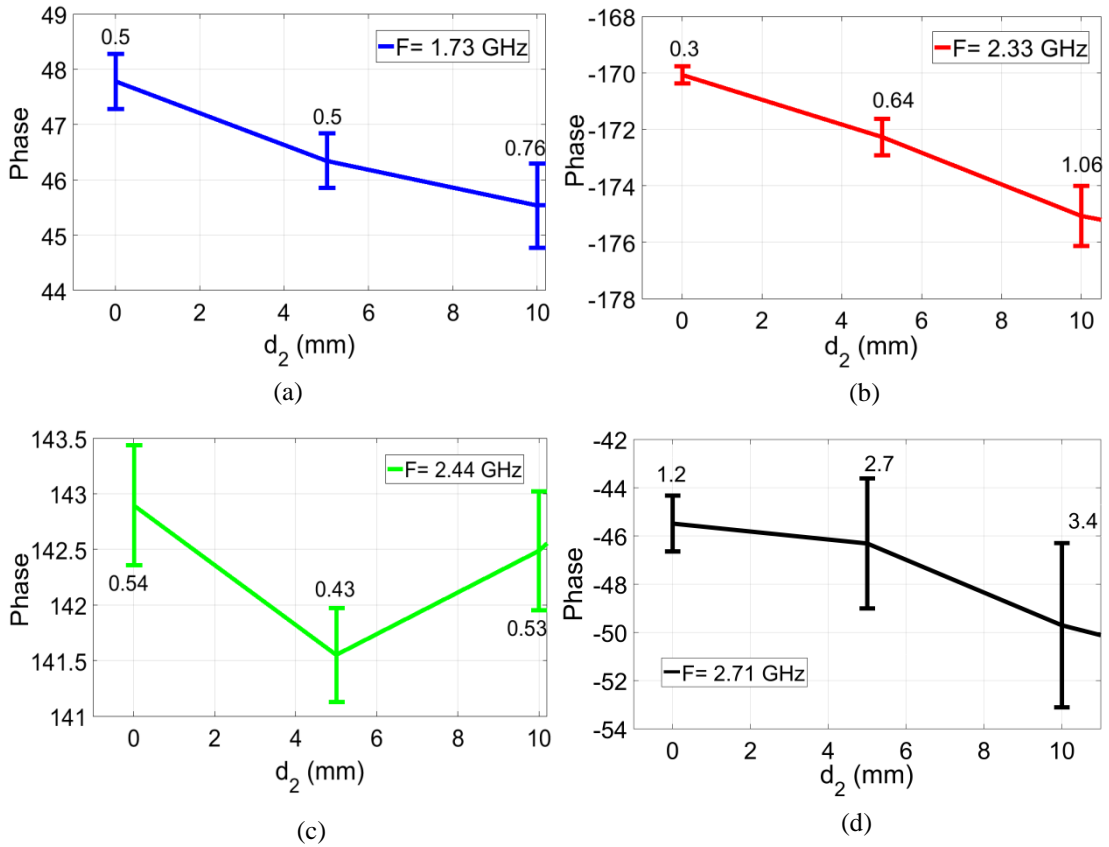
Figure 3.15 Measured average phase (in degree) of the reflection coefficient with
standard deviation versus gap value at (a) 1.73 GHz, (b) 2.33 GHz, (c) 2.44 GHz, and
(d) 2.71GHz.

3.5 MAVA with reinforced concrete sample

In reality, reinforced bars (rebars) are embedded inside concrete in order to increase
its mechanical stability. To investigate the influence of rebars on the reflection and
transmission properties of concrete samples irradiated by MAVA, extensive

simulations using CST MWS and measurements with the fabricated MAVA and reinforced concrete samples have been performed. The most critical simulated and measured results at the entire frequency range from 0.6 GHz - 3.5 GHz and at selected single frequencies are presented in this section for two samples. One of them has two parallel rebars and another had a rebar cell.

3.5.1 MAVA with concrete sample possessing two rebars

Two parallel rebars in one of the samples can be arranged to be parallel or orthogonal to electric field polarsation vector of the MAVA (referred to as parallel or vertical configuration, respectively) as shown in Figs. 3.17(a)-(b). The rebars with diameter of 16 mm and distance of $g = 110$ mm are embedded inside the concrete block with dimensions of 250 mm by 250 mm by 366 mm at depth of 100 mm. The MAVA is located at $d = 50$ mm above the air-to-concrete interface. The material of the rebars is steel-1008 (conductivity of 7.69×10^6 S/m). Fig. 3.16(c) shows the measurement setup. The sample used in this setup consists of a 100-mm thick concrete slab with dimensions of 250 mm by 250 mm, and a 250-mm concrete cubic block. The gap of 16 mm between the slab and the block was filled by plasterboard pieces and the rebars as shown in Fig. 3.16(c). The complex reflection coefficient was measured using the PNA.
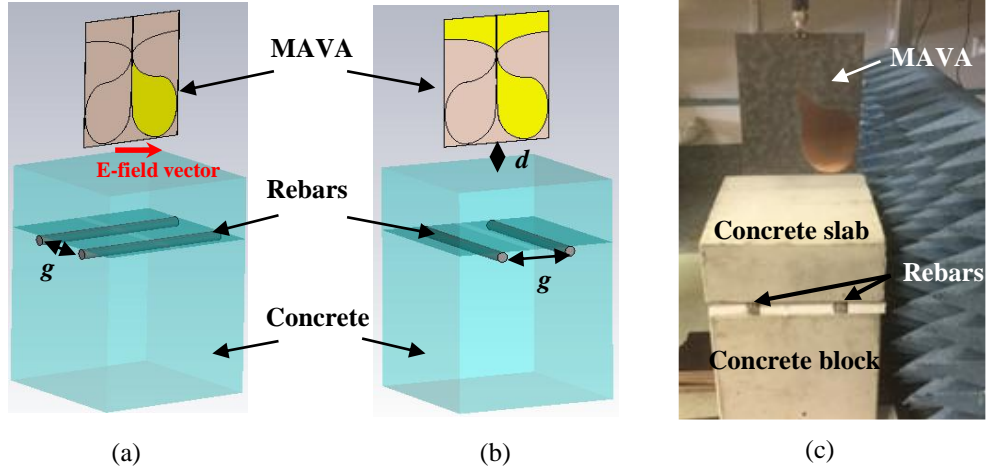
Figure 3.16 Model of the setup with concrete sample possessing two rebars: (a) parallel and (b) vertical configuration, and (c) photo of the measurement setup.

Simulated and measured magnitudes of the reflection coefficient versus frequency at two configurations are shown in Fig. 3.17(a)-(b), respectively. Overall, the magnitudes of the reflection coefficient of the concrete without and with two rebars at the vertical configuration represent similar trends but the rebars cause the increase of amplitude of ripples. It can be clearly seen in Fig. 3.17 that this increase is higher at the parallel configuration than at the vertical configuration at the most frequencies, as expected. There is a good agreement between simulation and measurement results as shown in Fig. 3.17(a)-(b), respectively. Discrepancy between simulation and measurements can be attributed to the gap filled by plasterboard pieces in the experimental concrete sample.
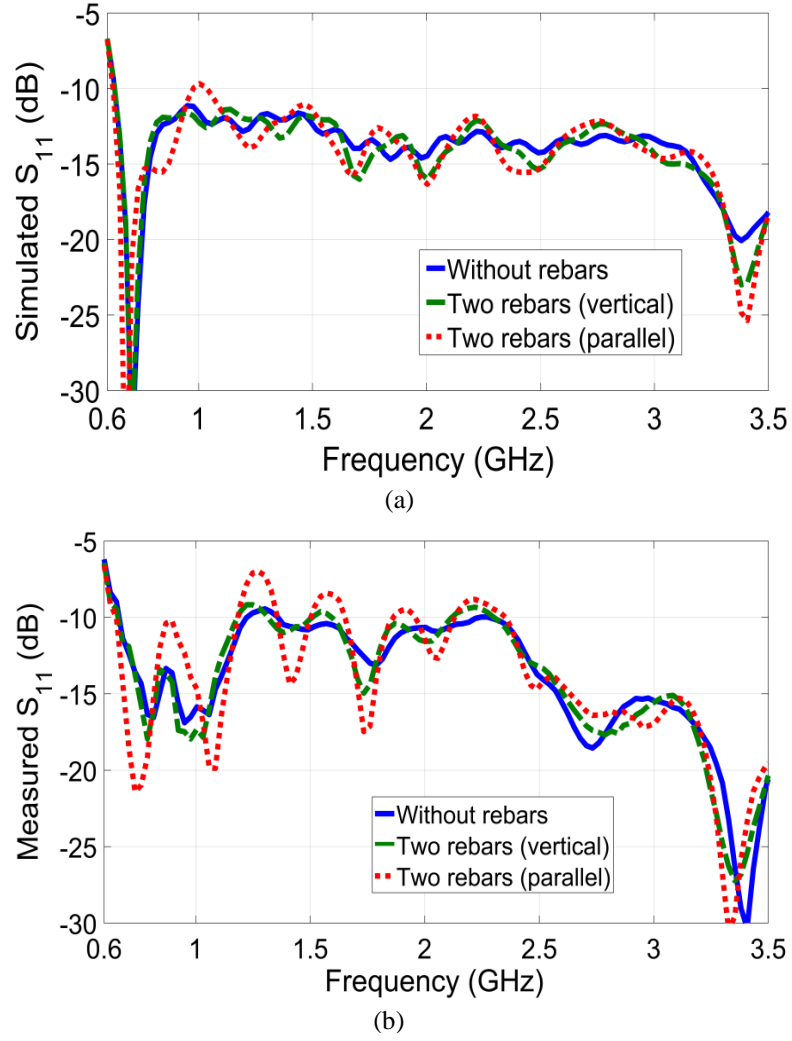
Figure 3.17 Simulated and measured magnitude of the reflection coefficient without and with parallel rebars at two configurations: (a) simulated and (b) measured S_{11}.

3.5.2 MAVA with concrete sample possessing rebar cell

Another reinforced concrete sample has an embedded rebar cell. Fig. 3.18(a) shows the model of the MAVA with the concrete sample. The sample has dimensions of 250 mm by 250 mm by 382 mm and dielectric constant and loss tangent of the dry concrete. A 4-rebar cell with mesh period parameter g (c.f. Fig. 3.18(b) is embedded in concrete so that the distance between the top (bottom) surface of sample and the center of lower two rebars, d_1 (d_3), and upper two rebars, d_4, are 132 mm (250 mm) and 100 mm, respectively. Each rebar has diameter of 16 mm and was made of steel-1008.

Measurement setup is similar to that shown in Fig. 3.16(c). The gap of 32 mm between the slab and the block was filled by plasterboard pieces and the rebar cell as shown in Fig. 3.16(c).
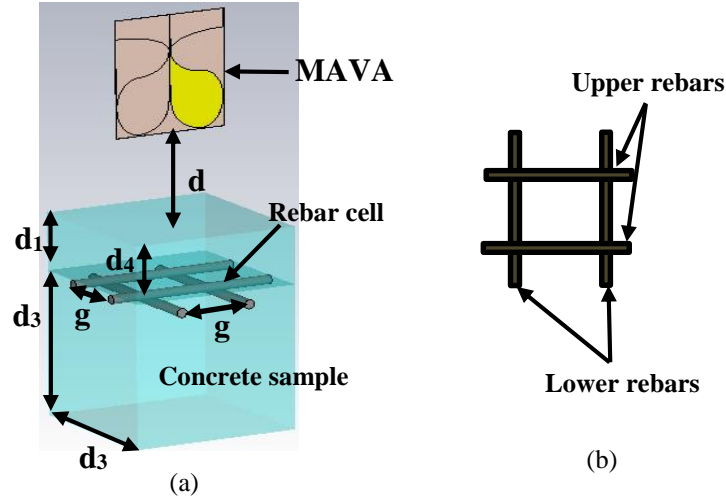
Figure 3.18 MAVA and concrete sample with a rebar cell: (a) model in CST and (b) configuration of the rebar cell.

Simulated and measured magnitudes of the reflection coefficient at three distances between the antenna and the concrete samples with and without rebar cell at $g = 110$ mm are shown in Fig. 3.19 and Fig. 3.20. Firstly, the simulated magnitude of reflection coefficient with the concrete sample without rebars (c.f. Fig. 3.19) and in free space (c.f. Fig. 3.5) is compared. The comparison shows the following: 1) the presence of concrete sample increases reflection at some frequencies that can be attributed to the reflection from the sample boundaries, in particular from the top surface irradiated by the MAVA and 2) the magnitude of reflection coefficient with the concrete sample at some frequencies corresponding to the resonant dips is lower than in free space at the same frequencies; for instance, the reflection reduces significantly at frequencies from 0.6 GHz to 0.8 GHz at $d = 0$ and from 1.4 GHz - 1.7 GHz at $d = 0$ and 100 mm. There is no gap between the MAVA and the surface of the concrete slab at $d = 0$.
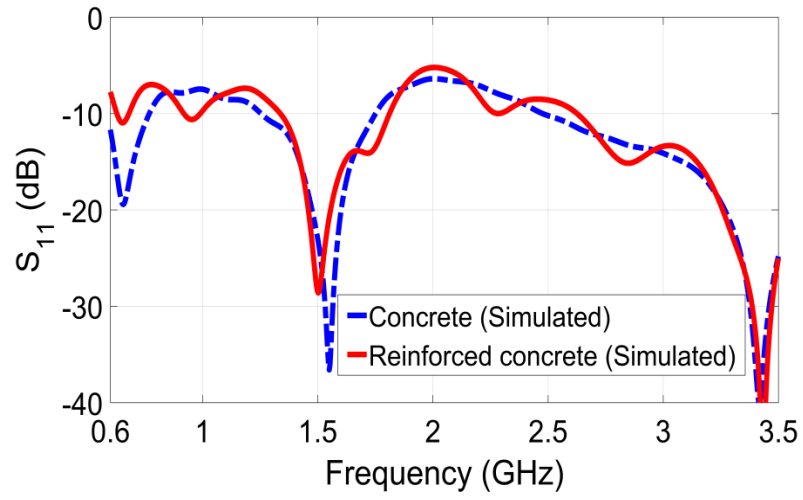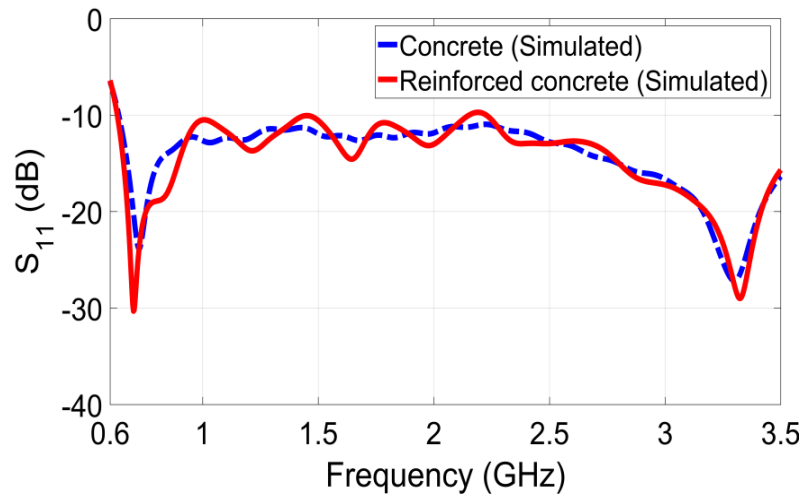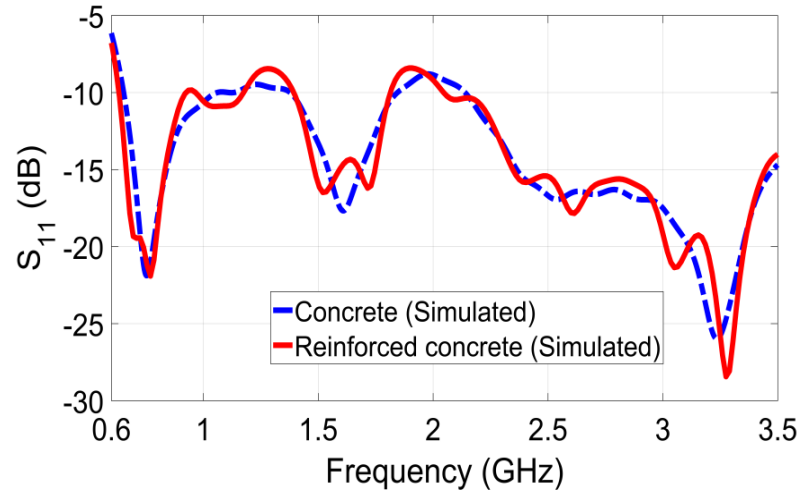
Figure 3.19 Simulated S_{11} (dB) versus frequency with concrete and reinforced concrete at $g = 110$ mm and (a) $d = 0$, (b) $d = 50$ mm, and (c) $d = 100$ mm.

Secondly, we considered the influence of rebars on the simulated magnitude of reflection coefficient. The main observation is that embedding the rebar cell leads to changes of magnitude of the dips and there are small shifts of the frequency corresponding to the peaks at all d values while no new peaks occur. The most significant changes can be seen at $d = 0$. Overall, the simulated results show that the reflection from the boundaries of the sample plays a dominant role in relative (to free space) changes of the magnitude of reflection coefficient. The measured results demonstrate a similar behavior of the magnitude of reflection coefficient. A slightly higher number of ripples and the resonant responses in measured results compared with the simulated results can be attributed to the reflection from the gap filled by plasterboard pieces in the experimental samples. It is worth mentioning that embedding the rebars increases the number of dips at $d = 50$ mm and 100 mm, respectively, compared with the case at $d = 0$. These dips occurred due to the influence of the rebars. In general, the results shown in Fig. 3.20 demonstrate that one of the main features of reinforced concrete samples irradiated by the MAVA is the indication of multiple ripples and the resonant responses at the reflection spectrum. Therefore, one of the advantages of wideband antennas, such as MAVA, is the opportunity to select a desired single frequency for a certain application.
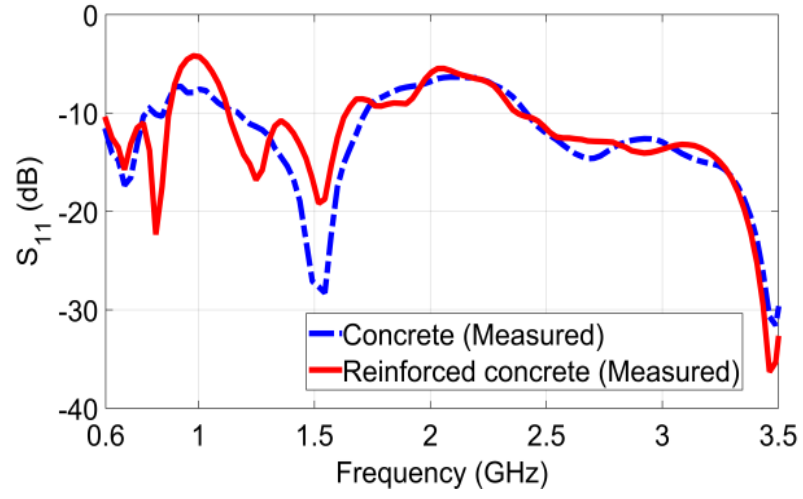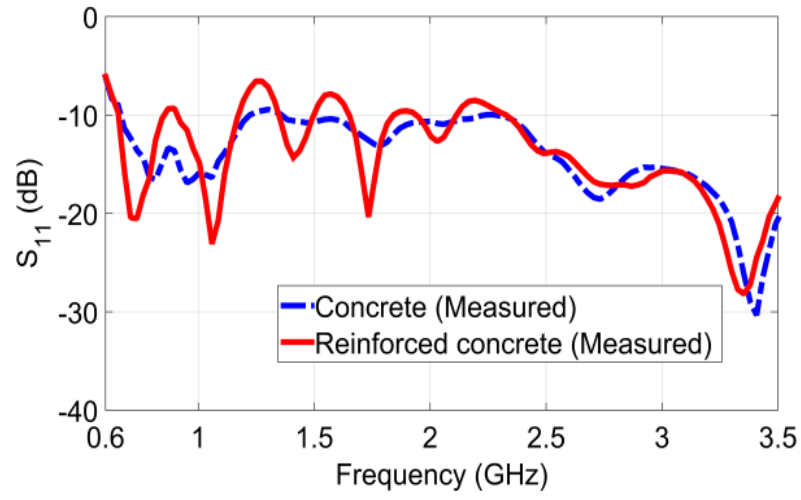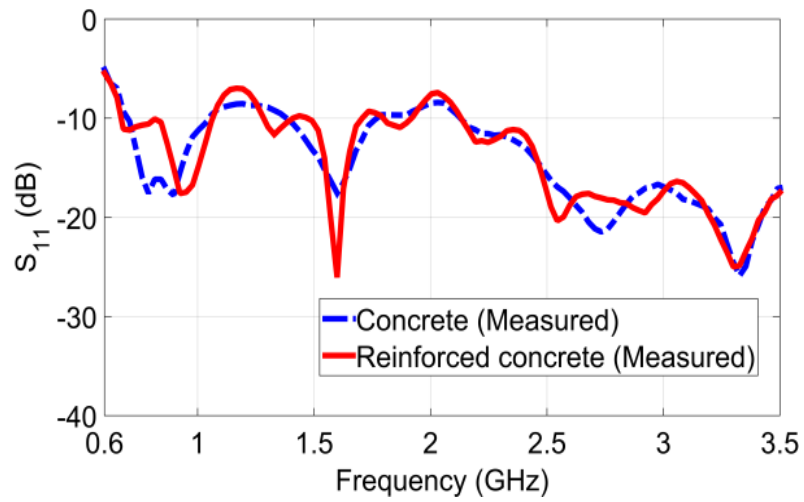
Figure 3. 20 Measured S_{11} (dB) versus frequency with concrete and reinforced concrete at $g = 110$ mm and (a) $d = 0$, (b) $d = 50$ mm, and (c) $d = 100$ mm.

3.5.3 Electrical field intensity distribution

Simulation and analysis of the electrical field intensity (referred to as E-field) distributions in the proposed MAVA and the finite samples as introduced in Fig. 3.7 and Fig. 3.18 have been performed at several single frequencies over the operating frequency range to further investigate the reflection as well as propagation of microwaves in the samples irradiated by the MAVA. Fig. 3.21 shows selected results of E-field distributions obtained at d = 50 mm and at a few single frequencies at the same scale. Several observations can be made from Fig. 3.21. At all selected frequencies the antenna radiates toward the sample and the EM radiation is partly reflected from air-to-concrete interface, partly transmits into the sample and propagates through the sample. The propagation of the EM waves in the sample is a complex function of the operating frequency, polarisation of radiation of the antenna, and the presence of rebar cell. Moreover, the analysis of E-field distributions at low frequencies clearly shows that the electromagnetic waves are almost blocked by rebar cell as shown in Fig. 3.21 at 0.7 GHz. At this frequency, the influence of rebar cell on the reflection property of the sample is significant, i.e., it leads to appearance of the resonant peak at the simulated and measured reflection spectra as shown in Fig. 3.19(b) and Fig. 3.20(b). It happened because parameter g is equal half electrical wavelength (110 mm) at this frequency, and as a result microwaves at this frequency are significantly shielded by the rebar cell similar to the case described in (Jiang, Georgakopoulos & Jonah 2012). Another important observation can be made from Fig. 3.21 at frequency of 2.02 GHz, it can be seen that microwaves propagate through the rebar cell and the sample (c.f. Fig. 3.19 and Fig. 3.20) and there are no peaks, and the indication of the influence of the rebar cell on the reflection spectra (c.f. Fig. 3.19(b) and Fig. 3.20(b)).
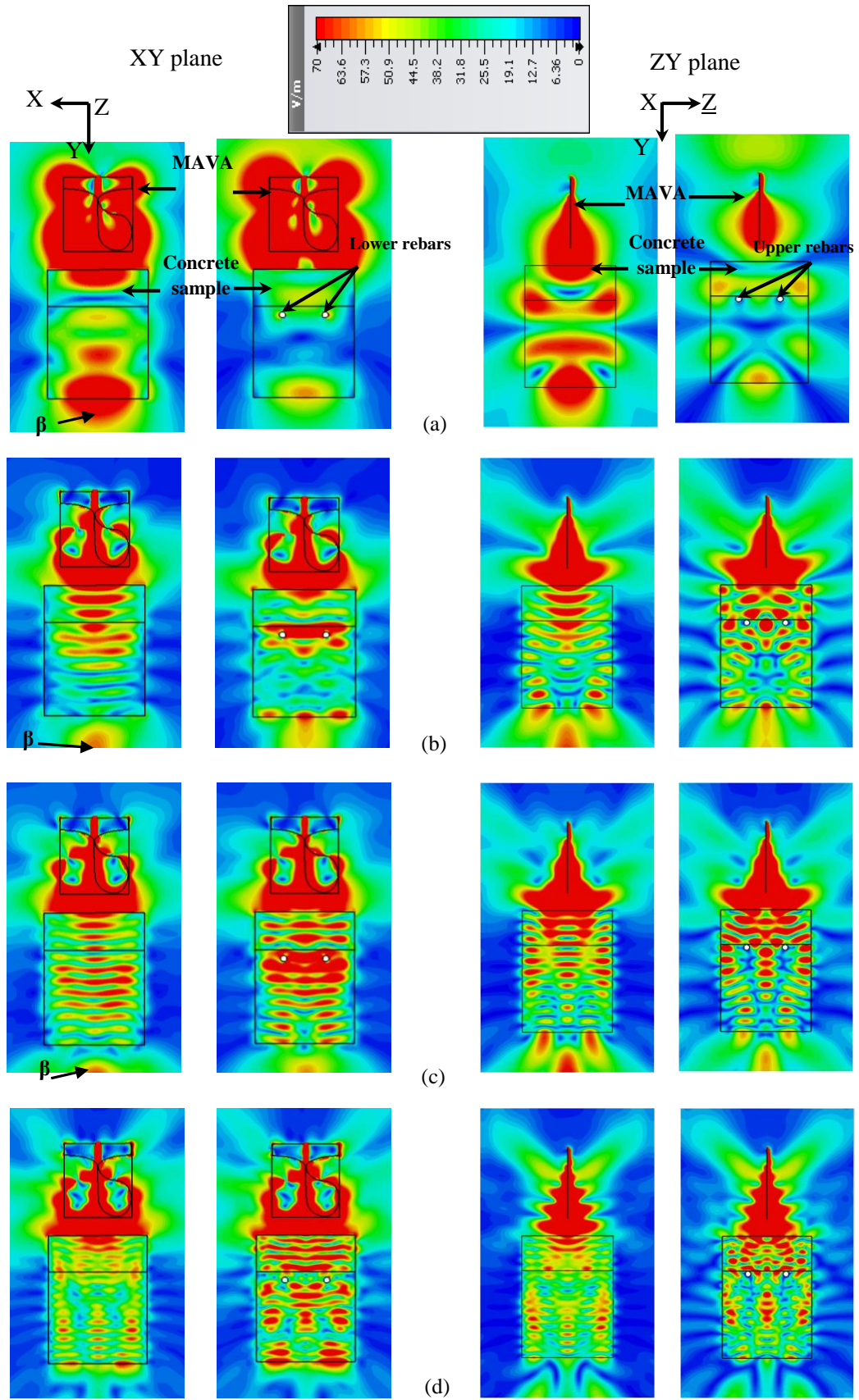
Figure 3.21 Electrical field intensity distribution in the concrete and reinforced concrete samples at (left) XY- plane and (right) ZY-plane, $d = 50$ mm, and frequency of (a) 0.70 GHz, (b) 2.02 GHz, (c) 2.45 GHz, and (d) 3.30 GHz.

In this case, the rebar cell concentrates E-field in the area of the rebars localisation and is scattered by the rebars, i.e., the rebar cell affects propagation of microwaves through the sample. Similar effects of the concentration and scattering of E-field by the rebar cell can be seen in Fig. 3.21 at 2.45 GHz where the resonant peaks can been observed with and without rebars with a very small difference (c.f. Fig. 3.19(b) and Fig. 3.20(b)). In addition, standing wave pattern inside the sample can be clearly seen in Fig. 3.21 at 2.45 GHz as a result of the reflection of microwaves from the bottom of the sample, and decreasing E-field intensity beyond the bottom, i.e., propagation of microwaves through the sample is reduced, due to the influence of the rebar cell. Finally, the consideration of E-field distributions at 3.3 GHz shows that the concentrations of E-field in the sample with rebar cell increases, and this can be attributed to resonant conditions in the areas between rebar cell and the top as well as the bottom of the sample. The magnitude of reflection coefficient is significantly changed at this frequency (i.e., 3.3 GHz) by introducing the rebar cell as can been seen in Fig. 3.19(b) and Fig. 3.20(b).

3.6 Coupling between MAVA and a microstrip patch antenna embedded in concrete and reinforced concrete samples

To investigate transmission of microwaves in the reinforced concrete sample, a microstrip patch antenna was embedded in the sample. The microstrip patch antenna consists of a rectangular patch of length, L_P, and width, W_P, which is imprinted on a rectangular substrate of thickness, h, with a rectangular ground plane as shown in Fig. 3.22(a).
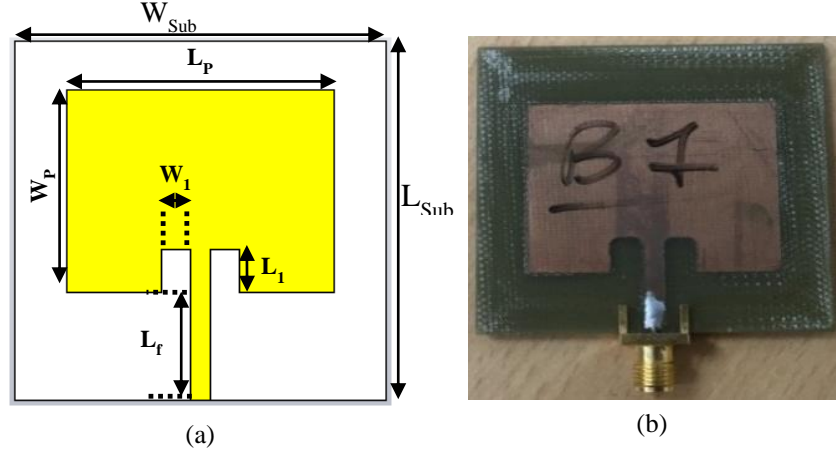
Figure 3.22 (a) Schematic of the microstrip patch antenna and (b) photograph of fabricated prototype (Salama & Kharkovsky 2013).

The first step of the design procedure of a rectangular patch antenna is to compute its physical dimensions. The physical width and length of the microstrip patch antenna is calculated using following equations (Balanis 2016):

$$W_P = \frac{1}{2f_r\sqrt{\mu_0\varepsilon_0}}\sqrt{\frac{2}{\varepsilon_r + 1}} \tag{3.6}$$

$$L_P = \frac{1}{2f_r\sqrt{\mu_0\varepsilon_0}\sqrt{\varepsilon_{reff}}} - 2\Delta L \tag{3.7}$$

$$\varepsilon_{reff} = \frac{\varepsilon_r + 1}{2} + \frac{\varepsilon_r - 1}{2}[1 + 12\frac{h}{W_P}]^{-\frac{1}{2}} \tag{3.8}$$

$$\Delta L = 0.412h\frac{(\varepsilon_{reff} + 0.3)(\frac{W_P}{h} + 0.264)}{(\varepsilon_{reff} - 0.258)(\frac{W_P}{h} + 0.8)} \tag{3.9}$$

where

ε_r = Dielectric constant of substrate

μ_0 = Permeability of free space

ε_0 = Permittivity of free space

ε_{reff} = Effective dielectric constant

60

ΔL = The extended incremental length of the patch

The microstrip patch antenna is designed with dimensions of copper patch of $35\times29\times0.035$ mm^3 and substrate of $50\times50\times1.5$ mm^3 as shown in Fig. 3.22. The substrate is made of FR4 with ε_r = 4.3 and $tan\delta$ = 0.025. Both sides of the patch antenna were covered by a foam sheet (as a superstrate) with dimensions of $55\times55\times10$ mm^3 and was located in an air box with dimension of $55\times55\times10$ mm^3 inside the sample at d_1 = 132 mm under the centre of the rebar cell.

Fig. 3.23(a) shows the model of the two-antenna setup in CST with MAVA as an external antenna and the microstrip patch antenna as an internal (embedded) antenna (referred to as the two-antenna system) operating at 2.45 GHz. Measurement setup included the reinforced concrete sample and arrangement of the MAVA used in the measurement described in the previous section. In addition, two air-filled grooves were made on the surface of the cube to locate the microstrip patch antenna with superstrate and a cable connecting the antenna and the PNA as shown in Fig. 3.23(c). Then, the cube with the antenna and cable was covered by the rebar cell, plasterboard pieces and concrete slab as described above.
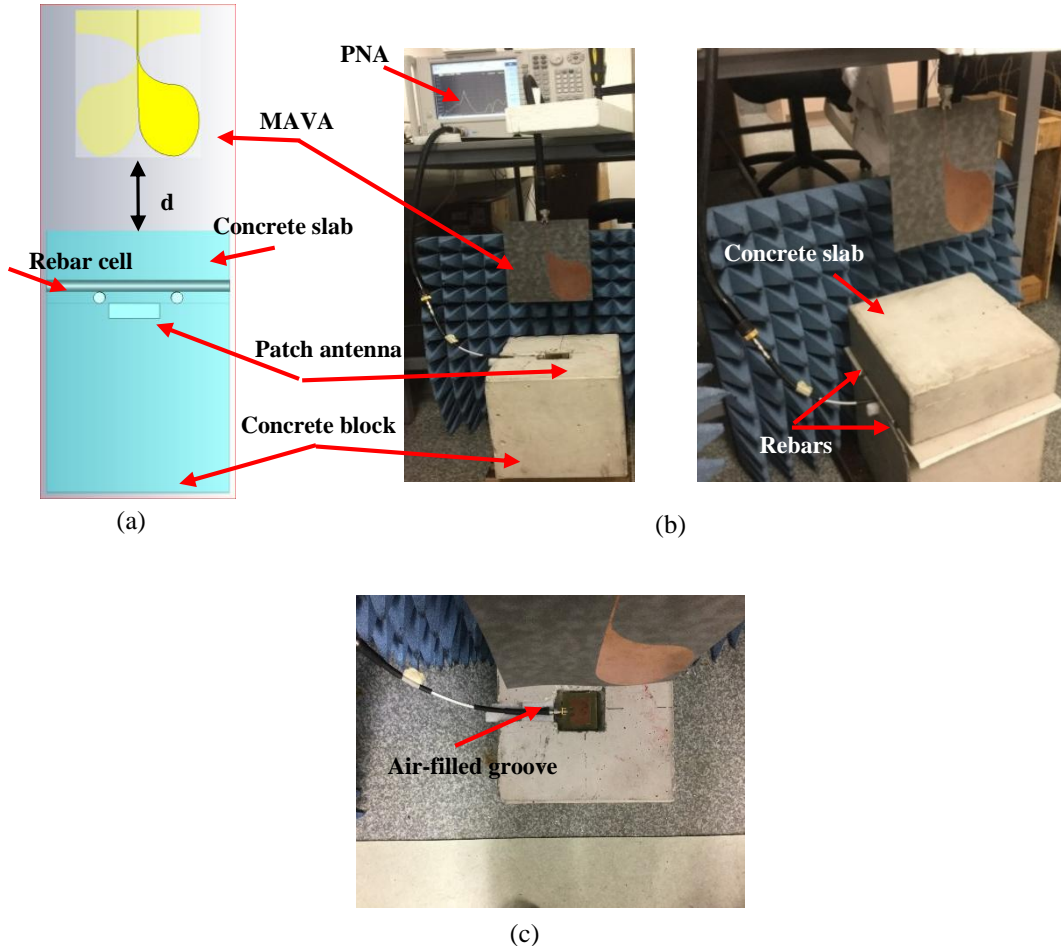
Figure 3.23 Reinforced concrete sample with the two-antenna system, (a) cross-sectional view of the model in CST, (b) picture of the measurement setup without (left) and with (right) concrete slab and rebar cell and top view of the air-filled grooves.

In practice, a typical value of mesh period parameter g is in the range of 101.6 mm to 304.8 mm (Jiang, Georgakopoulos & Jonah 2012). The simulated magnitude of the reflection coefficient of the patch antenna in free space, concrete and reinforced concrete samples at $d = 50$ mm and $g = 110$ mm is shown in Fig. 3.24(a). It can be seen from Fig. 3.24(a) that embedding the patch antenna inside the concrete sample leads to an increase (relative to free space) of the resonant frequency and S_{22} (dB) of the antenna. These changes can be attributed to the influence of concrete in E-field of the embedded patch antenna since dimensions of the superstrate and air box are selected to be relatively small, i.e., less than wavelength, to avoid destruction of

62

concrete integrity. Then, applying the rebar cell in concrete does not change the resonant frequency and the magnitude of the reflection coefficient of the antenna. However, measured results which are shown in Fig. 3.24(b) demonstrate negligible shift of the resonant frequency under the influence of concrete and the rebar cell on the magnitude of the reflection coefficient. This discrepancy between simulated and measured results can be explained by the antenna fabrication errors and/or the influence of concrete and the rebar cell on radiation from a connector which is attached to the antenna and connected to the cable.

(a)

(b)
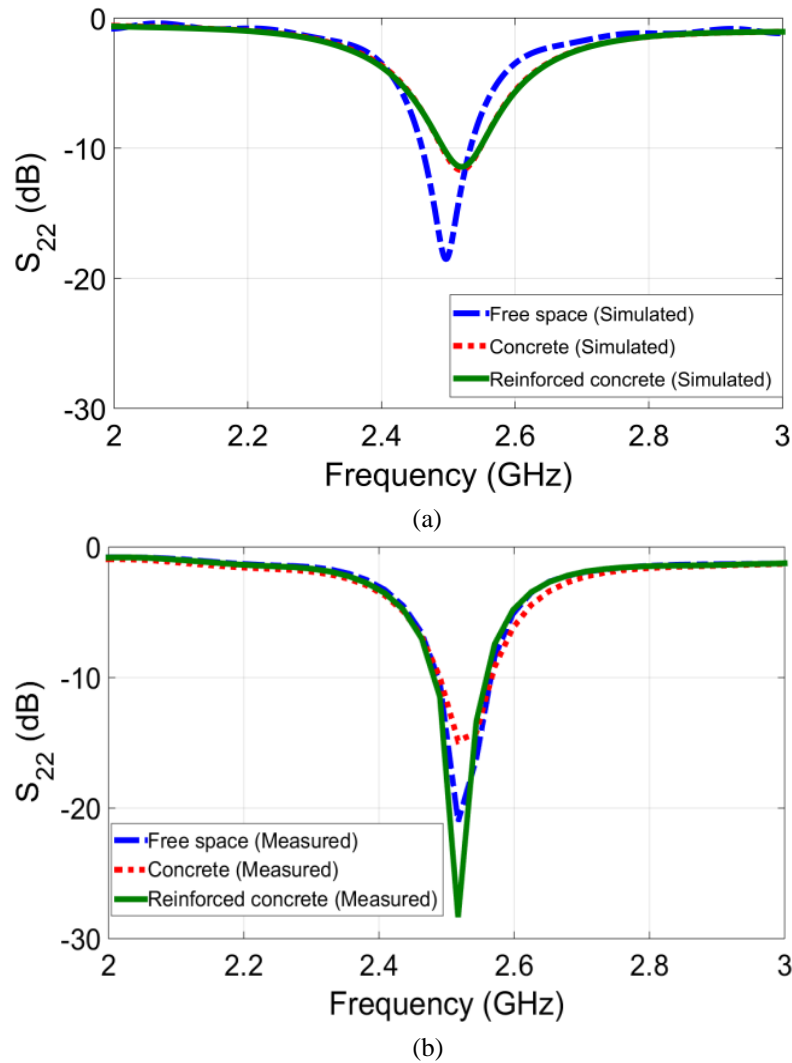
Figure 3.24 Magnitude of the reflection coefficient of the patch antenna in free space, concrete and reinforced concrete samples ($d = 50$ mm) (a) simulated S_{22} (dB) and (b) measured S_{22} (dB).

Fig. 3.25 and Fig. 3.26 show simulated and measured magnitude of the transmission coefficient, S_{21}, in the two-antenna system in free space, and with concrete and reinforced concrete samples at three distances between the MAVA and the surface of concrete. It can be seen from Fig. 3.25 that maximum value of the simulated S_{21} in free space is -15 dB at ~2.45 GHz (i.e., at the resonant frequency) and embedding patch antenna in concrete and applying the rebar cell do not change it at d = 0 as shown in Fig. 3.25(a). The maximum magnitude with the concrete and reinforced concrete samples slightly decreases at d = 50 mm and a notable decrease of the magnitude is observed at d = 100 mm. Fig. 3.25 also shows that the changes of the magnitude in the concrete and reinforced concrete samples are almost the same. This observation leads to the conclusion that the influence of concrete boundaries, in particular, the top surface of the samples is the main contributing factor to changes of transmission property of the samples. The measured results shown in Fig. 3.26 confirm the main features and behavior of the maximum magnitude of the transmission coefficient, which have been observed from the simulated results. It should be noted that the magnitude of transmission coefficient is lower in the measurement than in the simulation (c.f. Fig. 3.25) and it can be attributed to losses in the cable, which were not taken into account in the simulation.
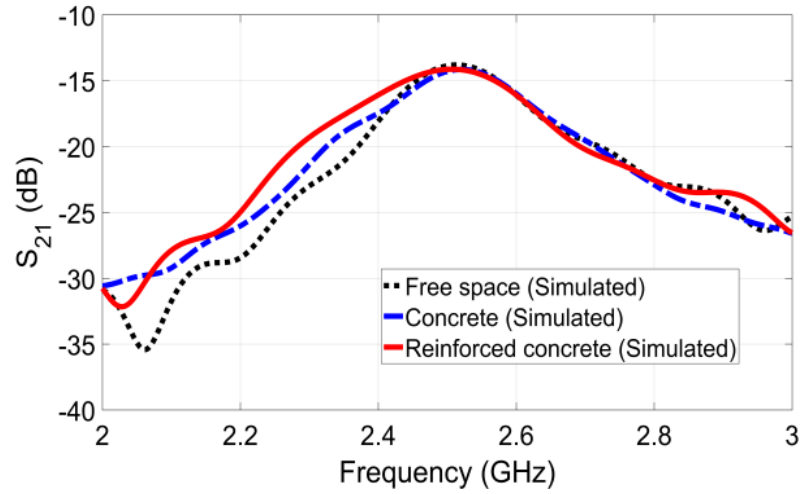
(a)
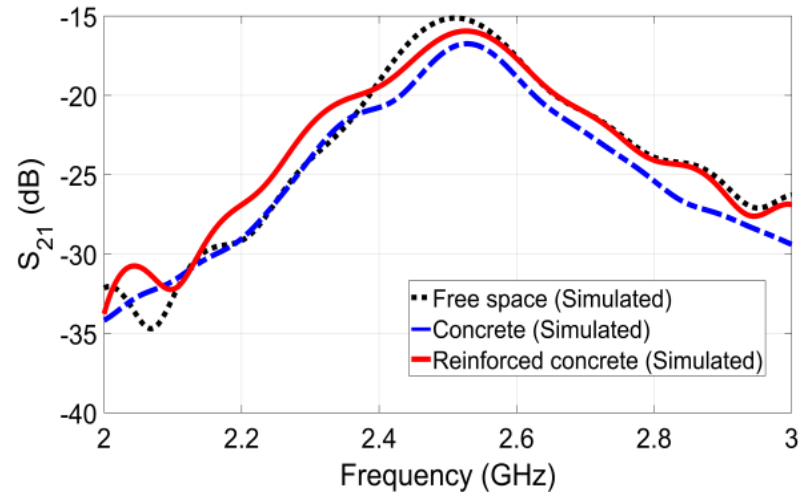
(b)
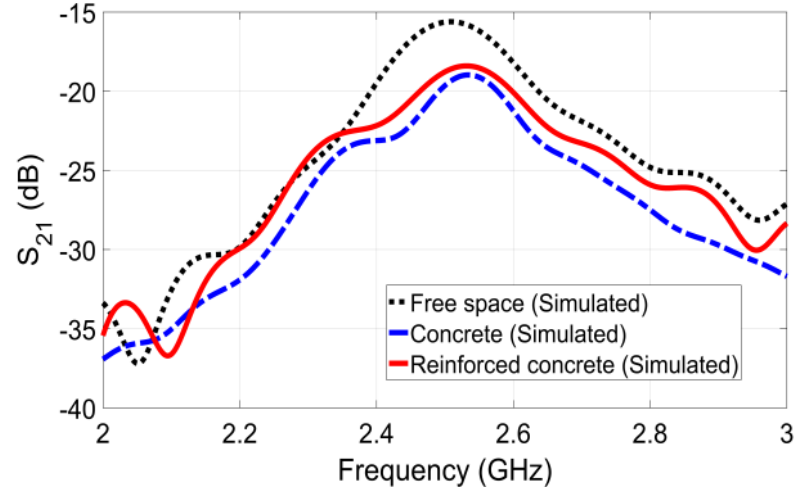
(c)

Figure 3.25 Simulated magnitudes of the transmission coefficient between antennas in free space, concrete and reinforced concrete at (a) $d = 0$, (b) $d = 50$ mm, and (c) $d = 100$ mm.
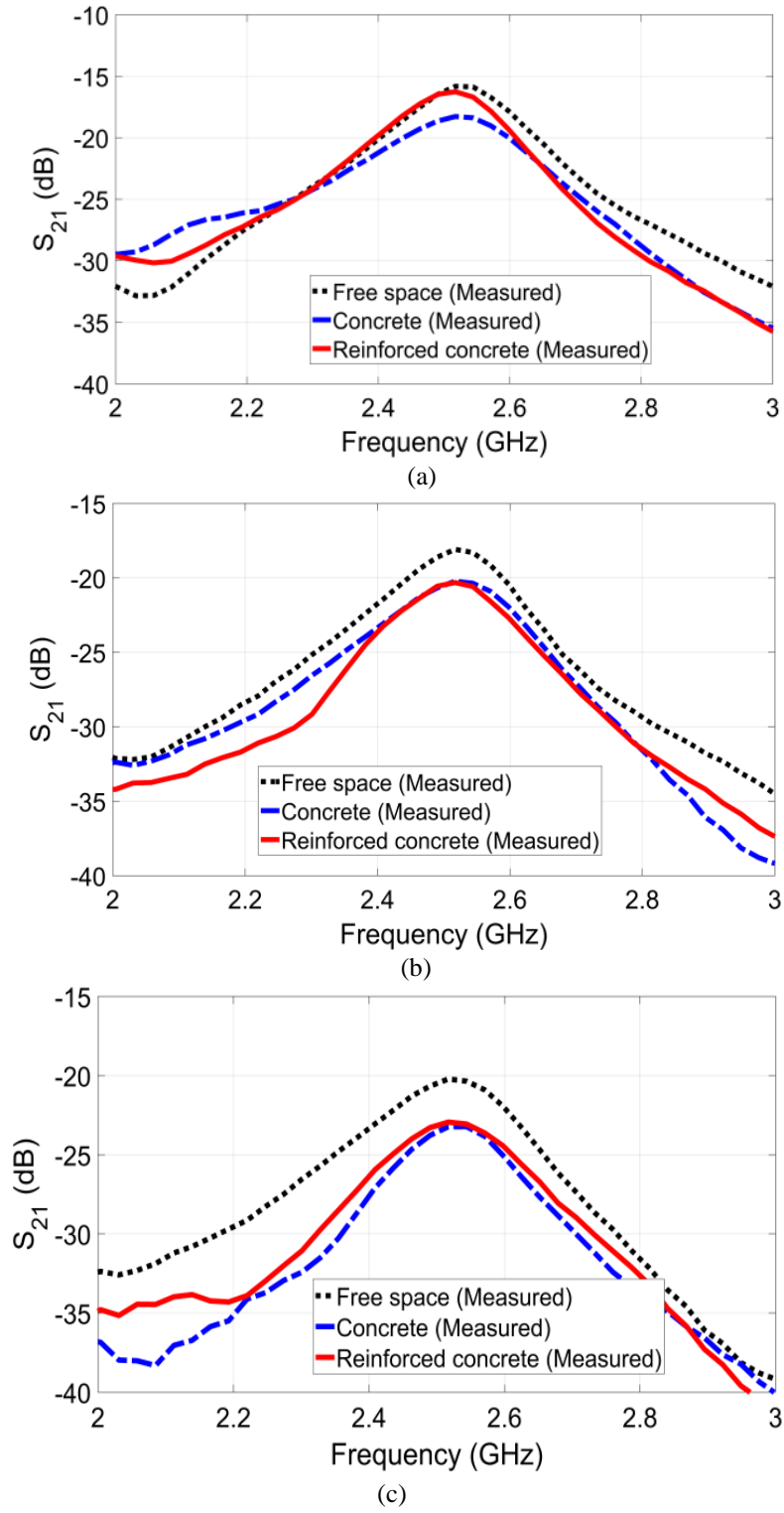
Figure 3.26 Measured magnitudes of the transmission coefficient between antennas in free space, concrete and reinforced concrete at (a) $d = 0$, (b) $d = 50$ mm, and (c) $d = 100$ mm.

The influence of parameter g of the rebar cell on the magnitude of the transmission coefficient has been investigated numerically at the range from 90 mm to 170 mm and the results are shown in Figs. 3.27. It can be observed from Figs. 3.27 that the decrease of g from 170 mm to 150 mm decreases the magnitude, then it increases gradually when g decreases from 150 mm to 90 mm, reaching the maximum value at $g = 90$ mm which, as expected, is equal to the simulated maximum magnitude shown in Fig. 3.25(b). The measurements were conducted with practical values of $g = 90$ mm and 110 mm at three values of d as shown in Fig. 3.28. It can be seen from Fig. 3.29 that the increase of d causes the decreasing of S_{21} while the change of g from 90 mm to 110 mm leads to negligible changing of on the maximum magnitude of S_{21}. The results also demonstrate that the measured maximum S_{21} in Fig. 3.28 is less than the simulated maximum S_{21} in Fig. 3.27, and the maximum S_{21} for each d in Fig. 3.29 corresponds to the measured results shown in Fig. 3.26.
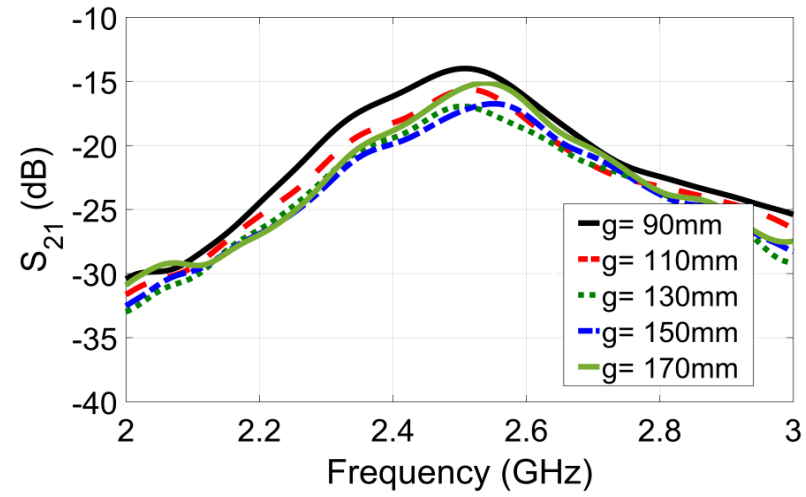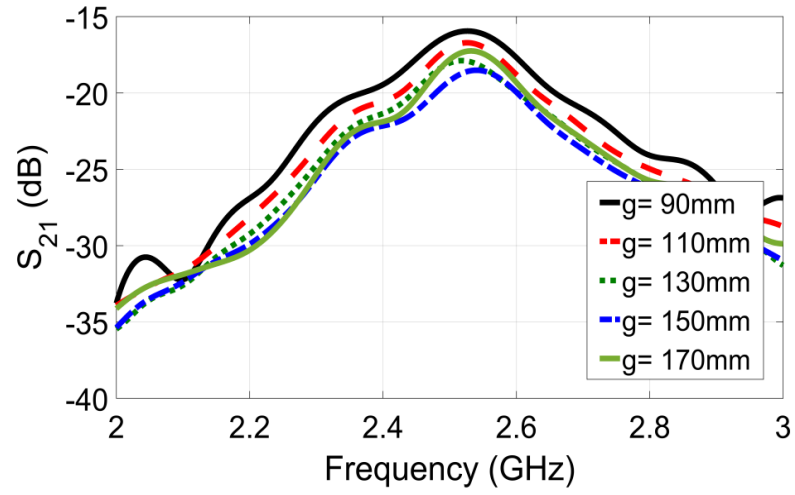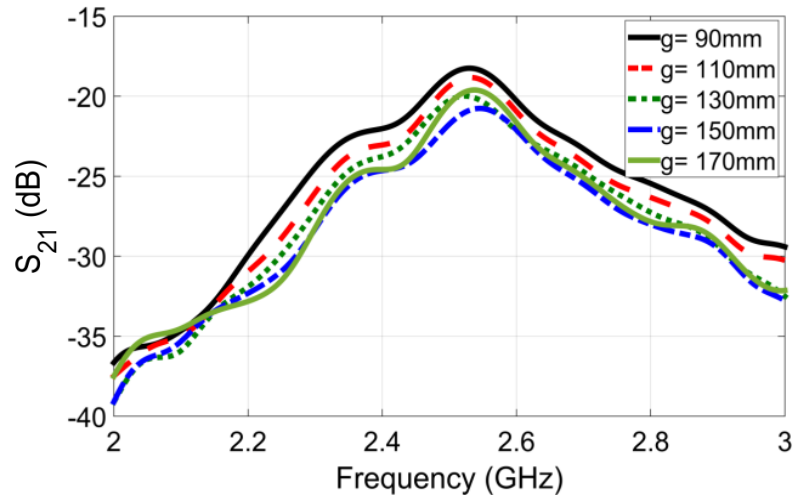
Figure 3.27 Simulated magnitude of the transmission coefficient of the two-antenna system with the reinforced concrete sample and different values of g (a) $d = 0$ mm, (b) $d = 50$ mm, and (c) $d = 100$ mm.
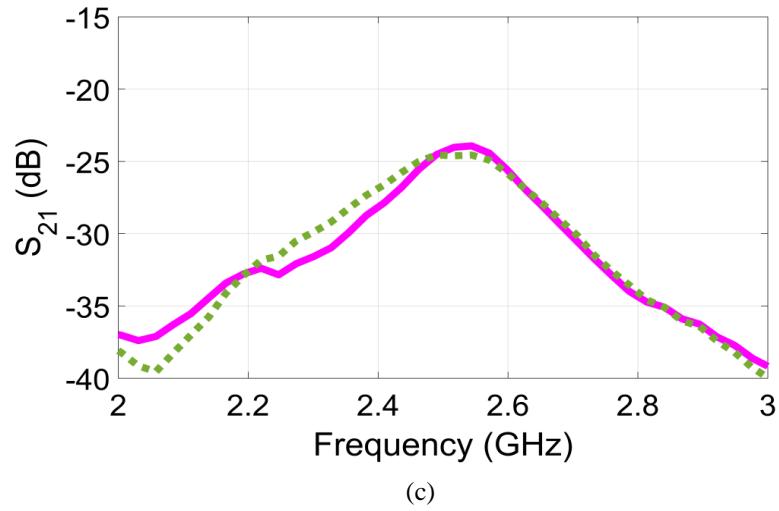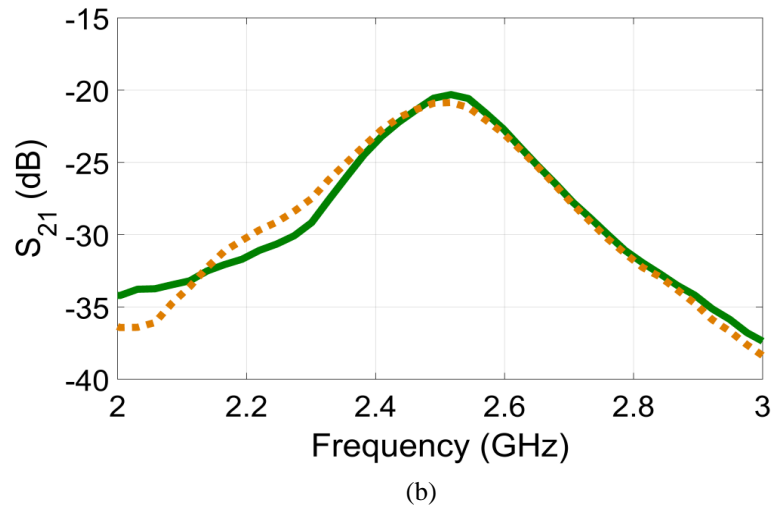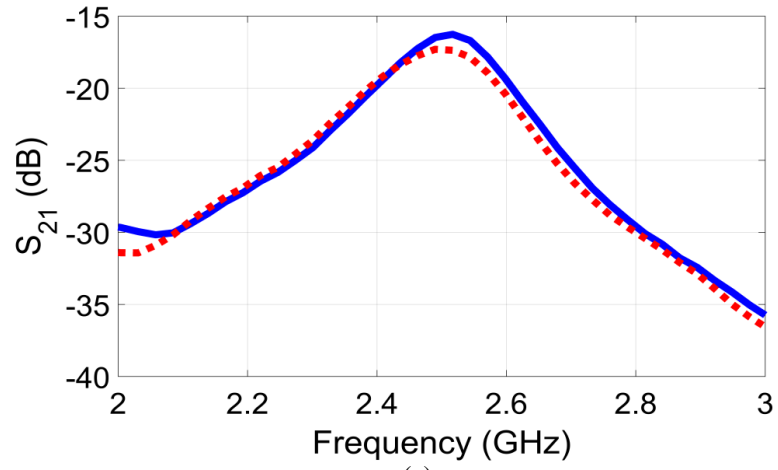
Figure 3.28 Measured S_{21} at (a) $d = 0$, (b) $d = 50$ mm and (c) $d = 100$ mm at two values of g: 90 mm (solid line) and 110 mm (dash line).

Fig. 3.29 shows the simulated and measured magnitude of the transmission coefficient of the two-antenna system with the reinforced concrete sample possessing the rebar cell when an upper layer of rebars is parallel (case 1) or vertical (case 2) to the E-field polarisation vector of the antennas at $d = 0$ and 50 mm . The model for case 1 is shown in Fig. 3.23(a). It can be seen from Fig. 3.29 that there is no difference between maximum values of S_{21} obtained at case 1 and case 2 for both the simulated and measured results.

(a)

(b)
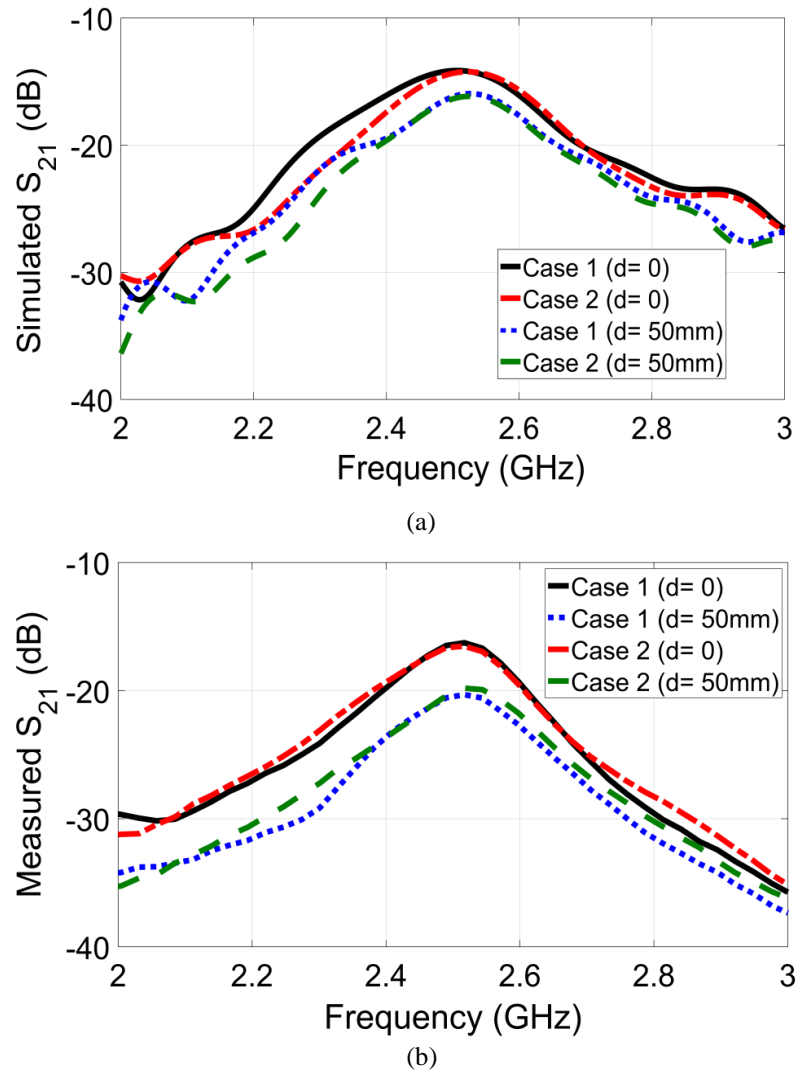
Figure 3.29 Magnitude of the transmission coefficient of the two-antenna system with the reinforced concrete sample possessing the rebar cell when an upper layer of rebars is parallel (case 1) or vertical (case 2) to the E-field polarisation vector of the antennas at $d = 0$ and 50 mm (a) simulated S_{21}, and (b) measured S_{21}.

3.7 Summary

The modified antipodal Vivaldi antenna (MAVA) is designed, built and tested to be used for IHM techniques at frequency range from 0.65 GHz – 6 GHz. The antenna is applied to investigate the reflection and transmission properties of concrete-based samples possessing air gap or rebars numerically and experimentally at frequency range from 0.65 GHz - 3.5 GHz.

It is shown that the reflection from the top of the samples with and without air gap or rebars provided the most critical effect on the change of reflection from or reduction of power transmission in the samples. The results show that the air gap of > 5 mm can be detected at any depth inside 500-mm thick concrete samples. The gap (not "crack") was invisible to the naked eye and it was detected through concrete at different distances from the top of specimen to its location.

The investigation into the influence of rebars show that it depended on the value of rebar cell parameter and the rebar cell mesh could act as a shield for microwaves if this parameter was less than the electrical half wavelength. At higher frequencies of the frequency range, microwaves could penetrate through the reinforced concrete samples with a rebar cell with the parameter used in practice. These results is used for the investigation into the transmission of microwaves at single frequency of 2.45 GHz between the MAVA and a microstrip patch antenna embedded inside dry reinforced concrete samples at the location of the rebar cell. It is shown that -15 dB coupling between the antennas can be achieved.

Chapter 4 Resonant antipodal Vivaldi antenna for wireless power transfer in concrete

4.1 Introduction

In this chapter, a relatively small resonant antipodal Vivaldi antenna (RAVA) was designed to operate as an external transmitting antenna for WPT in concrete at 2.45 GHz. Feasibility of a two-antenna setup including the RAVA and a modified microstrip patch antenna as a receiving antenna embedded in reinforced concrete members is investigated numerically. Parametric study on the most critical parameters of the members such as reinforced concrete slab and column, which affect electromagnetic wave propagation in these members, is performed.

4.2 Configuration and performance of RAVA and modified patch antenna in free space

The proposed antennas are designed to operate at the resonant frequency of 2.45 GHz (i.e., at the ISM band) and their schematics are shown in Fig. 4.1. The RAVA is based on a relatively small broadband conventional AVA but a resonance is added to get to the operating frequency at 2.45 GHz with reduced dimensions of the antenna and for potential applications of higher frequency for wireless communication, sensing and/or power transmission in relatively low loss materials. Both antennas are printed on RO4003C with relative dielectric permittivity of 3.38 and loss tangent of 0.0027. The substrate thickness of the RAVA and the patch antenna are 0.813 mm and 1.524 mm, respectively. The RAVA and the patch antenna are fed by a microstrip line with width of W_f and W_{f1}, respectively, in order to match 50 Ω, as shown in Fig. 4.1.
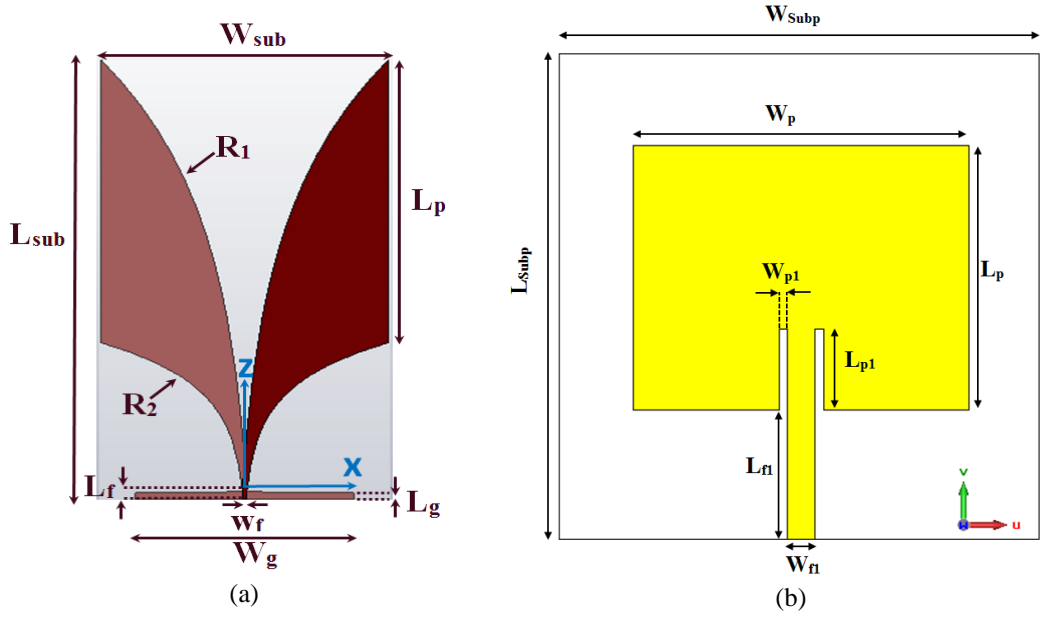
Figure 4.1 Schematic of the (a) RAVA and (b) microstrip patch antenna.

To design the exponential taper profile of the proposed RAVA (see Fig. 4.1(a)) the following equations were used:

$$X = \pm(C_1 e^{R_n z} + C_2) \qquad (4.1)$$

$$C_1 = \frac{x_2 - x_1}{e^{R_n z_2} - e^{R_n z_1}} \qquad (4.2)$$

$$C_2 = \frac{x_1 e^{R_n z_2} - x_2 e^{R_n z_1}}{e^{R_n z_2} - e^{R_n z_1}} \qquad (4.3)$$

where R_n is the rate of opening, and (x_1, z_1) and (x_2, z_2) are the peak and bottom points of the exponential tapered curve.

To obtain the desired performance of the RAVA extensive parametric studies on the dimensions were performed. For example, the influence of changes of R_1 on the magnitude of reflection coefficient and gain of the RAVA is shown at Fig. 4.2. It can be seen from Fig. 4.2(a) that the RAVA acts as a resonant antenna at lower frequency (< 3 GHz). The resonant frequencies increase as the R_1 increases from 0.01 to 0.02 and it has acceptable value ($<$-10 dB) over desired 2.45 GHz resonant frequency at $R_1=$

73

0.014. As shown in Fig. 4.2(b), at lower resonant frequencies the gain of the RAVA increases as the R_1 increase.

(a)

(b)
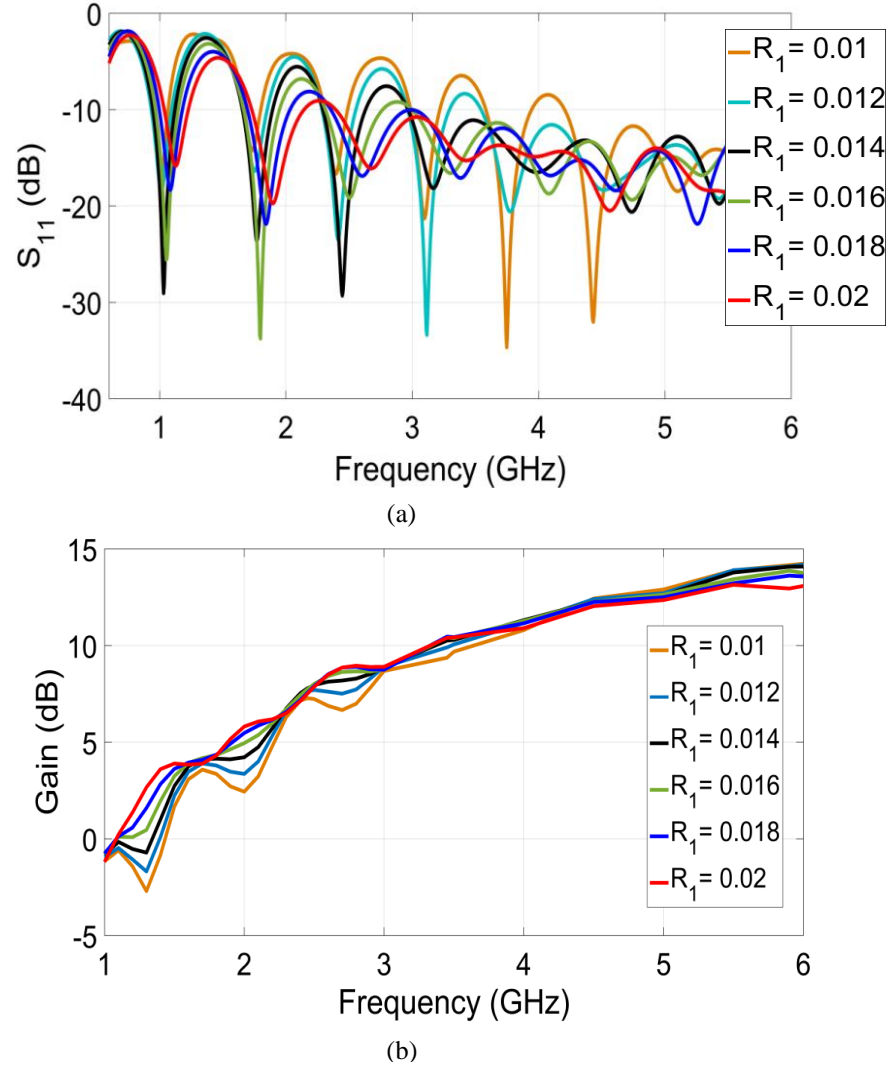
Figure 4.2 (a) Magnitude of the reflection coefficient and (b) gain of the RAVA with different R_1 (no unit).

As a result, the optimised dimensions of the proposed RAVA are: $L_{sub} = 202$ mm, $W_{sub} = 120$ mm, $L_p = 130$ mm, $W_g = 90$ mm, $W_f = 1.9$ mm, $L_f = L_g = 4$ mm, $R_1 = 0.014$ and $R_2 = 0.051$ (no unit). The magnitude of the reflection coefficient and gain of the RAVA at 2.45 GHz are shown in Fig. 4.3. The gain of the proposed RAVA at 2.45 GHz is 8.05 dB. The simulated 3D radiation patterns and co-polarsation radiation patterns of the RAVA in both E- and H-planes at 2.45 GHz are presented in Fig. 4.4.
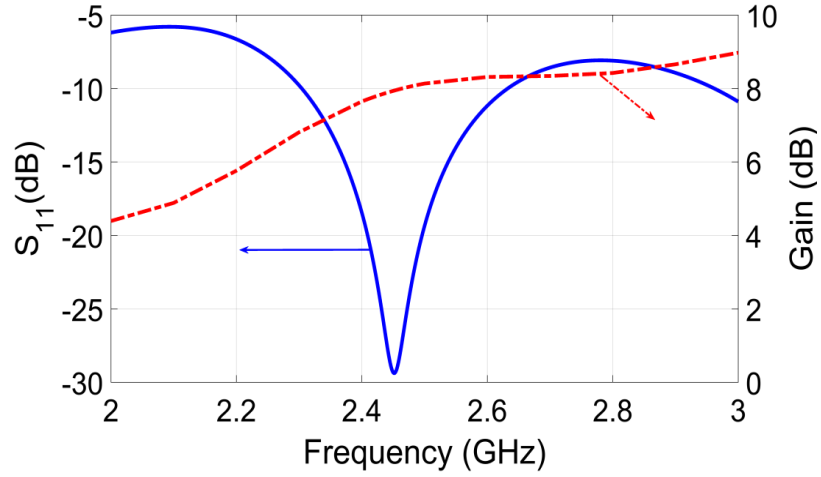
Figure 4. 3 Simulated magnitude of the reflection coefficient and gain of the proposed RAVA.

(a) (b) (c)
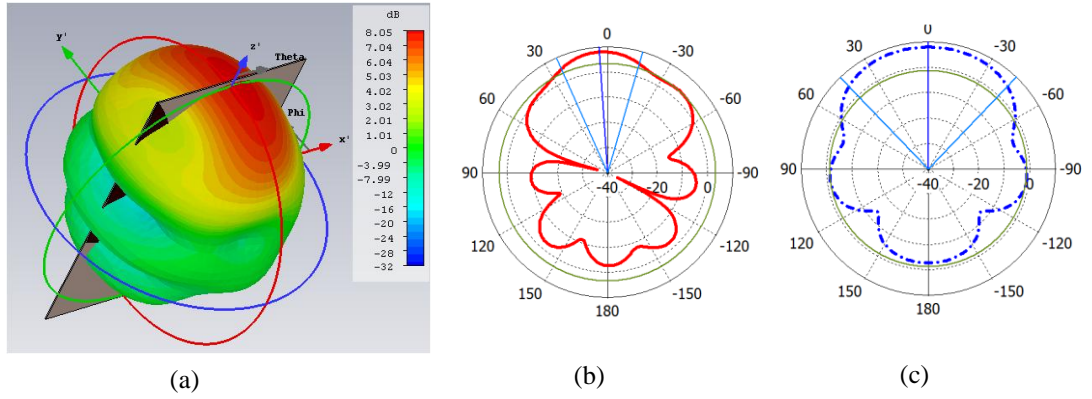
Figure 4.4 (a) 3D, (b) E-plane, and (c) H-plane radiation patterns of the RAVA at 2.45 GHz.

The width and length of the microstrip patch antenna is calculated using Eqs. 3.6- 3.9. As a result, the optimized dimensions of the patch antenna are: $W_{subp} = L_{subp} = 60$ mm, $W_P = 41.4$ mm, $L_P = 32.6$ mm, $L_{P1} = 12$ mm, $W_{P1} = 0.3$ mm, $L_{f1} = 16$ mm and $W_{f1} = 3.5$ mm. Magnitude of the reflection coefficient (S_{22}) and gain of the patch antenna in free space are shown in Fig. 4.5. A maximum gain of 6 dBi is observed. The simulated 3D, E- and H-plane radiation patterns of the patch antenna are shown in Fig. 4.6.
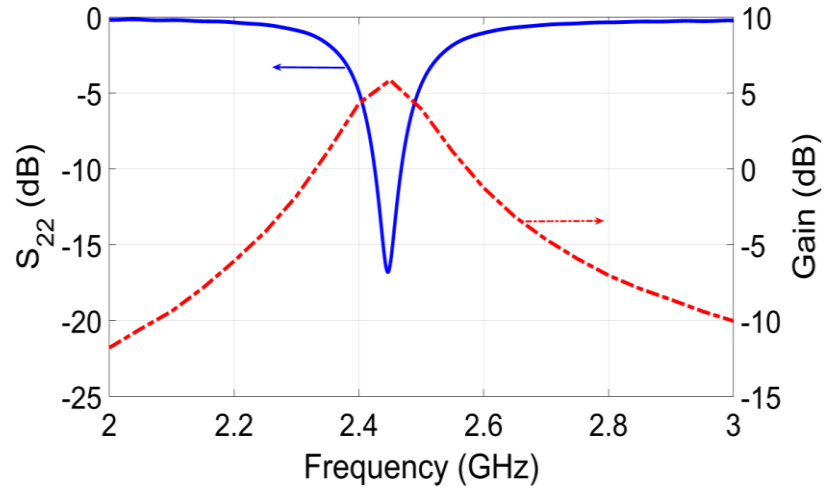
Figure 4. 5 Simulated magnitude of the reflection coefficient and gain of the patch antenna.

(a)

(b)

(c)
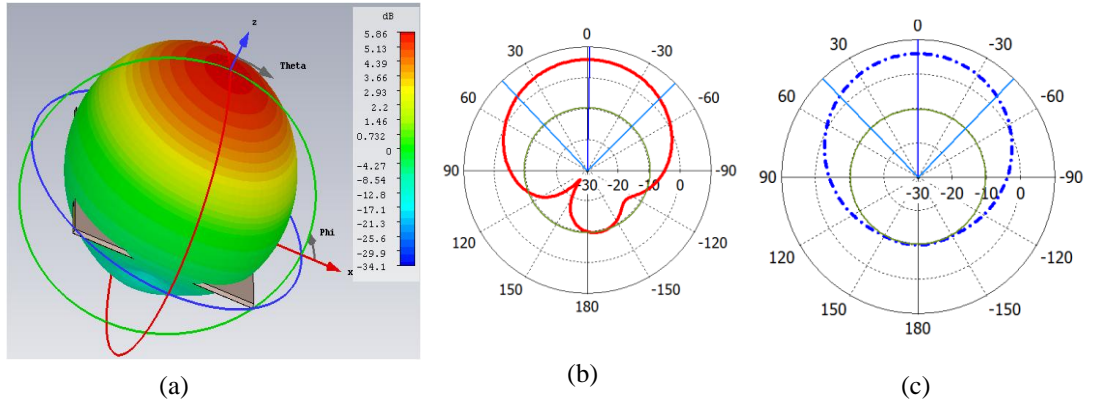
Figure 4.6 (a) 3D, (b) E-plane, and (c) H-plane radiation patterns of the patch antenna at 2.45GHz.

Magnitude of the reflection coefficients of the RAVA (S_{11}) and the patch antenna (S_{22}), and the gain of antennas in free space are shown in Fig. 4.7. It can be clearly seen from Fig. 4.7 that the both antennas resonate at 2.45 GHz. The results also show that the gain of the RAVA at the resonant frequency is almost 3.3 dB higher than the gain of the patch antenna. The RAVA provides higher bandwidth than the patch antenna and operates from 2.3 GHz to 2.6 GHz when using S_{11} = -10 dB as a criterion.
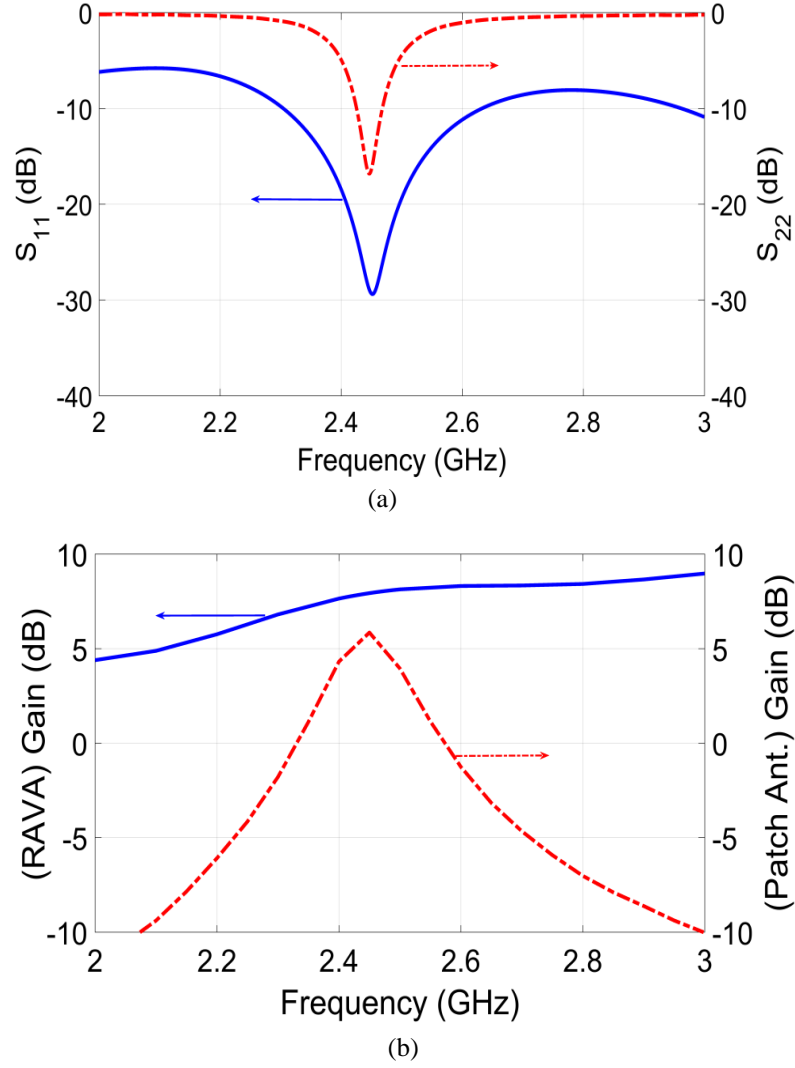
Figure 4.7 (a) Magnitude of the reflection coefficient and (b) gain of the RAVA and patch antenna (without superstrate) from 2 GHz to 3 GHz at free space.

The patch antenna will be used as a receiving antenna embedded inside concrete. In order to reduce the influence of surrounding material on the performance of the embedded antenna, it is covered by two layers made of Teflon with relative dielectric permittivity of 2.1, loss tangent of 0.0002 and thickness of h_1 bonded to top and bottom sides of the antenna substrate (referred to as superstrate). Firstly, a parametric study is performed to analyse the influence of different thicknesses of superstrate on the magnitude of the reflection and gain of the patch antenna while the patch antenna is located at free space as shown in Fig. 4.8. Secondly, a parametric study is performed to analyse the influence of concrete on the performance of embedded patch antenna

with different thicknesses of the superstrate, which will be discussed in the following

section.

(a)

(b)
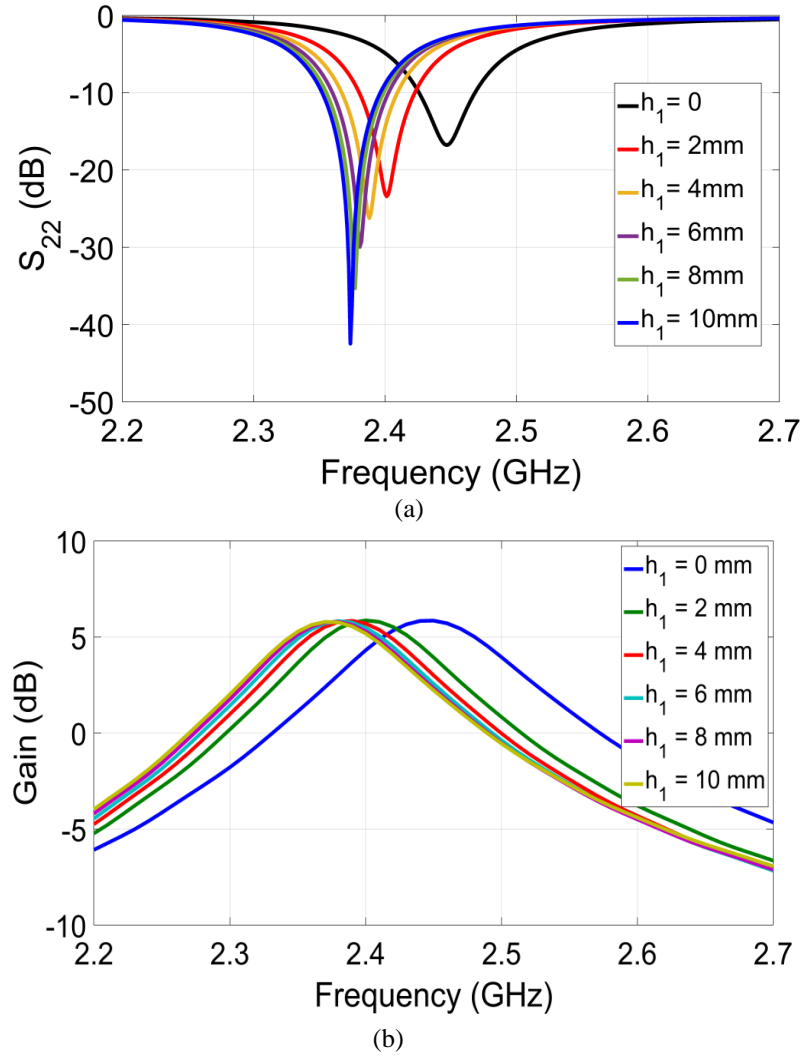
Figure 4.8 (a) Influence of the different thicknesses of the superstate on magnitude of the reflection coefficient and (b) gain of the patch antenna at free space ($L_P = 32.6$ mm).

It can be seen from Fig. 4.8(a), the resonant frequency of the patch antenna is shifted to lower frequency by increasing the thickness of superstrate. For instance, at $h_1 = 10$ mm, the resonant frequency is 2.38 GHz. The results in Fig. 4.8 (b) show that the gain of the patch antenna at the resonant frequency is constant at any selected h_1. In order to achieve the 2.45 GHz resonant frequency while the patch antenna covered by 10 mm superstrate, the parametric study on L_P is performed as shown in Fig. 4.9.

As illustrated in Fig. 4.9, the resonant frequency of the patch antenna with superstrate is shifted toward 2.45 GHz by decreasing the L_P. The 2.45 GHz resonant frequency is achieved while the L_P is equal to 31.6 mm. Therefore, the proposed patch antenna covered by superstrate with L_p= 31.6 mm will be embedded inside concrete in the following section. Fig. 4.10 shows the simulated 3D pattern and radiation patterns at E- and H-planes of the patch antenna with the superstrate.
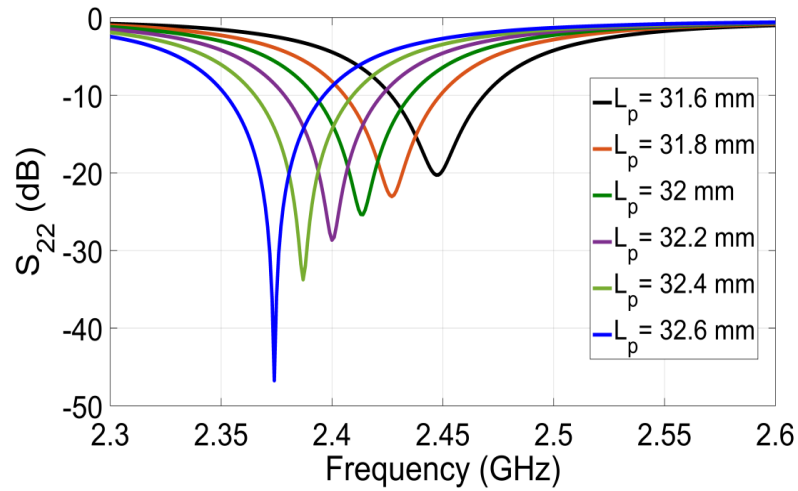
Figure 4.9 Magnitude of the reflection coefficient of the patch antenna covered by superstrate with different values of the L_P at free space (h_1=10 mm).

(a)   (b)   (c)
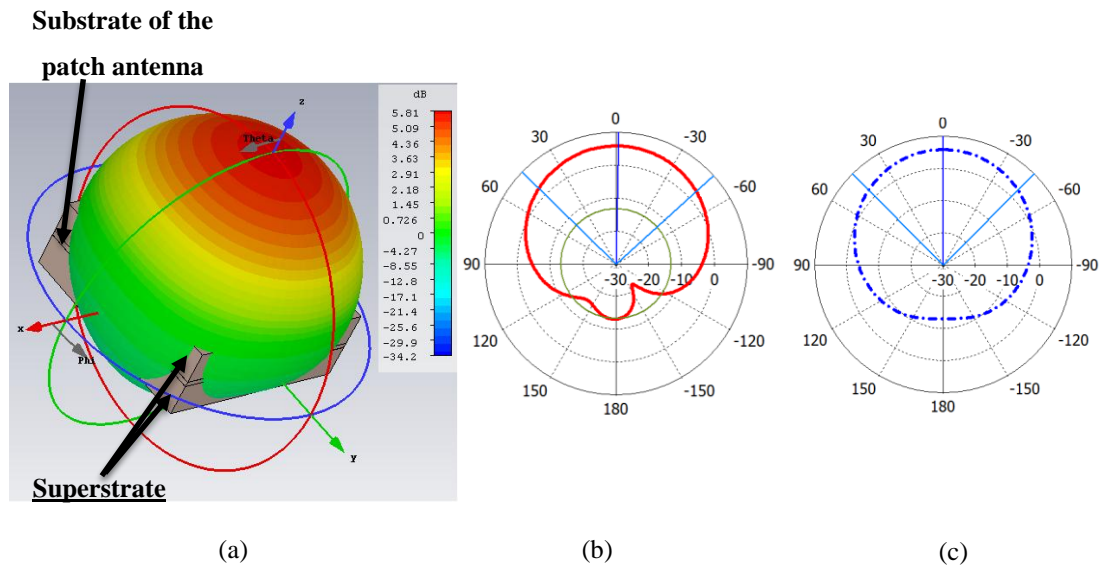
Figure 4.10 Radiation patterns of the patch antenna with superstrate at 2.45 GHz: (a) 3D, (b) E-plane, and (c) H-plane.

4.3 Reflection and transmission properties of reinforced concrete slab and column irradiated by RAVA

4.3.1 Reinforced concrete slab

Fig. 4.11 shows schematic of a reinforced concrete slab with two cross rebar layers which is widely used in building structures such as reinforced concrete walls and bridge decks. The metal rebars used for increasing strength and serviceability of concrete may affect the performance of the embedded antenna as well as the WPT in the reinforced concrete for IHM applications. In this investigation, the reinforced concrete slab and the two-antenna setup were modeled in CST as shown in Fig. 4.12 and distances between the concrete surface and the RAVA (L_1) and the microstrip patch antenna (L_2), and mesh period (g) of rebar cell were parameters in numerical study.
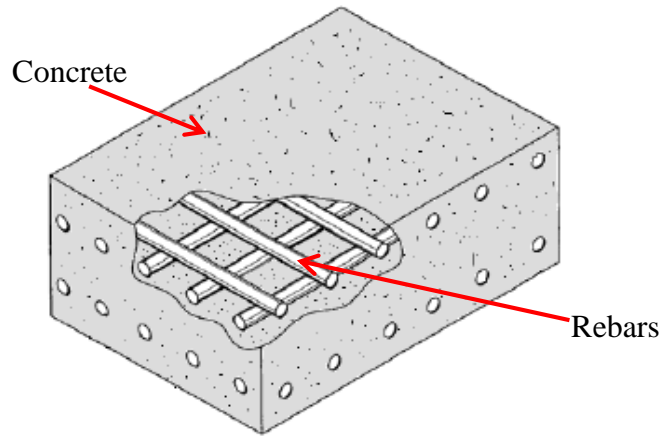
Figure 4.11 Reinforced concrete slab (Jiang & Georgakopoulos 2011) .

As previously mentioned, the complex permittivity of concrete varies with both the frequency and the moisture content. At any given frequency both dielectric constant and conductivity increase as moisture content increases (Buyukozturk 1997; Maierhofer & Wöstmann 1998; Shaari, Millard & Bungey 2004; Soutsos et al. 2001).
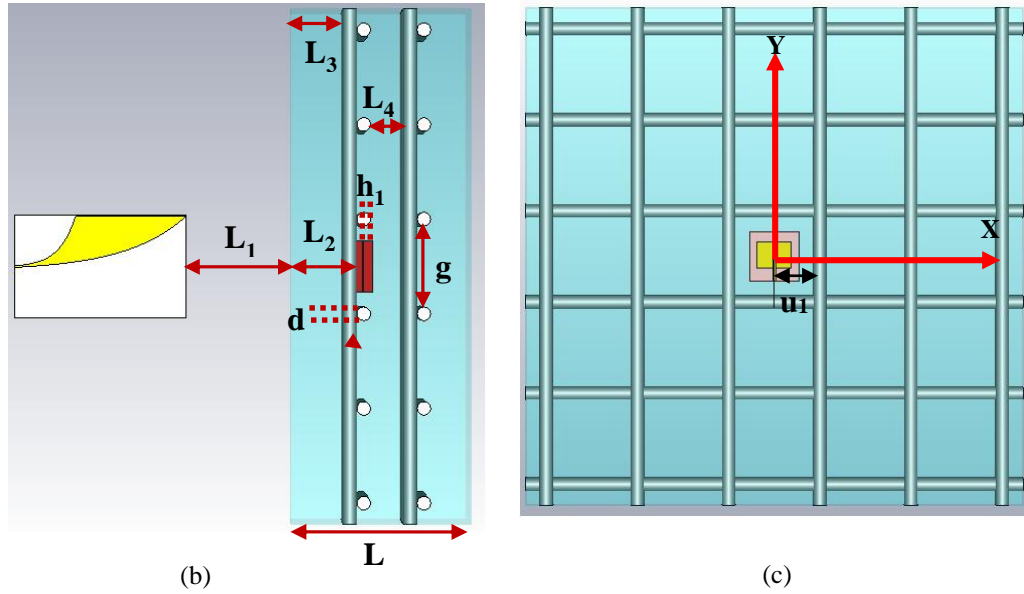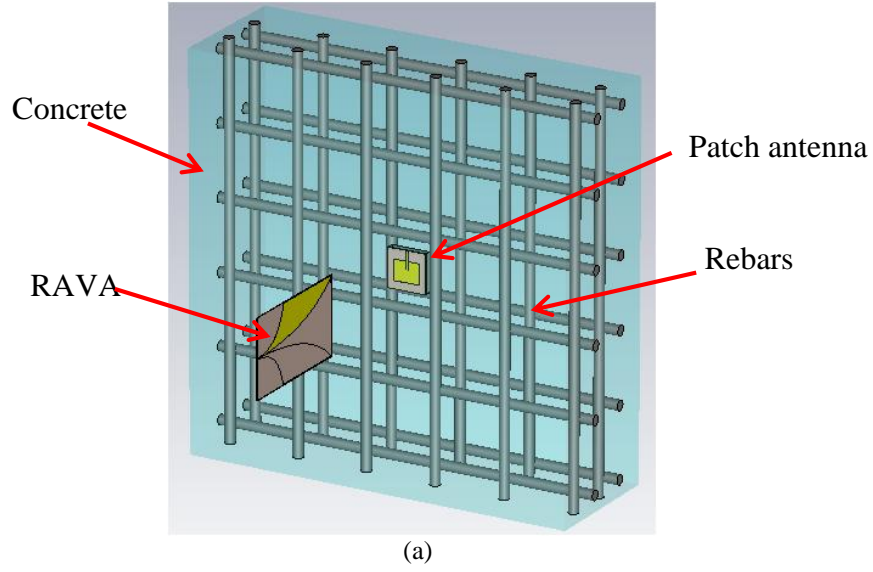
Figure 4.12 Model of the antennas and reinforced concrete slab in CST: (a) perspective view, (b) side view and (c) front view (L = 210 mm, L_3 = 77 mm, L_4 = 38 mm, d = 16 mm).

The dielectric permittivity of four different groups of concrete such as wet, saturated, air-dried and oven-dried are available in (Buyukozturk 1997). The air-dried and saturated concrete are chosen to be used in this section. The electromagnetic properties of air-dried and saturated concrete at 2.45 GHz are listed in Table 4.1. The term saturated means that the surface of concrete specimen is dry however there is moisture inside and it is significantly higher than air-dried concrete moisture content.

Table 4. 1 Measured relative permittivity of concrete at 2.45 GHz (Buyukozturk 1997).

Concrete	Air-died	Saturated
Dielectric constant, ε_r	4.5	8.1
Conductivity, σ	0.013	0.13
Loss tangent, tan δ	0.0212	0.1178

A parametric study is performed to analyse the influence of concrete on the performance of embedded patch antenna. Figs. 4.13(b)-(c) show the resonant response of the patch antenna embedded in the dry and saturated concrete slabs, respectively, with different thicknesses of the superstrate, h_1. It can be seen from Fig. 4.13 that the resonant frequency and magnitude of the reflection coefficient S_{22} change when h_1 increases from 0 mm to 15 mm. The changes of S_{22} can be attributed to changes of coupling between the patch antenna and the microstrip feed due to different losses in the antenna (i.e., its loaded Q factor changes) when h_1 changes. The results demonstrate that when the embedded patch antenna is not covered by the superstrate ($h_1 = 0$) its resonant frequency for the dry concrete is significantly lower than it is in free space (i.e., 2.45 GHz) as shown in Fig. 4.13(a) while there is no resonant response of the patch antenna in the saturated concrete. The effects of the dry and saturated concrete on the resonant frequency of the patch antenna were considered in detail and the results are shown in Fig. 4.14. It can be seen from Fig. 4.14 that a shift of the resonant frequency is larger for the saturated concrete than for the dry concrete at h_1 from 1 mm to ~3 mm. Then, by increasing h_1 from 3 mm to 9 mm, the resonant frequency is shifted gradually to 2.45 GHz, and remains constant at h_1 from 9 mm to 15 mm for both the dry and saturated concrete. Therefore, the thickness of h_1 is chosen to be 10 mm in following investigations.
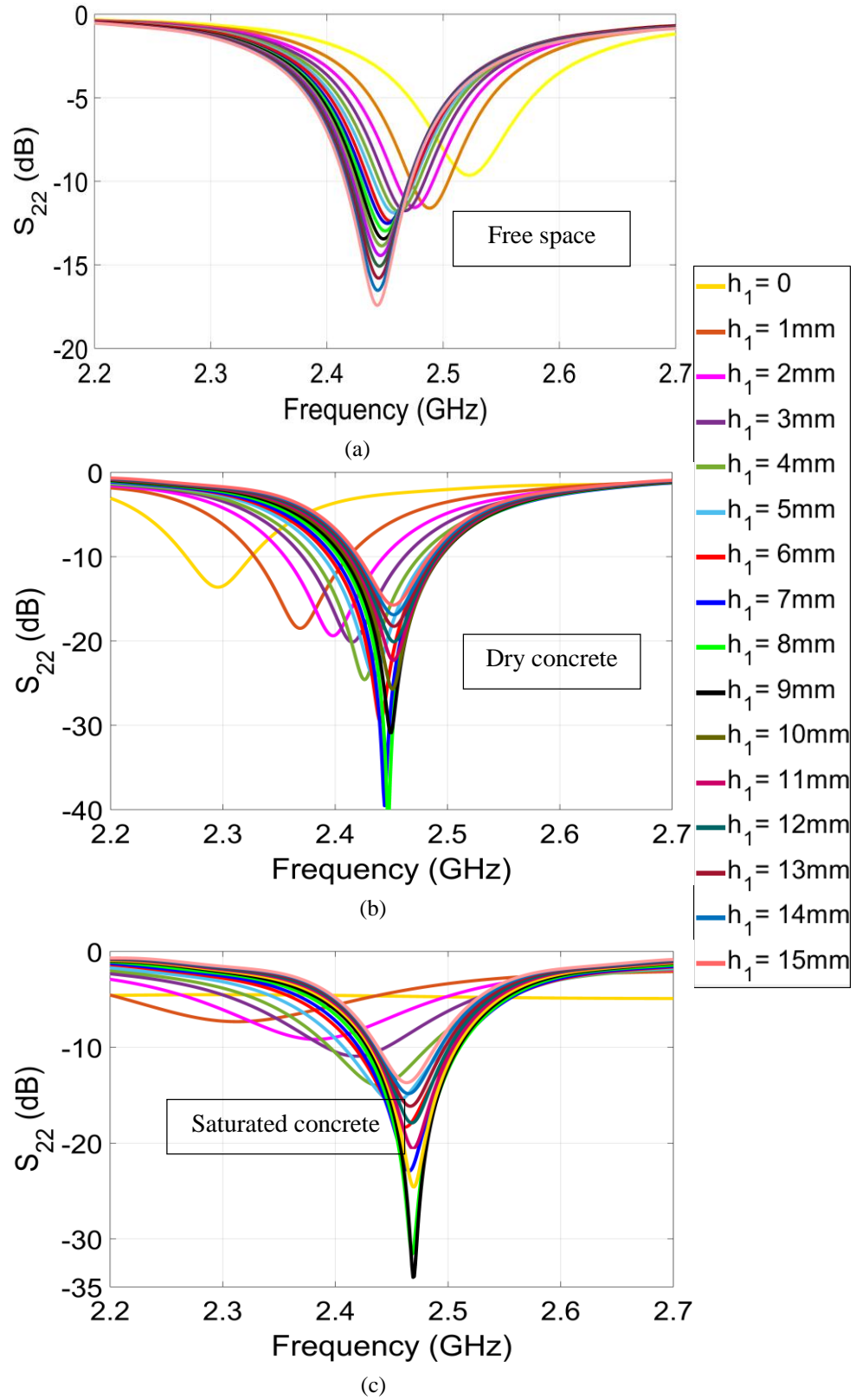
Figure 4.13 Magnitude of the reflection coefficient of the patch antenna embedded in the (a) free space, (b) dry and (c) saturated concrete at different values of the superstate's thickness.
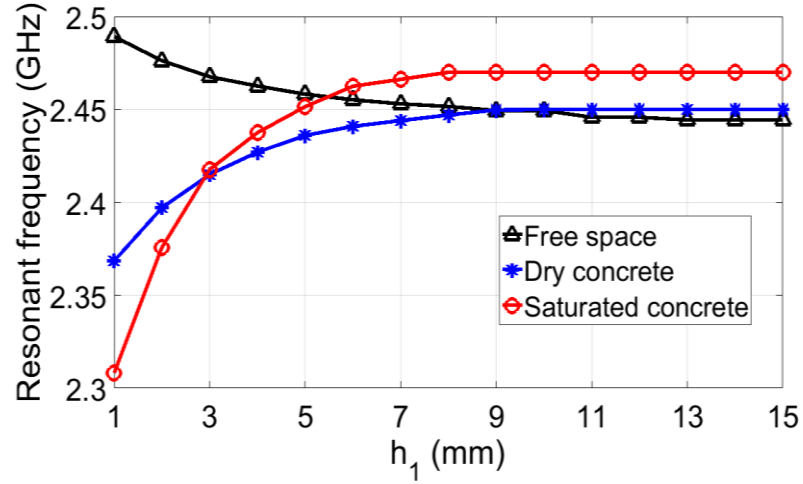
Figure 4.14 The resonant frequency of the patch antenna versus h_1 in the free space, the dry and saturated concrete.

The effects of the concrete and rebars on magnitude of the reflection coefficients of the antennas and transmission coefficient between antennas at $L_2 = 82$ mm and $g = 110$ mm are demonstrated in Fig. 4.15. As can be seen from Fig. 4.15(a), the resonant frequency and magnitude of the reflection coefficient of the receiving patch antenna are slightly changed by applying the concrete and rebars, as expected (see Fig. 4.14). On the other hand, changes of the resonant frequency of the RAVA are negligible while its magnitude of the reflection coefficient changes under the influence of concrete and rebars are visible due to the reflection of EM waves from the interface between free space and concrete, and from the rebars.

Fig. 4.15(b) shows the magnitude of transmission coefficient related to coupling between the two antennas when the RAVA is in free space while the patch antenna is located in the free space, concrete slab or reinforced concrete slab. It can be seen from Fig. 4.15(b) that maximum S_{21} is achieved at the resonant frequency of RAVA at all cases. The coupling between antennas decreases when the concrete is applied, as expected; however, it increases when rebars are inserted inside concrete. To understand this behaviour of wave propagation in the reinforced concrete slab parametric study was performed and its results will be presented in the next sections.
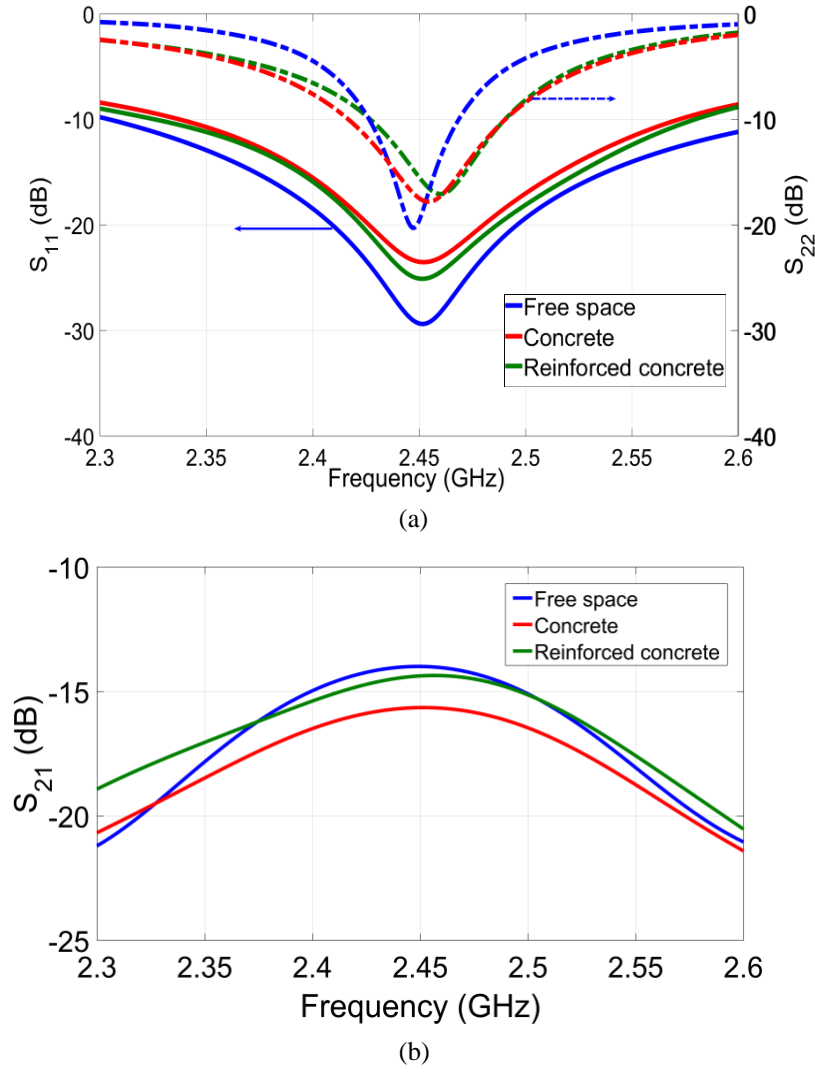
Figure 4.15 Magnitude of the (a) reflection coefficients of the RAVA (S_{11}) (shown by solid line) and the patch antenna (S_{22}) (shown by dash line) and (b) the transmission coefficient between the antennas (S_{21}) at $L_1 = 122.5$ mm and $L_2 = 82$ mm.

4.3.1.1 Parametric study on value of mesh period

In practice, a value of mesh period, g, in reinforced concrete slab design is in the range from 100 mm to 305 mm (Jiang & Georgakopoulos 2011). To analyse the influence of g on the resonant frequency of the antenna embedded in the dry and saturated concrete, and coupling between the antennas, a parametric study is performed when the g is in the range from 55 mm to 300 mm as shown in Fig. 4.16. Fig. 4.16(a) shows that at g = 55 mm - 85 mm the resonant frequency of the patch antenna embedded inside the

dry and saturated concrete reveals downward and upward sloping trends, respectively; and then from 95 mm to 300 mm, remains constant at slightly different levels, i.e., almost at 2.45 GHz for dry concrete and 2.48 GHz for saturated concrete. Fig. 4.16 also shows that there is a similarity between the resonant frequency and the coupling trends. When the resonant frequency increases or decreases (c.f. Fig. 4.16(a)), there is also an increase or decrease in the coupling and maximum coupling is achieved at the highest and lowest resonant frequencies for the saturated and the dry concrete, respectively (c.f. Figs. 4.16(a)-(b)). As an overall view, it is clear that coupling between antennas is significantly lower in the saturated reinforced concrete slab than in the dry reinforced concrete slab. However, the Fig. 4.16(b) shows that maximum coupling is achieved for both the dry and saturated reinforced concrete at $g = {\sim}95$ mm. These results would seem to contradict the idea that rebars may cause reduction of coupling between antennas since the material of rebars is steel. The results show that when the g is less than one and half wavelength, the antenna coupling dramatically reduces since an upper rebar layer drastically shields the electromagnetic waves. In summary, in order to provide an efficient wireless power transfer in a reinforced concrete slab, the electrical dimensions of rebar cells must be taken into account.
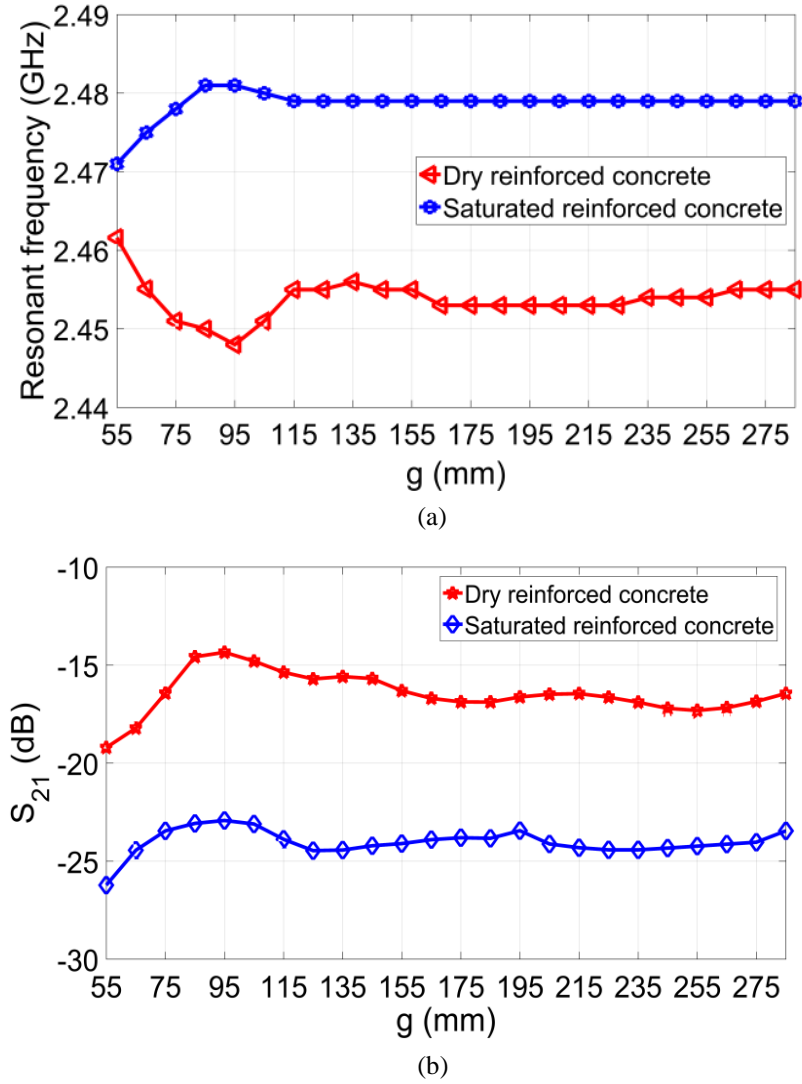
Figure 4.16 (a) Resonant frequency of the embedded patch antenna and (b) the magnitude of transmission coefficient (coupling between the antennas) versus mesh period g at dry and saturated reinforced concrete ($L_1 = \lambda = 122.45$ mm, $L_2 = 107$ mm, λ is wavelength in free space).

The electric field distributions in the RAVA, the concrete slab and reinforced concrete slab with the embedded patch antenna at three values of the mesh period at 2.45 GHz are shown in Figs. 4.17 and 4.18. As can be seen from Fig. 4.17(a) that the RAVA radiates EM waves toward the concrete slab and EM waves partly reflect from a concrete-to-free space interface and partly transmit inside and through the concrete slab. Figs. 4.17(b-d) demonstrate that the presence of the rebars in the concrete slab significantly changes the electric field distribution in the slab, in particular when the

value of mesh period is equal to 95 mm as shown in Fig. 4.17(b). These changes decrease as the value of mesh period increase, as shown in Fig. 4.17(b-d). In addition, the comparison of the electrical field distributions at the three values of mesh periods clearly indicates that the highest electric field intensity near the location of the embedded patch antenna is at g = 95 mm (c.f. Fig. 4.17(b)).

Fig. 4.18 shows electrical field intensity distributions, when the patch antenna embedded in the slabs is a transmitting antenna. It can be clearly seen from Fig. 4.18 that the embedded antenna radiates EM waves, which propagate through the part of the slabs and penetrate into free space. Compared the case of concrete slab (c.f. Fig. 4.18(a)) electrical field intensity in the case of reinforced concrete slab is higher in the RAVA and free space, in particular at location K as designated in Figs. 4.18(b)-(d)). The highest intensity in these placed is observed at g = 95 mm. We can conclude that there is a similarity between this observation and the results for the resonant frequency of patch antenna, the coupling between antennas and electrical field intensity distributions shown in Fig. 4.16(a), Fig. 4.16(b) and 4.17, respectively.
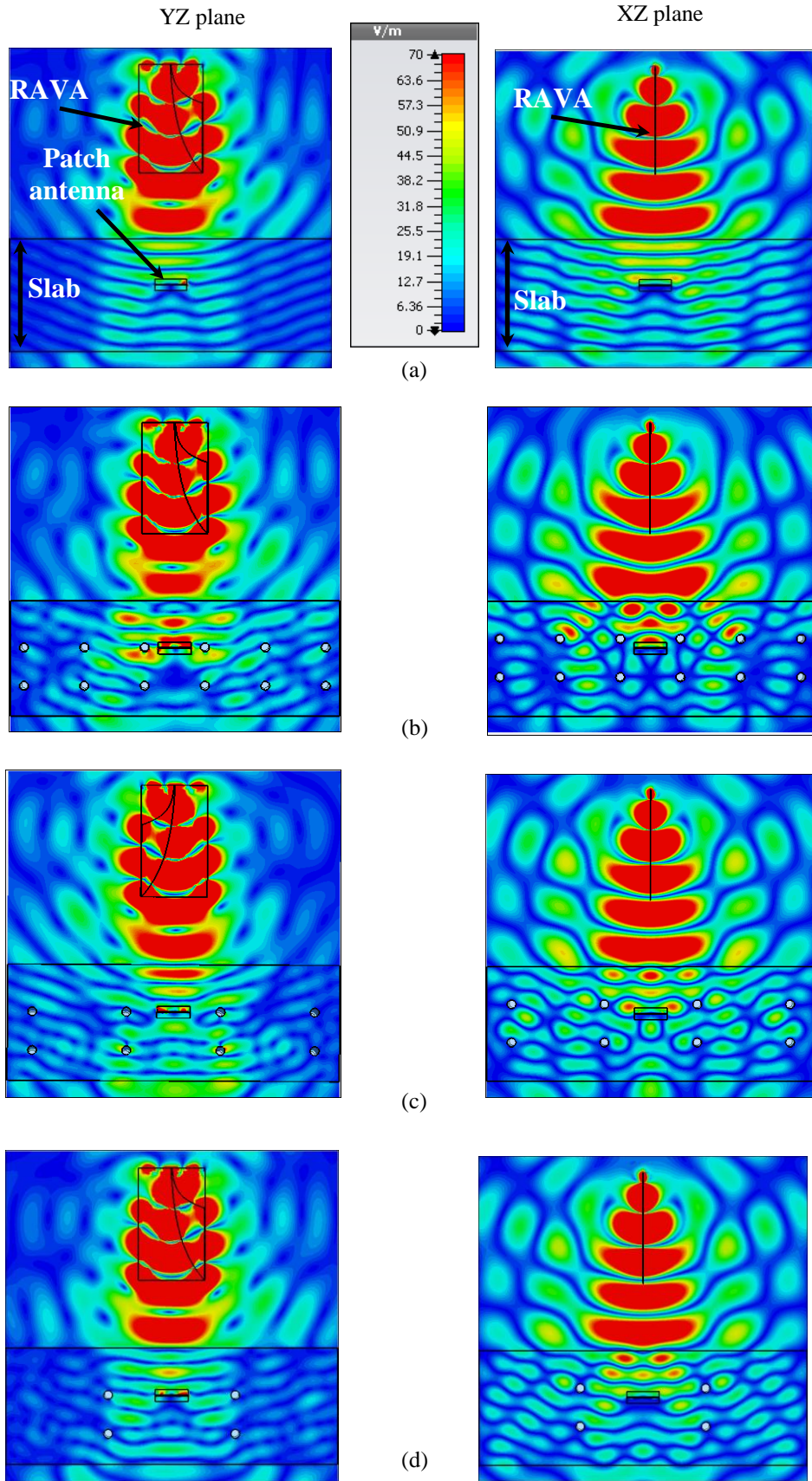
Figure 4.17 Electrical field intensity distribution in the two-antenna setup and (a) the dry concrete slab, and dry reinforced concrete slab with: (b) *g* = 95 mm, (c) *g* = 115 mm, and (d) *g* = 255 mm, when the *RAVA is transmitting antenna*.
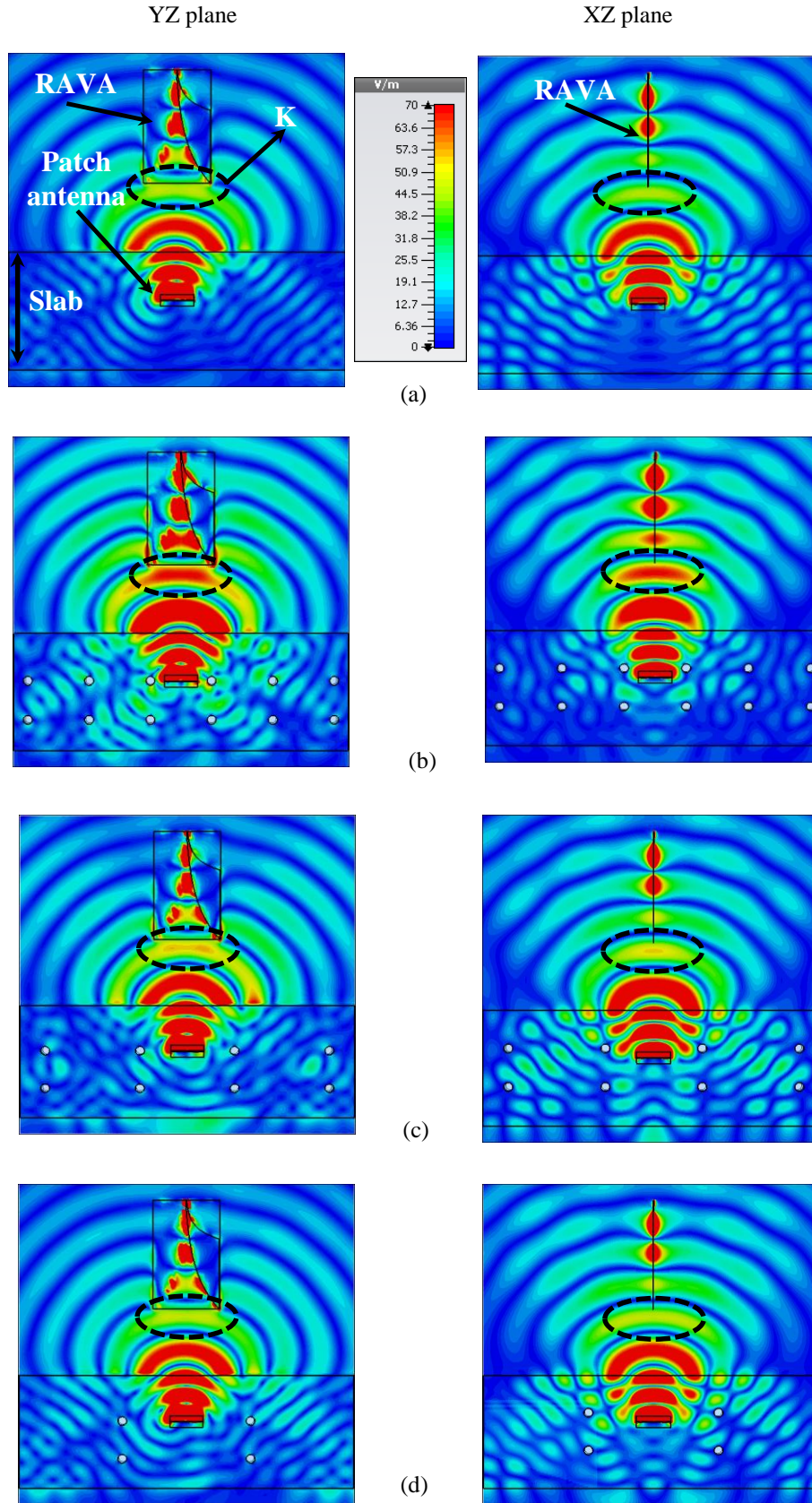
Figure 4.18 Electrical field intensity distribution in the two-antenna setup and (a) the dry concrete slab, and dry reinforced concrete slab with: (b) *g* = 95 mm, (c) *g* = 115 mm, and (d) *g* = 255 mm, when the *patch antenna is transmitting antenna.*

4.3.1.2 Parametric study on L_2

The investigation into the influence of locations of the patch antenna in the concrete and reinforced concrete slabs on the resonant frequency of the antenna and coupling between antennas for dry and saturated concrete was also performed. The results at different L_2 at the range from 10 mm − 190 mm for the dry and saturated concrete are shown in Fig. 4.19. It can be seen from Fig. 4.19(a) that the increase of L_2 causes a periodical change of the resonant frequency near 2.45 GHz and 2.48 GHz for the dry and saturated concrete slabs, respectively. This change monotonically decreases when L_2 increases. Fig. 4.19(b) shows the highest value of the magnitude of transmission coefficient (i.e. level of coupling) between the antennas versus L_2 in concrete and reinforced concrete slabs. Several observations can be made from Fig. 4.19(b). As expected, the coupling is higher in the *dry concrete than in the saturated concrete* for both the concrete and reinforced concrete slabs and coupling decreases with increasing L_2 faster in saturated concrete slabs than in dry concrete slabs. Interestingly, coupling between antennas are higher in *dry (saturated) reinforced concrete than in the dry (saturated) concrete.* This observation confirms that the rebars cause increasing the coupling between antennas. It should be noted that maximum coupling (-13.5 dB) are achieved to *dry reinforced concrete slab* at the range of L_2 from ~70 mm to ~110 mm. Therefore, this range of L_2 can be considered as optimal for effective power transfer at the given two-antenna setup and reinforced concrete slab.
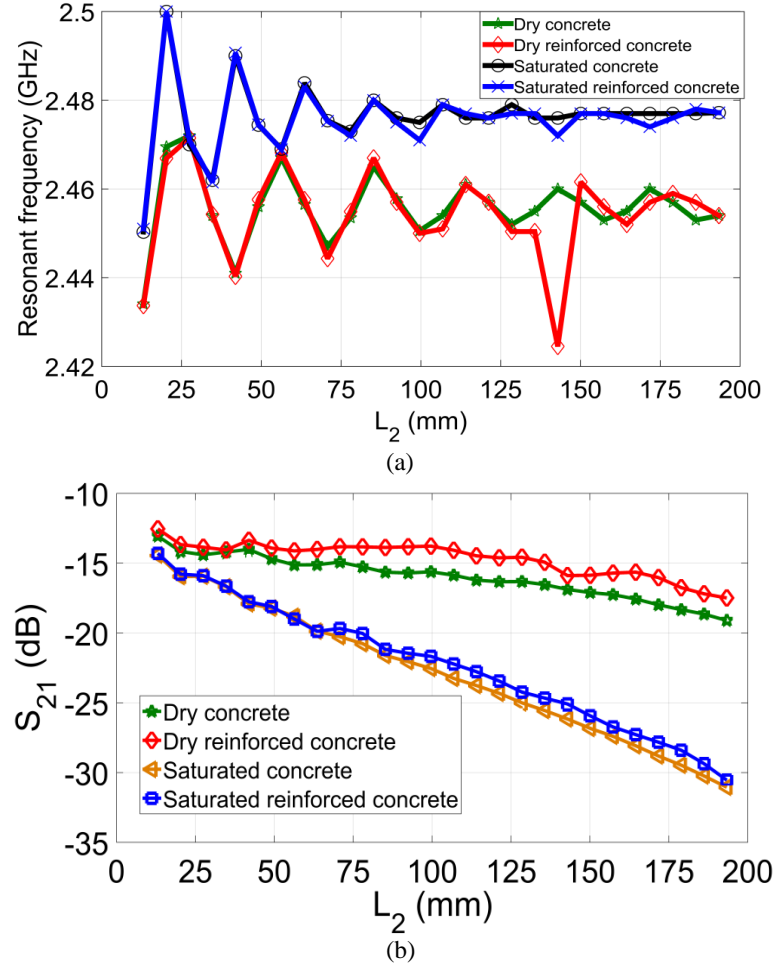
Figure 4.19 (a) Resonant frequency of the embedded patch antenna and (b) the magnitude of transmission coefficient (coupling between the antennas) versus L_2 (g =110 mm, L_1 = 122.45 mm = λ).

4.3.1.3 Parametric study on L_1

Fig. 4.20(a) shows the resonant frequency of RAVA versus the distance between this antenna and the surface of concrete, L_1, which changes from 0 mm to 245 mm (i.e., from 0 – 2λ. As an overall trend, the sharp fluctuations of the resonant frequency at small distances between the specimen and the antenna can be attributed to distortion of electric field distribution of the antenna by the specimen and the amplitude of fluctuations decreases when L_1 changes from 25 mm -125 mm *(~λ)*. The amplitude of fluctuations of the resonant frequency is higher when the concrete is saturated in

92

comparison with dry concrete because the saturated concrete has higher dielectric constant than the dry concrete.
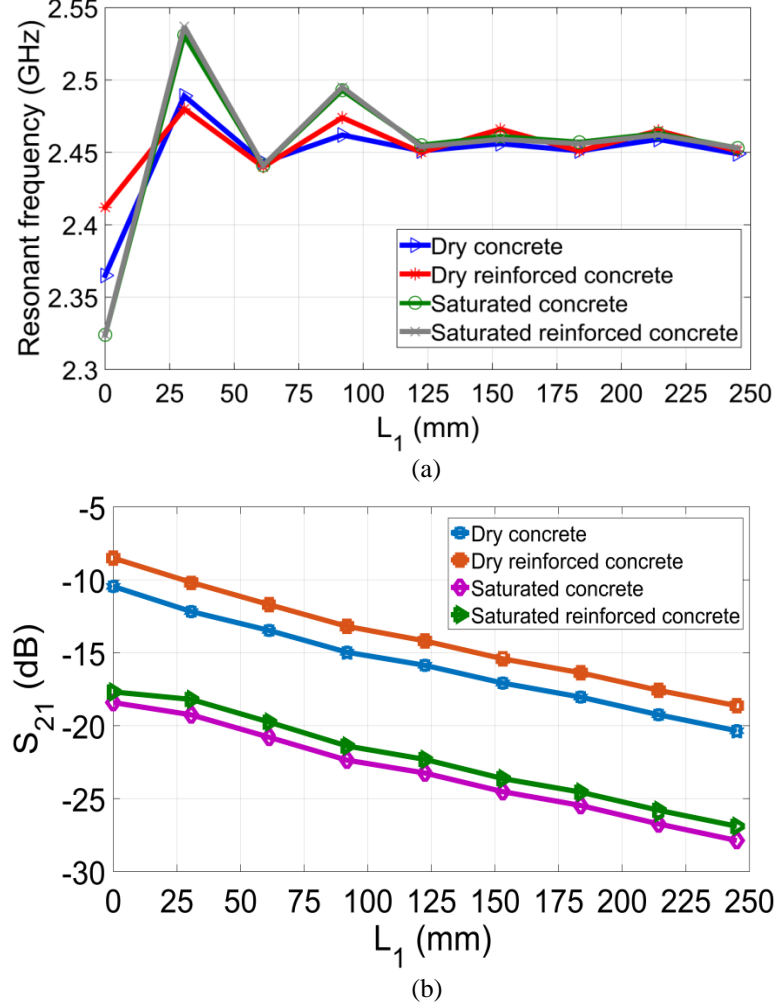
Figure 4.20 (a) Resonant frequency of the embedded patch antenna and (b) the magnitude of transmission coefficient (coupling between the antennas) versus L_1 (g =110 mm, L_2 = 107 mm).

Fig. 4.20(b) shows the magnitude of transmission coefficient versus L_1. This figure demonstrates that the coupling between the antennas monotonically decreases with the increase of L_1 in all four cases of concrete slabs, and it is higher for the dry concrete than in the saturated concrete. The highest coupling is achieved in the dry reinforced concrete. It should be noted that the decrease of coupling is almost -5 dB/λ for all cases which can be attributed to free space loss.

It is well known that both antennas have to be aligned properly to provide maximum coupling. It may happen that the embedded patch antenna is shifted from its correct position (i.e., the position aligned with the RAVA). Therefore, the reflection coefficient of the RAVA and coupling between the antennas at three locations of the two-antenna setup with respect to the rebars along X-axis, u_1, (c.f. Fig. 4.12(c)) have been investigated and the results are shown in Fig. 4.21. It can be seen from Fig. 4.21 that coupling between antennas reduced when u_1 increases and the maximum (minimum) coupling are achieved at $u_1 = 0$ (40 mm) when the embedded patch antenna is in the centre of rebar cell (the closest to one of the rebars). It is observed that the resonant frequency of the RAVA increase when u_1 increases.
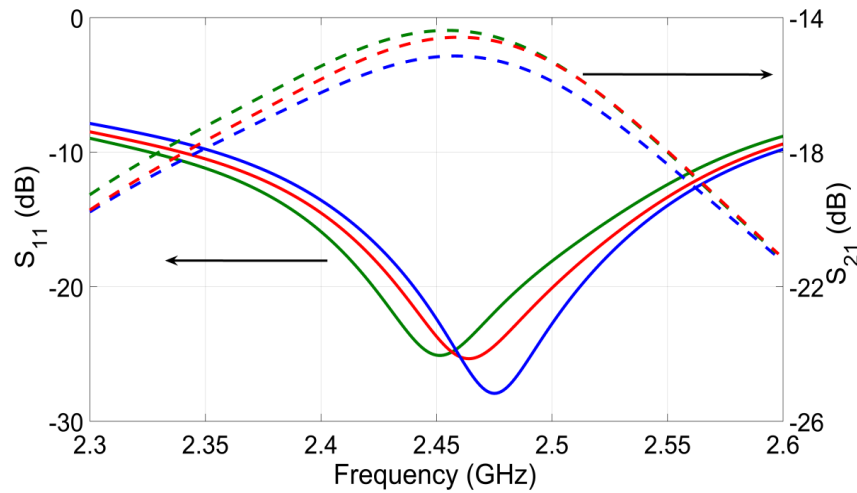
Figure 4.21 Magnitude of the reflection coefficient of the RAVA (S_{11}) and coupling between the antennas (S_{21}) versus frequency at three locations of the two-antenna set up along X-axis (u_1) in the dry reinforced concrete slab at g =110 mm, L_1 = 110 mm and L_2 = 107 mm.

4.3.2 Reinforced concrete column

A reinforced concrete column is a structural member designed to carry compressive loads. It consists of concrete column with an embedded steel frame to provide reinforcement. Reinforced concrete columns are categorised into five main types; a

rectangular tied column, rectangular spiral column, round tied column, round spiral column, and columns of other geometry (Hexagonal, L-shaped, T-Shaped, etc.) (Choi 2002). Fig. 4.22 shows the rectangular tied and round spiral concrete columns. Tied columns have horizontal ties to enclose and hold in place longitudinal bars. Ties are commonly No. 3 or No.4 steel bars. Spiral columns have reinforced longitudinal bars that are enclosed by continuous steel spiral. The spiral is made up of either large diameter steel wire or steel rod and formed in the shape of helix. The spiral columns are slightly stronger than tied columns (Choi 2002).

(a)   (b)
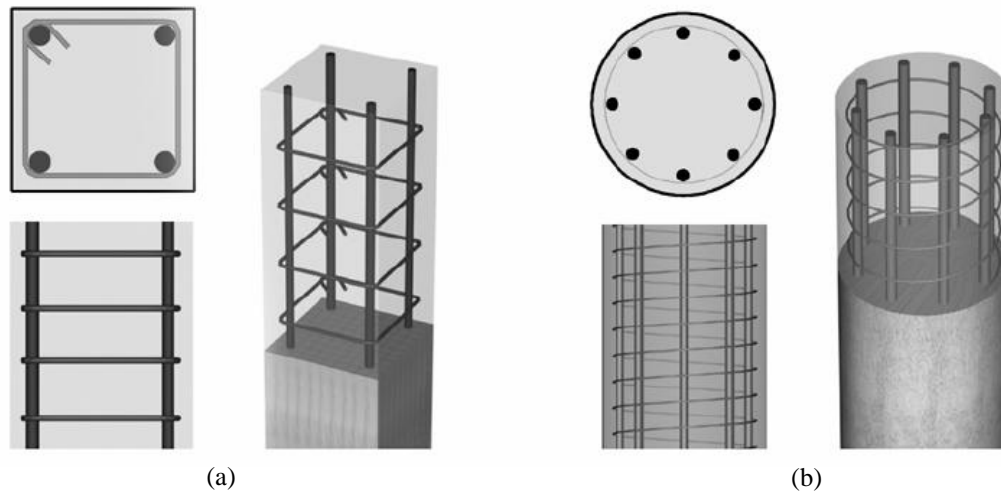
Figure 4.22 Column types (a) rectangular tied column and (b) round spiral column.

In practice, reinforced concrete column are constructed at different configuration with different values of steel ratio. In this section, a reinforced concrete column section with steel ratios of 1%, 2%, 3% and 4% has been studied. Diameter of column and rebars are 300 mm and 14 mm, respectively. Moreover, the distance between rebars and concrete column surface, L_c, and distance between rebars, l, should be more than 50 mm and twice the diameter of the rebar. Steel ratio and number of rebars in the column are calculated by using the following equations:

$$Steel\ ratio = \frac{A_s}{A} \tag{4.4}$$

$$Number\ of\ rebars = \frac{A_s}{A_b} \tag{4.5}$$

where A_S and A are total rebars area in column and cross section of the column, respectively, and A_b is area of one rebar.

A model of the setup including the cylindrical concrete column with different steel ratios and the RAVA as a transmitting antenna and the patch antenna as a receiving antenna located at distance L_1 and L_2 from the interface between free space and concrete surface, respectively, is created in CST MWS as shown in Fig. 4.23.

(a)

(b)
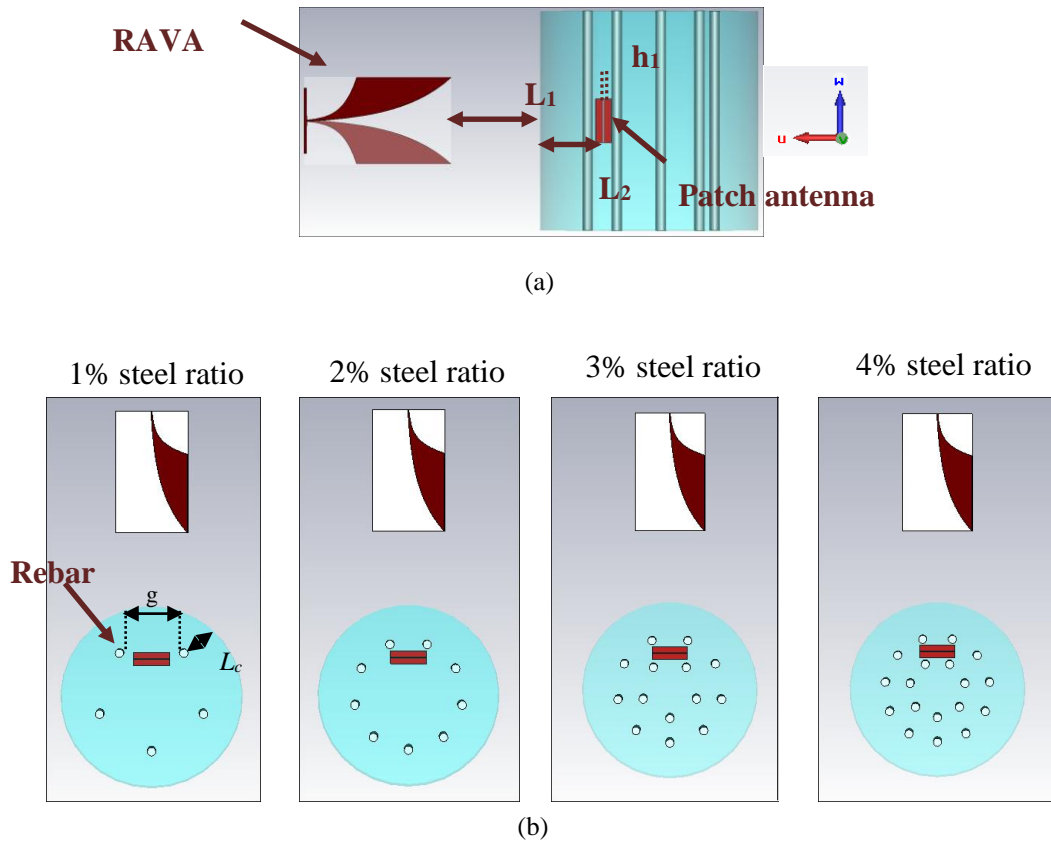
Figure 4.23 Model of the antennas and reinforced concrete column with different values of steel ratio in CST: (a) cross-sectional side view of the model with 1% steel ratio, and (b) cross-sectional front view of the model with 1%, 2%, 3% and 4% ($L_1 = 122.45$ mm $= \lambda$, $L_2 = 85$ mm, $d = 16$ mm and λ is free-space wavelength).

Since material of rebars is metal, they may effect on the performance of transmitting and receiving antennas as well as WPT between the antennas. It is worth to mention that the polarisation of these antennas should be aligned properly in order to maximise coupling between antennas. With respect to rebars embedded inside column, the transmitting and receiving antennas polarisation can be aligned parallel or vertical to rebars. Therefore, the influences of reinforced concrete column with different steel ratios on reflection and coupling between antennas are investigated while electric field polarisations of these antennas are parallel or vertical to longitudinal rebars (referred to as parallel or vertical configuration, respectively).

4.3.2.1 Reflection properties of reinforced concrete columns with different values of steel ratio

Reflection properties of dry and saturated reinforced concrete columns with four values of steel ratio are studied here. Fig. 4.24 shows the resonant response of the RAVA in concrete and reinforced concrete columns at $L_1 = 122.5$ mm (i.e., λ) and at two polarsation configurations. It can be clearly seen in Fig. 4.24 that increasing the steel ratio of the concrete column marginally affects the resonant frequency of the RAVA. However, changes of magnitude of the reflection coefficient at the resonant frequency can be observed in particular, at parallel configuration at 1% steel ratio. There are several factors that may contribute separately or in combination to this behaviour of the magnitude including the reflection of EM waves from free space-to-concrete front and back interfaces, and from the rebars, as well as attenuation of EM waves in concrete.
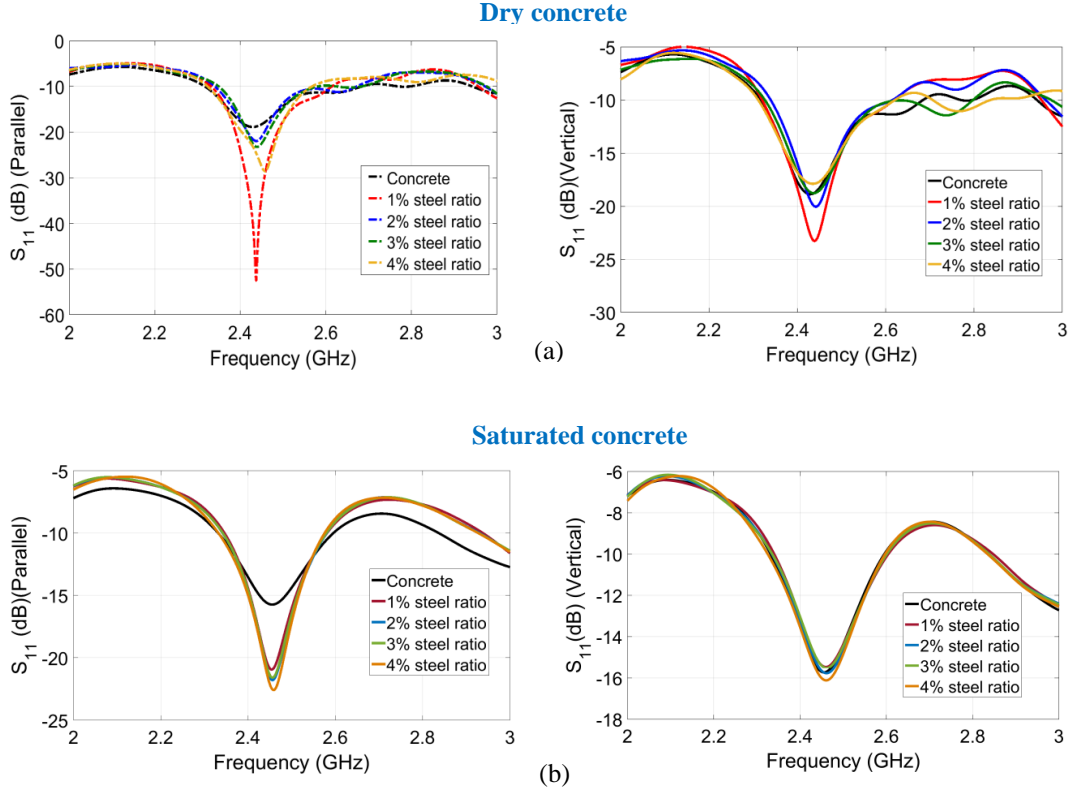
Figure 4.24 S_{11} of the RAVA versus frequency at parallel (left) and vertical (right) configurations in the (a) dry and (b) saturated reinforced concrete columns with different values of the steel ratio at L_1 = 122.5 mm and L_2 = 85 mm.

Since the location of the patch antenna may be restricted by rebars when the value of the steel ratio increases, the resonant response of embedded patch antenna was investigated at three values of L_2 as shown in Fig. 4.25 for the reinforced concrete column with the highest steel ratio (i.e., 4%). Fig. 4.26 and Fig. 4.27 show the magnitude of reflection coefficient of the antenna for different values of the steel ratio in dry and saturated reinforced concrete columns, respectively.
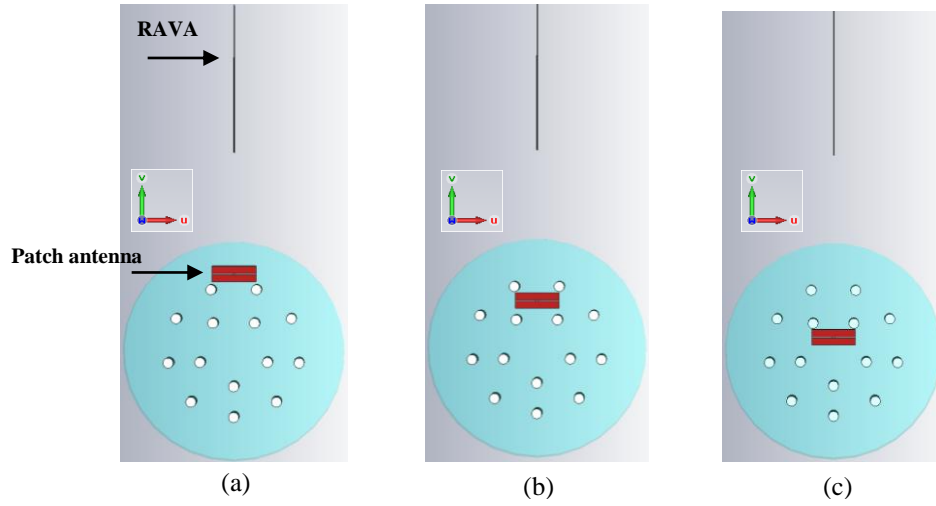
Figure 4.25 Cross-sectional top view of the two-antenna setup at three locations of the patch antenna inside reinforced concrete column (steel ratio is 4%): (a) $L_2 = 45$ mm, (b) $L_2 = 85$ mm, and (c) $L_2 = 130$ mm (parallel configuration).

It can be seen from Fig. 4.26 that when the configuration of antennas are parallel and vertical, the resonant frequency of the patch antenna slightly shifted to the lower and higher frequencies, respectively, when the value of steel ratio increase. In particular, this effect is dominant at relatively high steel ratio (3% and 4%). The maximum change of the resonant frequency and magnitude of the reflection coefficient is observed at $L_2 = 85$ mm and $L_2 = 130$ mm, respectively, at 4% steel ratio and at the parallel configuration of antennas as shown in Figs. 4.26(b-c).
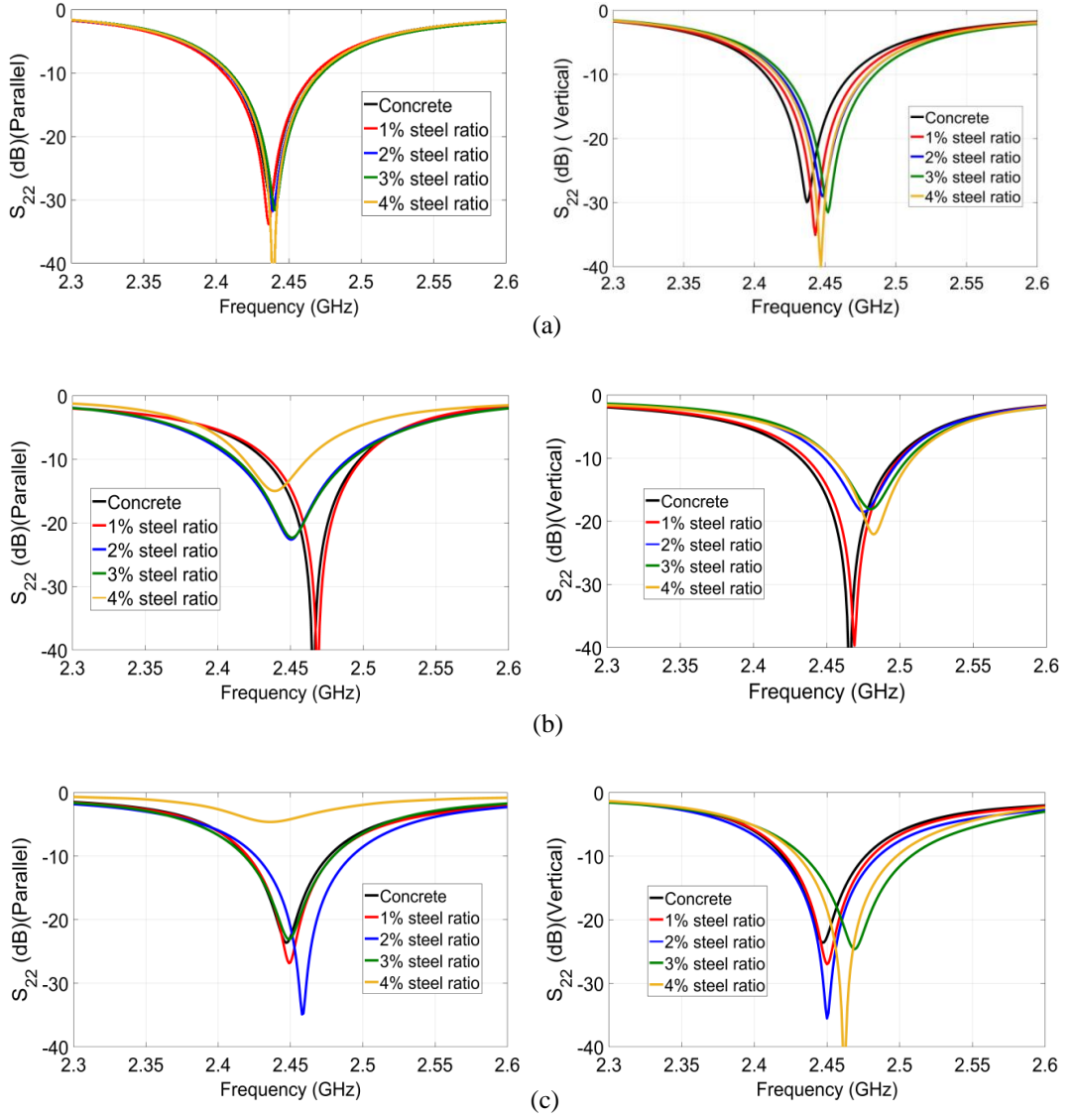
Figure 4.26 S_{22} of the patch antenna embedded inside *dry concrete column* at parallel (left) and vertical (right) configuration at (a) $L_2 = 45$ mm, (b) $L_2 = 85$ mm, and (c) $L_2 = 130$ mm.

Similar effects of steel ratio, L_2, parallel and vertical configurations on the resonant response of the patch antenna can be observed in the saturated reinforced concrete but they are weaker than in the dry concrete as shown in Fig. 4.27. This can be attributed to the dominant influence of losses in saturated concrete due to its relatively high moisture content.
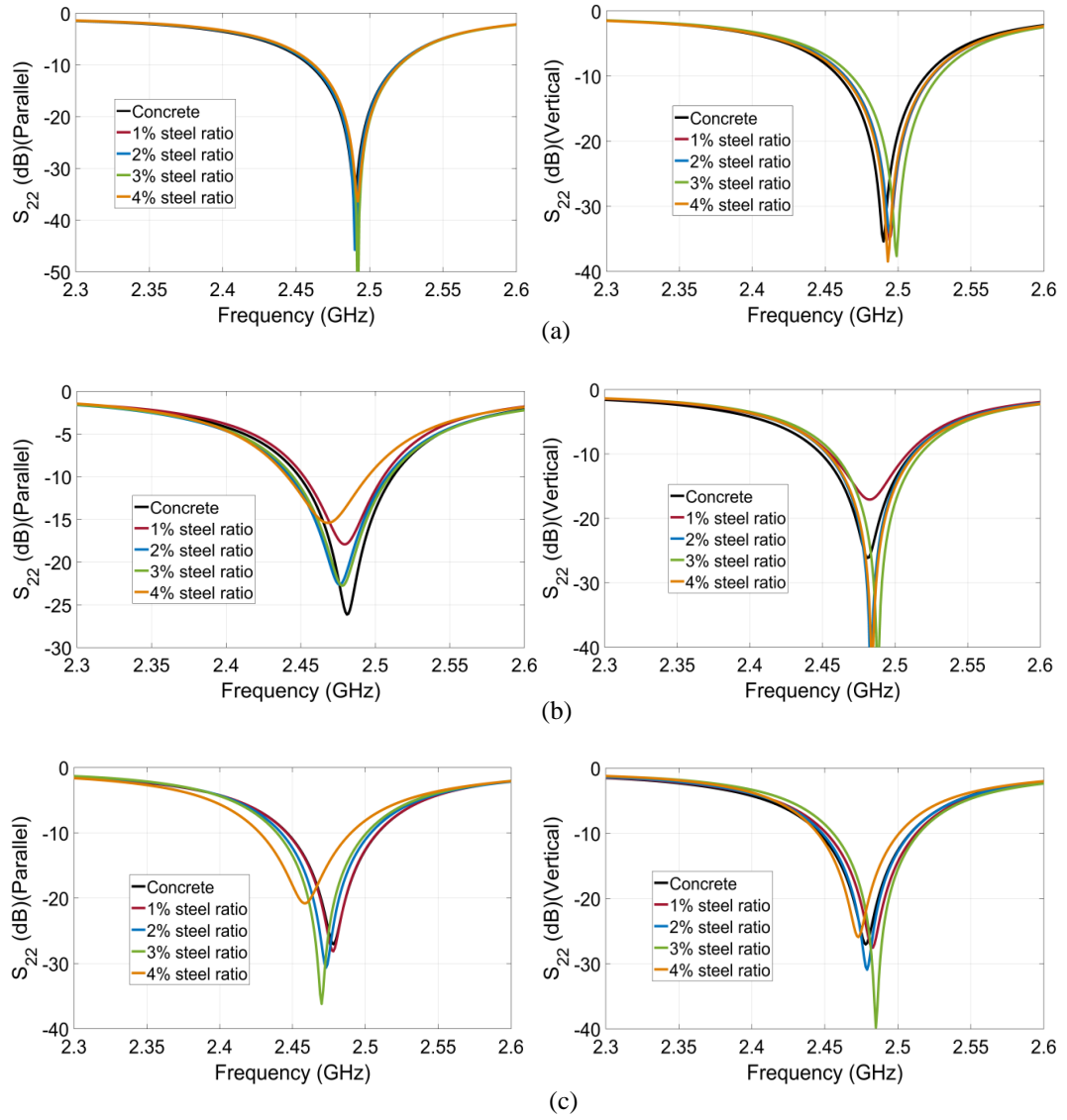
Figure 4.27 S_{22} of the patch antenna inside *saturated concrete column* at parallel (left) and vertical (right) configuration at (a) $L_2 = 45$ mm, (b) $L_2 = 85$ mm, and (c) $L_2 = 130$ mm.

4.3.2.2 Coupling between the antennas with dry and saturated concrete columns

Figs. 4.28 and 4.29 show magnitude of the transmission coefficient between the antennas versus frequency when the patch antenna embedded in (a) *dry* and (b) *saturated reinforced concrete columns* with different values of steel ratio and two polarsation configurations and at three values of L_2. It can be seen from these figures that the coupling between the antennas at the resonant frequency decreases when L_2 increases for all cases or while value of steel ratio increases at $L_2 = 85$ mm and 130

mm. Changing of the steel ratio negligibly changes the coupling when the patch antenna locates at $L_2 = 45$ mm (c.f. Figs. 4.28(a) and Figs. 4.29(a)) whilst the most significant changes are observed at parallel configuration. These changes are clearer and the resonant responses are smoother for the saturated concrete columns than for the dry concrete ones.

Parallel configuration   **Vertical configuration**

(a)

(b)

(c)
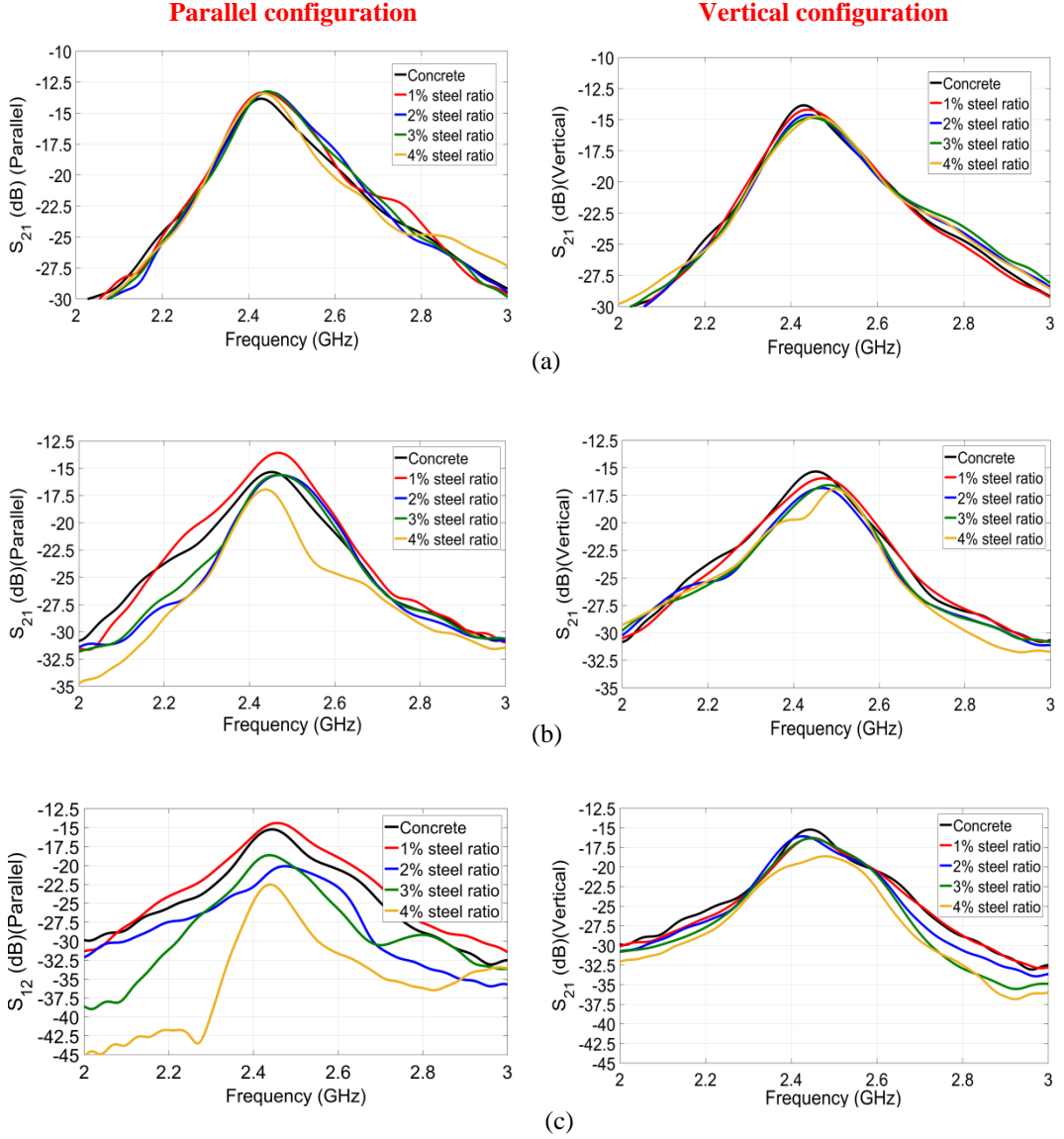
Figure 4.28 Magnitude of the transmission coefficient between the antennas when the patch antenna embedded in the *dry reinforced concrete columns* with different values of steel ratio and two configurations at (a) $L_2 = 45$ mm, (b) $L_2 = 85$ mm, and (c) $L_2 = 130$ mm.

(a)

(b)

(c)
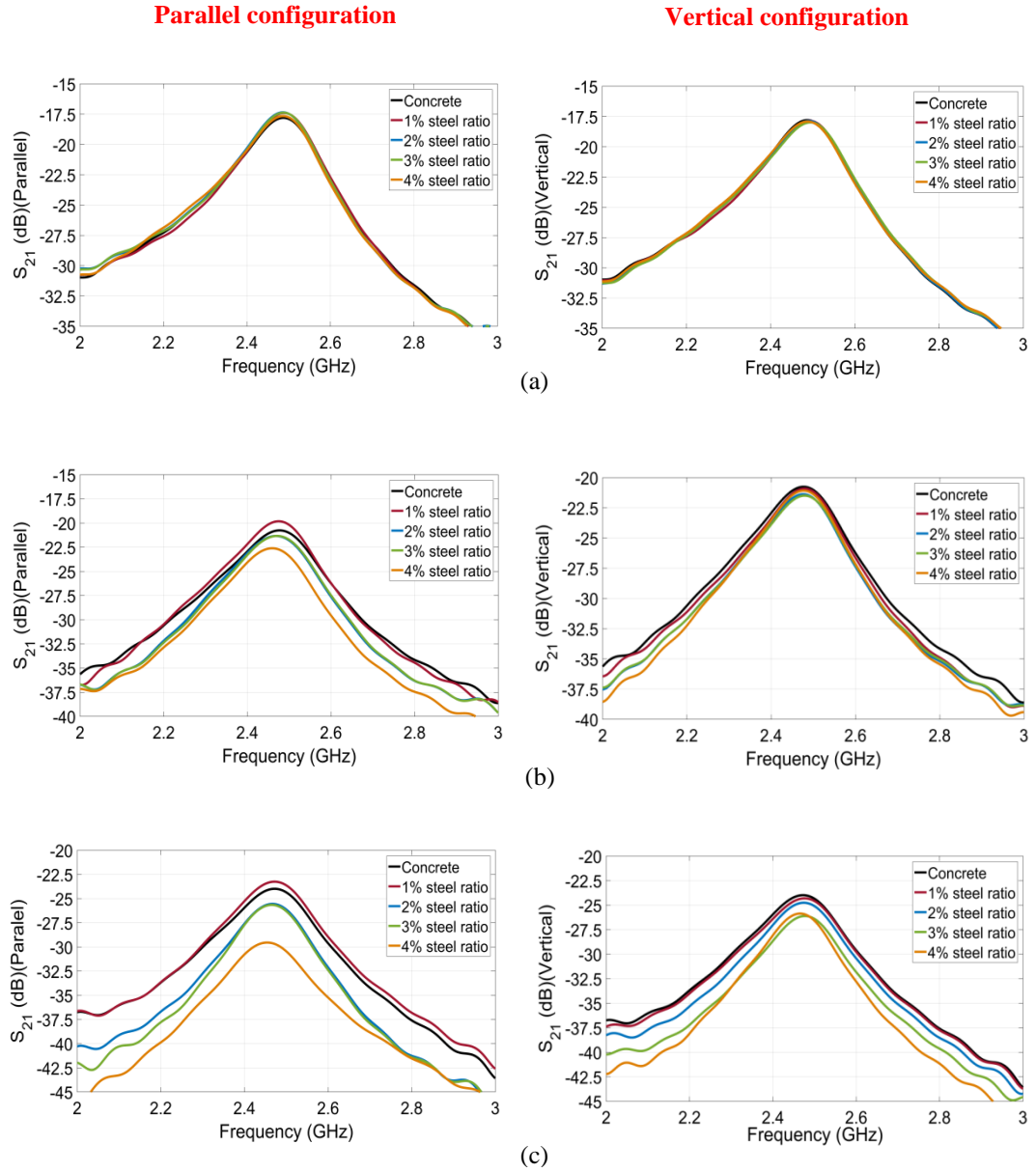
Figure 4.29 Magnitude of the transmission coefficient between the antennas when the patch antenna embedded in the *saturated reinforced concrete columns* with different values of steel ratio and two configurations at (a) $L_2 = 45$ mm, (b) $L_2 = 85$ mm, and (c) $L_2 = 130$ mm.

4.3.2.3 Electrical field distribution

Figs. 4.30 and 4.31 show electric field intensity distribution when the antennas are aligned at parallel and vertical configurations for *the dry and saturated* reinforced concrete columns, respectively, at 1% steel ratio and $L_2 = 85$ mm. It can be clearly

seen from these figures that electric field intensity in the embedded patch antenna is higher at parallel than at vertical configuration at both columns demonstrating enhancement of the coupling between antennas as was shown previously. In the case of dry concrete column EM waves propagate through the column and reflect from free space-to-concrete interfaces. Comparison between Fig. 4.30 and Fig. 4.31 illustrates different level of EM attenuation in the dry and saturated concrete columns; the attenuation of EM waves in saturated concrete is higher than in dry concrete, as expected. Overall, these results confirm our observations and interpretations of the results related to reflection and transmission properties of the considered columns.
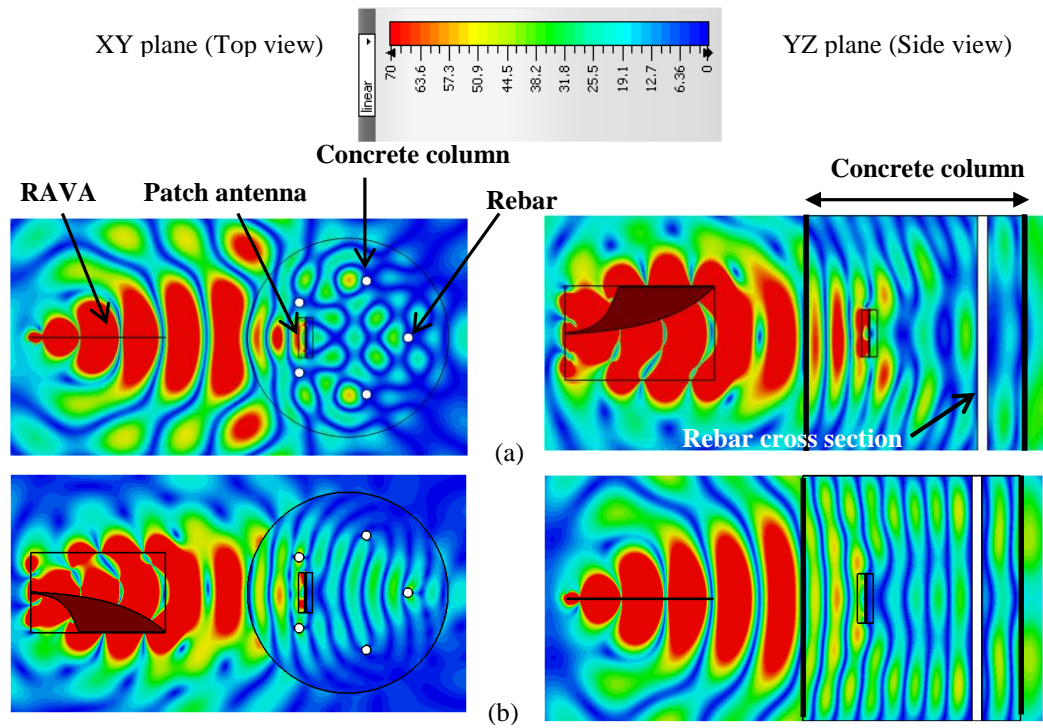
Figure 4.30 Cross-sectional top (left) and side (right) views of electrical field intensity distribution in the *dry reinforced concrete column* with 1% steel ratio at $L_1 = 85$ mm, while the antennas are aligned at: (a) parallel and (b) vertical configuration.
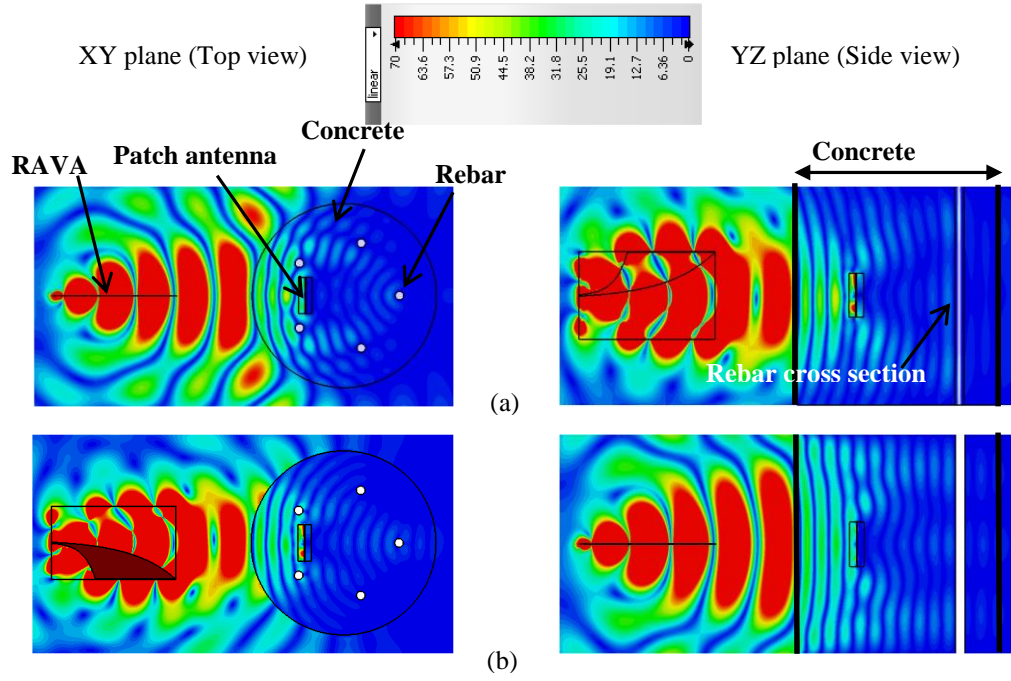
Figure 4.31 Cross-sectional top (left) and side (right) views of electrical field intensity distribution in *the saturated reinforced concrete column* with 1% steel ratio at $L_1 = 85$ mm, while the antennas are aligned at: (a) parallel and (b) vertical configuration.

4.4 Summary

A relatively small and high-gain resonant antipodal Vivaldi antenna as a transmitting antenna and a modified embeddable microstrip patch antenna as a receiving antenna were designed to operate in a two-antenna setup at 2.45 GHz for WPT in concrete members. These members included reinforced dry and saturated concrete slabs and columns with different values of mesh period of rebars and steel ratio, respectively. It was shown that there was a critical value of mesh period of rebars (i.e., 95 mm) with respect to reflection and transmission properties of the slabs which is related to wavelength in concrete. The maximum coupling between antennas was achieved at this value. The coupling between the antennas in the saturated concrete is always lower and reduces faster than in the dry concrete when the distance between the embedded patch antenna and the surface of concrete increases due to the increase of loss in

concrete. On the other, the coupling between the antennas with the saturated concrete is always lower than with the dry concrete when the distance between the RAVA and the surface of concrete increases due to the increase of free space loss. In this investigation, the two-antenna setup was aligned with the center of the rebar cell and it was shown that the coupling decreased when it shifted towards one of the rebar.

The investigation into reinforced concrete columns showed that polarsation configuration of the two-antenna setup with respect to rebars and steel ratios as well as losses in concrete are important parameters. It was observed that the coupling between antennas reduced faster by increasing the value of steel ratio at parallel than in vertical configuration due to the increase of the interaction between EM waves and rebars. This effect is more prominent in the saturated than in dry reinforced concrete columns.

Chapter 5 Design of Rectenna and RAVA Array for Recharging Batteries of Sensors Embedded inside Reinforced Concrete

5.1 Introduction

One of the undertaking methods for IHM is using wireless embedded sensors which can be buried in concrete during the construction to collect and report valuable monitoring data. Several publications have considered recharging batteries of sensors embedded inside *concrete members*. However, limited works have been performed to recharge the batteries of sensors embedded inside *reinforced concrete members* as mentioned in chapter 2. The main purpose of this section is to develop a WPT system for recharging batteries of wireless sensors embedded inside reinforced concrete slab and reinforced concrete column with different configurations and moisture content.

Firstly, an embeddable rectenna is designed. It consists of the microstrip patch antenna developed in previous chapter and a rectifying circuit, and can be embedded inside the reinforced concrete slab and reinforced concrete column. A single RAVA is used as a transmitting antenna and the main challenge of this part of research is to provide desired output voltage of the rectenna while the microstrip patch antenna is a receiving antenna.

Secondly, a 4-element RAVA array with a Wilkinson power divider feeding network is developed in this part. The main motivation of this research and development is a demand of higher directivity and efficiency of a transmitting antenna since a single RAVA provides low values of directivity (gain) which do not allow increasing distances between antennas and concrete surface.

5.2 Rectenna design

Rectenna is a key component of WPT system for recharging batteries of the embedded sensors. It receives microwave energy and converts it into DC voltage for the load. The impedance matching network is required to enable the rectifier to work at typical 50 Ω RF platforms. The simpler rectification circuit designs are necessary for IHM sensors. Therefore different types of rectifying circuits such as series-diode half wave rectifier (Heljo et al. 2013), full wave bridge rectifier (Itoh, Kenji 2015), and full wave voltage doubler (Jiang & Georgakopoulos 2011) will be considered to select the most applicable one. Then, the rectenna with selected rectified circuit will be applied with a single RAVA and with a RAVA array to recharge the batteries.

5.2.1 Series-diode half-wave rectifier

The simplest and best known rectifier circuit is a half wave rectifier. It can be designed by using a diode and a load as shown in Fig. 5.1 (Dobkin 2008; Feucht 2014).
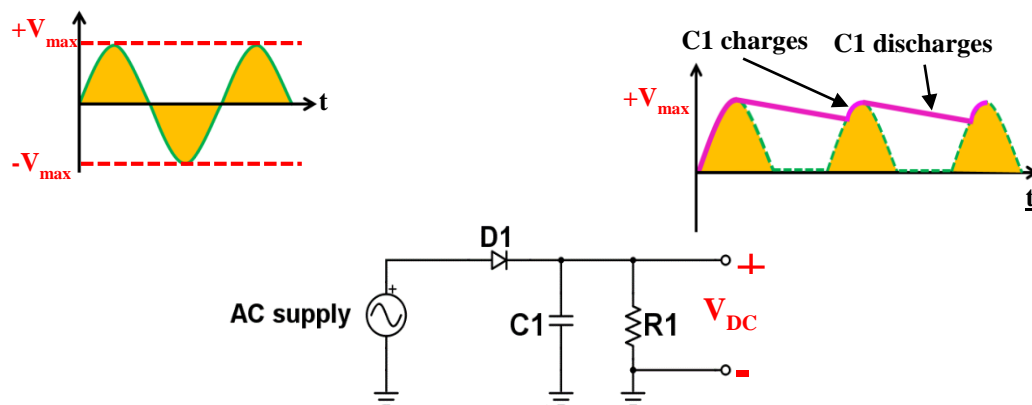
Figure 5.1 Half-wave rectifier circuit (Dobkin 2008; Feucht 2014).

In order to produce a steady DC voltage from a rectified AC source, a filter or smoothing circuit is needed. In the simplest form this can be just a capacitor placed across the DC output of the rectifier. 5.2.2 Full-wave bridge rectifier

5.2.2 Full-wave bridge rectifier

A full-wave bridge rectifier is a circuit arrangement which converts both half cycles of input waveform (AC) to direct current (DC). Circuit diagram of full wave bridge rectifier circuit is composed of four diodes which arranged in the form of a bridge as shown in Fig. 5.2. The bridge rectifier circuit is nearly general in modern power supplies, but it has two disadvantages in signal detection applications; one being that it has two diode forward-voltages in the path to the load, and the other being that either the output or the input terminals must be allowed to float with respect to the system ground.
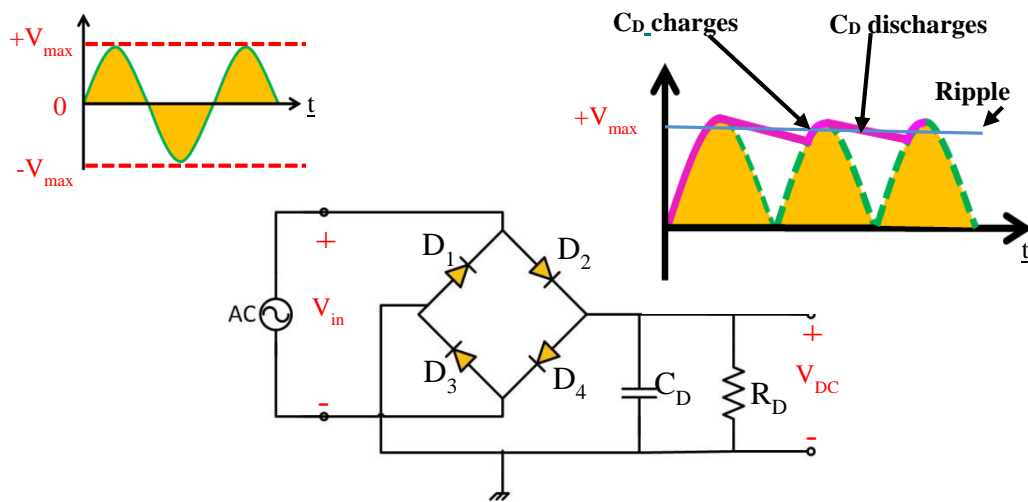
Figure 5.2 Full wave bridge rectifier circuit (Feucht 2014; Savant 1987).

One advantage of the bridge rectifier is that the maximum inverse voltage for any of the diodes is only $\sqrt{2}$ times the RMS input voltage. The magnitude of the inverse

voltage across *D*2 is prevented from rising above $V_{in}\sqrt{2}$ by the clamping action of *D*1 and vice versa. The same argument applies for *D*3 and *D*4 (Knight 1st Jan. 2016.).

5.2.3 Full-wave voltage doubler

The schematic in Fig. 5.3 represents one stage of voltage doubler rectifier circuit. This circuit is called a voltage doubler because in theory, the voltage that is received on the output is twice that at the input. The RF wave is rectified by *D*2 and C_D in the positive half of the cycle, and then by *D*1 and C_C in the negative cycle. But, during the positive half-cycle, the voltage stored on C_C from the negative half-cycle is transferred to C_D. Thus, the voltage on C_D is roughly two times the peak voltage of the RF source minus the turn-on voltage of the diode, hence named voltage doubler (Harrist 2004). Note that since the diodes operate alternately, this detector conducts on both positive and negative half-cycles of V_{in}, which means that it is actually a type of full-wave rectifier.
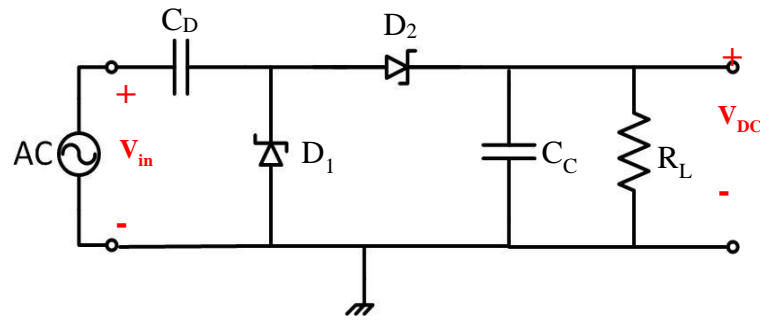
Figure 5.3 Full wave voltage doubler circuit (Feucht 2014).

Diodes are the main elements of a rectification circuit. Schottky barrier diode is used in most of microwave rectifiers because of its low forward voltage (e.g. V_f~0.3V) and high frequency switching capability. HSMS-286x series Schottky diode is used in designing our rectifier circuit since it meets the requirements of the sensor charging system. The modelling parameters for HSMS-286x diodes are given by Agilent data sheets, and the SPICE parameters are shown in Table 5.1. SPICE parameters can be

applied in CST DS for simulation modelling since both of them perform simulation using Netlists (Harrist 2004). In Table 5.1, R_S is the series resistance and C_{J0} is the junction capacitance. R_S and C_{J0} have the most effect on the diode since these two factors determine the turn on voltage and rise time. Lower R_S leads to lower voltage needed to turn on the diode, and lower C_{J0} raises voltage faster. B_V is the reverse breakdown voltage and E_G represents the band-gap energy. I_{BV} and I_S are the current breakdown voltage and the saturation current, respectively. N is the emission coefficient, while M is the grading coefficient. These parameters are used in our simulation setups in CST.

Table 5.1 HSMS-286x SPICE parameters

Parameters	Unit	Value
B_V	V	7.0
C_{J0}	pF	0.18
E_G	eV	0.69
I_{BV}	A	1 E-5
I_S	A	5 E-8
N	no units	1.08
R_S	Ω	6.0
P_B	V	0.65
P_T	no units	2
M	no units	0.5

5.3 Recharging of wireless sensor's battery embedded inside reinforced concrete slab and reinforced concrete column using RAVA

In this section, wireless powering of embedded sensors is investigated; they are embedded inside 1) dry and saturated reinforced *concrete slab* (referred to as DRCS and SRCS, respectively) and 2) dry and saturated reinforced *concrete column* (referred

to as DRCC and SRCC, respectively). In order to recharge the battery, the two-antenna system including of the RAVA and the microstrip patch antenna operating at 2.45 GHz are designed at CST MW. The patch antenna is embedded at depth of $L_2 = 85$ mm inside dry and saturated reinforced concrete, while the RAVA as a transmitting antenna is placed at 123 mm above the air-to-concrete interface. Then the rectifier circuit is designed at CST Design studio (CST DS) which enables the co-simulation of circuit with 3D MWS.

The three previous mentioned rectifier circuits have been analytically analysed. The half wave and voltage doubler rectifier circuits are chosen to be used in this investigation due to simplicity and efficiency to the load, respectively, as shown in Fig. 5.4. To optimise the efficiency of the wireless powering system, matching circuits for the antennas and the rectifier circuit are designed. In CST DS, the transmitter antenna is connected to 1W power source with 50 Ω internal resistances. The optimise parameters of half-wave and voltage doubler rectification circuits are illustrated at Table 5.2 and Table 5.3, respectively. In order to match two antennas to 50 Ω, the capacitors $Cm1$, $Cm2$ and inductor $Lm1$ $Lm2$ are used. Also, inductor $Lm3$ and capacitor $Cm3$ are used due to matching the rectification circuit to 50 Ω.

Table 5.2 Half-wave rectifier circuit parameters.

Parameter	value	Parameter	value
Lm1	24nH	Cm2	5.8pF
Lm2	14nH	Cm3	0.47pF
Lm3	3.5nH	Cs	200pF
Cm1	9.8 pF	RL	120 Ω

Table 5.3 Voltage doubler rectifier circuit parameters.

Parameter	value	Parameter	value
Lm1	24nH	Cm2	5.8pF
Lm2	14nH	Cm3	0.47pF
Lm3	7nH	Cs	25pF
Cm1	9.8 pF	RL	1KΩ
Cs1	5pF		

The DC output voltage across the load at the half-wave rectifier circuit at dry reinforced concrete slab with different mesh periods are shown in Fig. 5.5. As illustrated by Fig. 5.5, there is a significant difference between DC output voltage of the half wave rectifier and the voltage doubler. As can be seen from Fig. 5.5, the DC output voltage decreased when the mesh period increase. As expected, the maximum voltage is achieved when the mesh period is 95 mm at DRCS.

To power an embedded sensor, we assumed to use an 100 mAH ML 2430 series Sanyo lithium coin cell battery which requires a charging voltage of 3.1 V and a charging current of 0.5 mA, respectively (Shams & Ali 2007). Such batteries are cheap and should be generally suitable for sensor applications. Sanyo manganese rechargeable lithium batteries are high-capacity rechargeable coin-type batteries. These batteries have a higher voltage (3 V) than Ni-Cd button cells (1.2V), with a low self-discharge rate and superior charge/discharge cycle characteristics. The DC voltage across the load at voltage doubler is sufficient to recharge such batteries as shown in Fig. 5.5 (b). It is worth to mention that the delivered DC voltages across the load by half wave rectifier is sufficient to recharge the 80 mAH Nickel-metal hydride button cell battery (Sodano et al. 2007). The power delivered to the load in the voltage doubler rectifier circuit and half wave rectifier for the DRCS with mesh period equal

to 95 mm is 45.4 mW and 33.1%, respectively, which is equivalent to a wireless power

transfer efficiency of 4.54% and 3.31%.
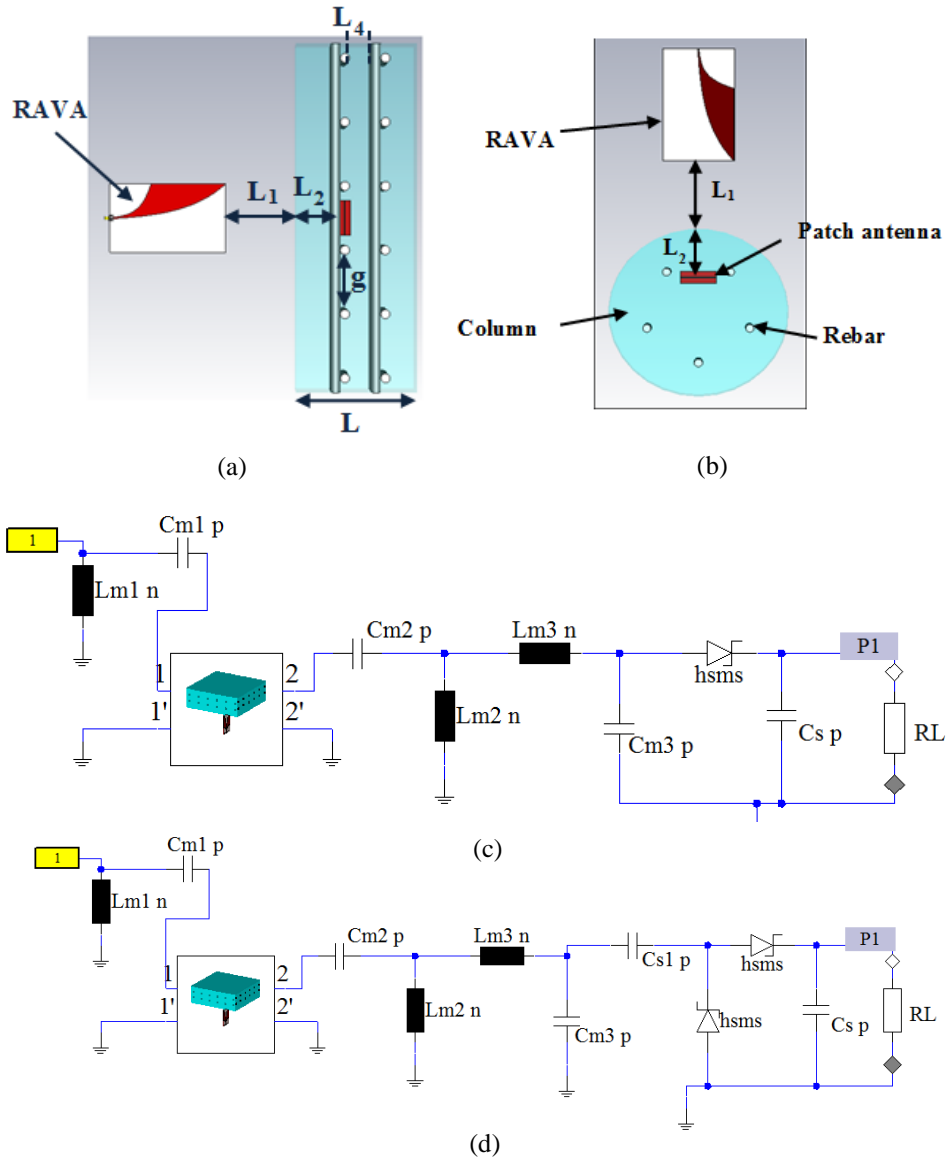
Figure 5.4 Model of the two-antenna setup and reinforced concrete (a) slab and (b) column, and schematic of the WPT system using (c) half wave rectifier, and (d) voltage doubler.
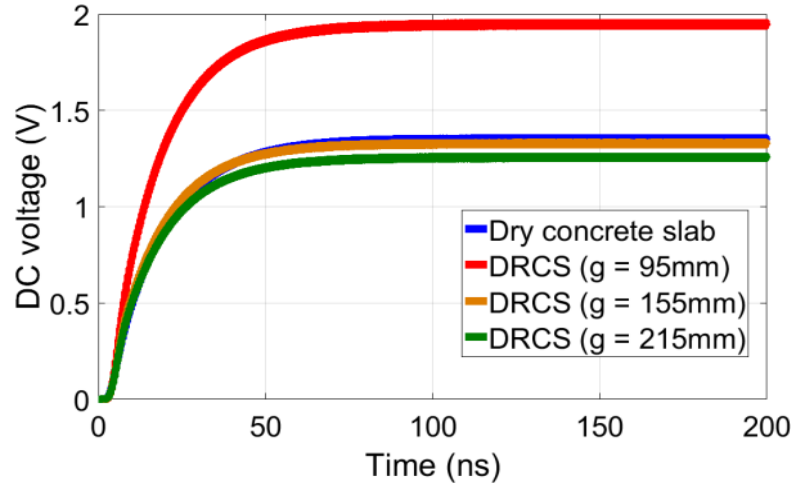
(a)
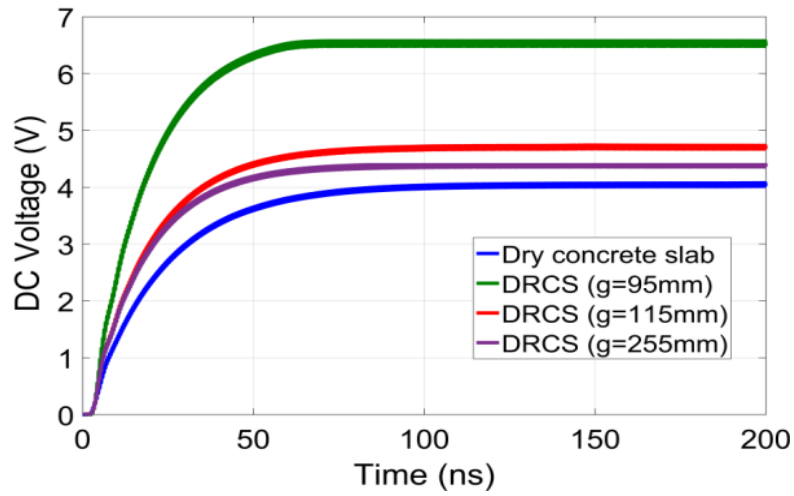
(b)

Figure 5.5 DC output voltage across the load at the (a) half wave rectifier and (b) voltage doubler embedded in dry reinforced concrete slab at different values of mesh period (*g*).

Moreover, the DC output voltage across the load inside the SRDS with different mesh periods is investigated, as shown in Table 5.4. It is clearly shown that the DC output voltage across the load at the half wave rectifier circuit is significantly lower than the DC output voltage at the voltage doubler. For instance, the DC voltage of voltage doubler in SRCS with *g* = 95 mm is almost four times higher than the DC voltage of the half wave rectifier.

Table 5.4 The DC output voltage across the load inside saturated reinforced concrete slab.

Rectifier circuit / Saturated concrete	Half-wave V_{DC} (v)	Voltage doubler V_{DC} (v)
Concrete slab	0.64	2.8
SRCS (g = 95mm)	0.7	3.2
SRCS (g = 115mm)	0.66	2.9
SRCS (g = 255mm)	0.6	2.8

In addition, the DC output voltage at dry and saturated reinforced concrete column with different values of steel ratios are investigated by using half wave and voltage doubler rectifier circuits. The values of the rectifier circuits parameters are the same as values are shown in Table 5.2 and Table 5.3. The results are shown in Fig. 5.6 and Fig. 5.7. As can be clearly seen from Fig. 5.6 and Fig. 5.7, the DC voltages received in DRCC is higher when polarisation of the antennas is parallel to longitudinal rebars than it is vertical one. For instance, in parallel configuration with 1% steel ratio the DC output voltage of the half wave rectifier and voltage doubler are 0.5 V and 1.5 V higher than vertical configuration. The obtained results confirm the results that have been achieved in the previous chapter. As mentioned before, the rebars in specific configuration cause the enhancement of the coupling between antennas; as a result the DC output voltage increases. As a results, the output DC voltages of the half wave rectifier and voltage doubler are sufficient to recharge the 80 mAH Nickel-metal hydride button cell battery and the 100 mAH ML 2430 series Sanyo lithium coin cell battery, respectively.

The DC output voltage of rectennas in SRCC is presented in Table 5.5. Similar to the SRCS, the received voltage at saturated concrete is significantly smaller than the ones for DRCC due to severe attenuation in saturated concrete. However, the Sanyo

lithium coin cell battery still can be recharged inside the SRCC while voltage doubler

used as a rectifier circuit.

Vertical configuration

(a)

Parallel configuration

(b)
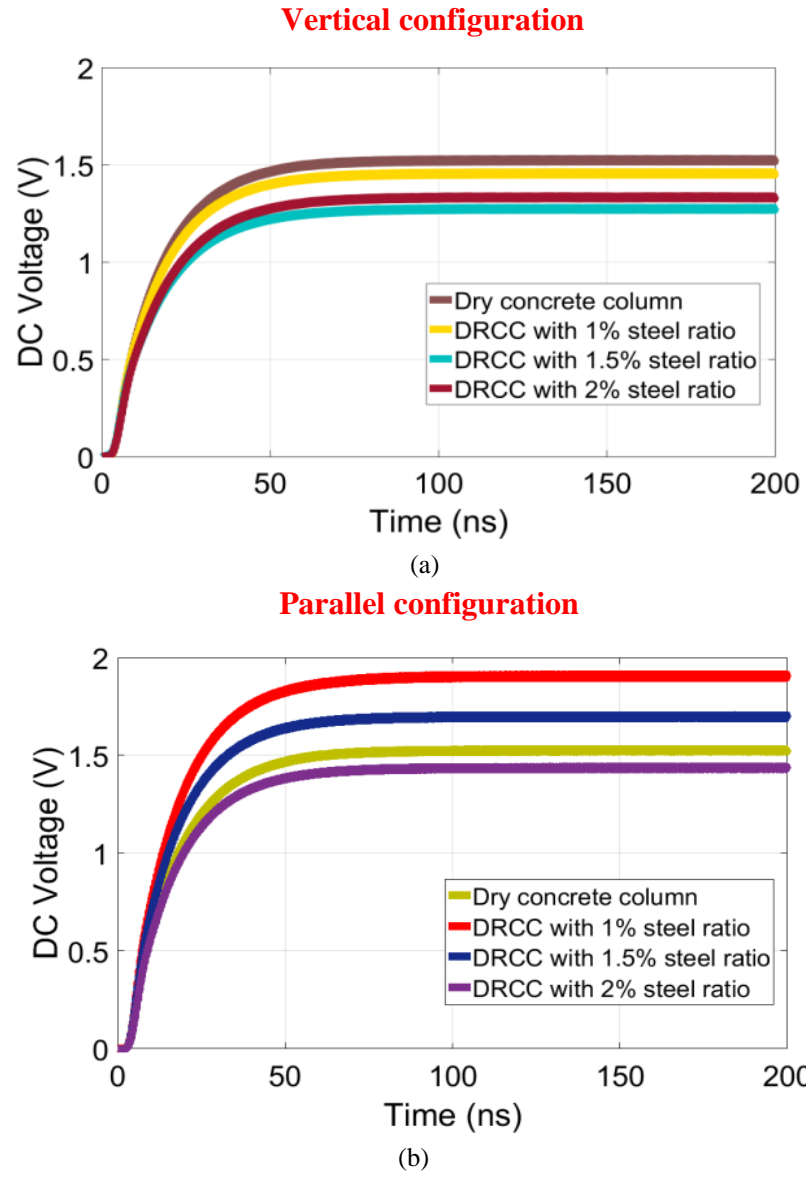
Figure 5.6 DC output voltage using half wave rectifier at dry reinforced concrete column with different steel ratios while polarisation of antennas are (a) vertical and (b) parallel to longitudinal rebars.
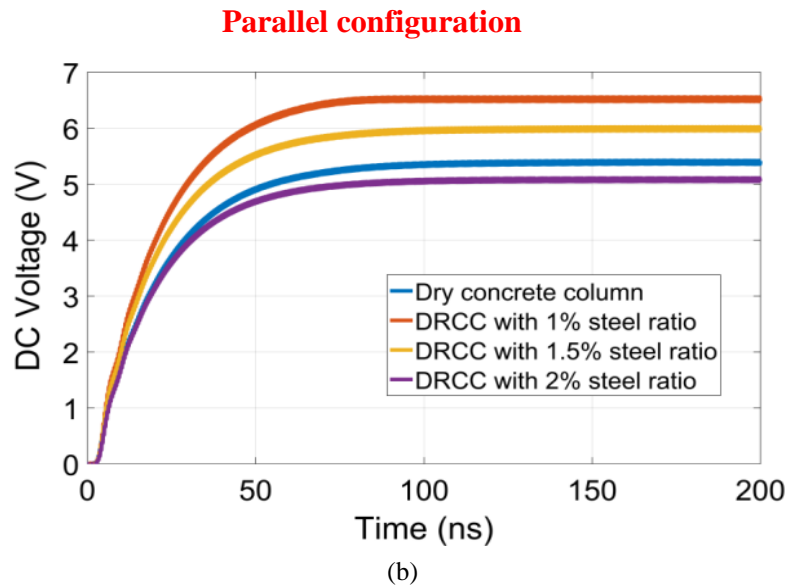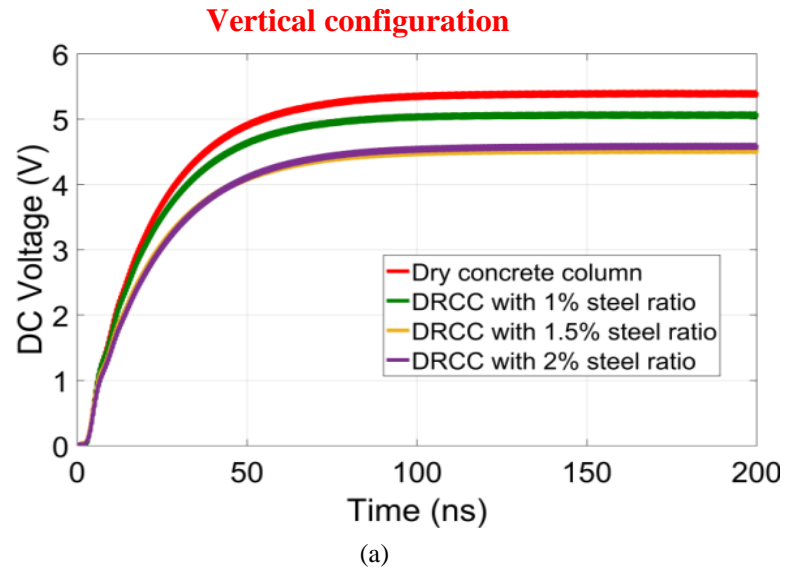
Figure 5.7 DC output voltage using voltage doubler at dry reinforced concrete column with different steel ratios while polarisation of antennas is (a) vertical and (b) parallel to longitudinal rebars.

Table 5.5 The DC output voltage across the load inside saturated reinforced concrete column.

Rectifier circuit	Half-wave		Voltage doubler	
	V_{DC} (v)		V_{DC} (v)	
Saturated concrete	Parallel	Vertical	Parallel	Vertical
Concrete column	0.78	0.75	2.82	2.8
SRCC (1%)	0.85	0.73	3.13	2.48
SRCC (1.5%)	0.8	0.78	2.93	2.94
SRCC (2%)	0.7	0.69	2.6	2.56

5.4 Resonant antipodal Vivaldi antenna array as a transmitting antenna

In this part, in order to increase directivity and gain of a transmitting antenna, and, as a result, the distance between the transmitting antenna and concrete surface for recharging the embedded sensor's battery, a 4-element resonant antipodal Vivaldi antenna array with a Wilkinson power divider feeding network is designed.

5.4.1 Wilkinson power divider

T-junction dividers, resistive dividers, and the Wilkinson power divider are three common power dividers featuring unique characteristics. These power dividers can be constructed using various types of transmission lines (i.e. waveguides, microstrip, or stripline) or using resistive networks. The advantages and disadvantages of these three dividers are summarised as follows (Kao et al. 2012; Zhou 2015):

- ➢ T-junction power divider: advantage of this type of the power divider is being loss less; however, all ports are not match and there is not isolation between output ports;

- ➢ Resistive power divider: advantage of this type of the power divider is that all ports can be matched; however, it is lossy, limited by resistor tolerance and there is not isolation between output ports;

- ➢ Wilkinson power divider: High isolation and low loss are advantages of this type of power divider; however, reflected power can be dissipated through the isolation resistor if there is mismatching.

The Wilkinson power divider can satisfy the ideal three-port network conditions such as being lossless, matched output ports with high isolation, and reciprocal.

Therefore, the Wilkinson power divider is the best choice and will be used in the optimized design of the corporate-fed network for the array.

A 4-way Wilkinson power divider has been designed to feed a 4-element RAVA array. It provides signals with equal amplitudes and phases over the 2 GHz to 3 GHz bandwidth. Rogers's 4003 substrate having a dielectric constant of 3.38, loss tangent of 0.0027 and thickness of 1.524mm was used to design the power divider. Fig. 5.8 shows the configuration of the designed Wilkinson power divider.

(a)

(b)
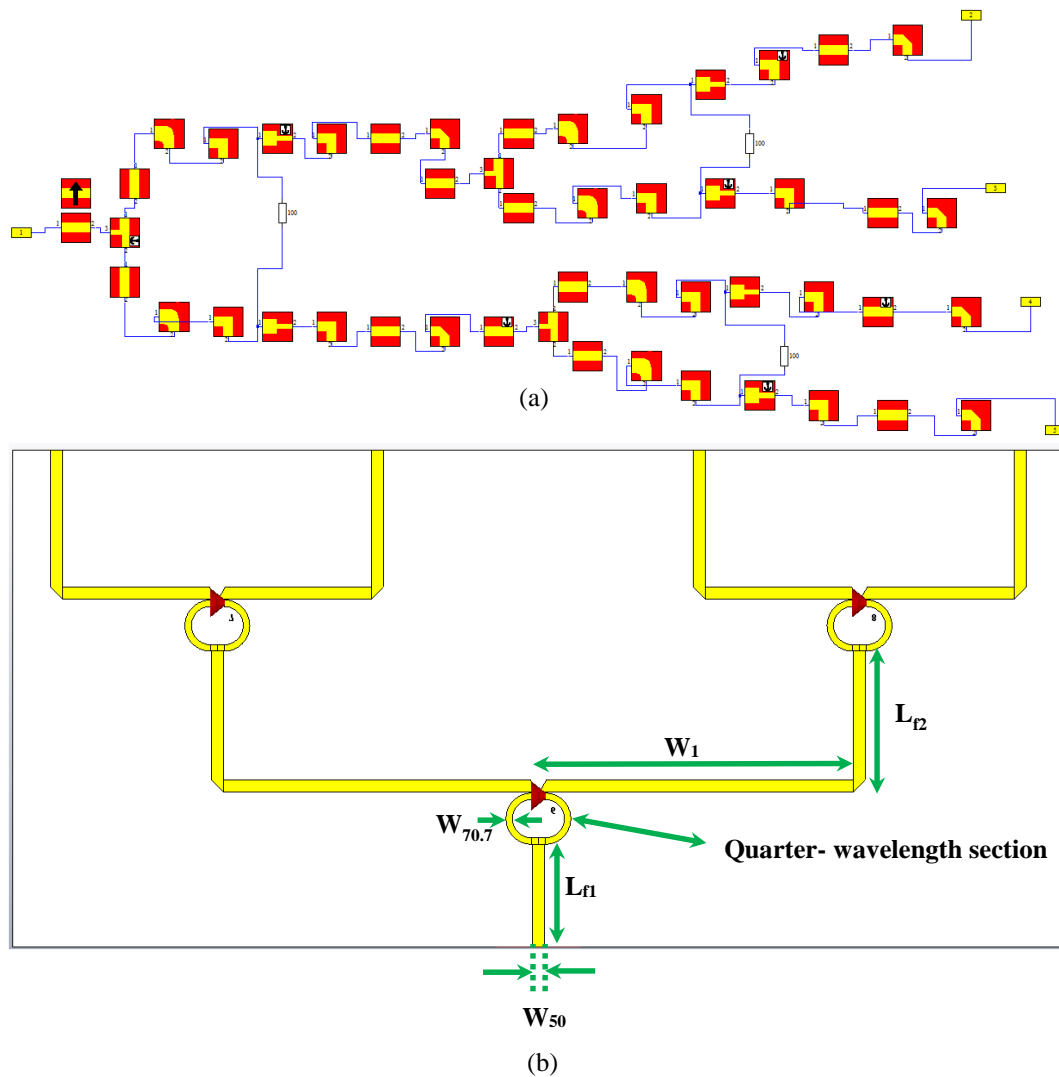
Figure 5.8 Designed Wilkinson power divider: (a) schematic and (b) layout.

The impedances of input and output ports of the proposed power divider are 50 Ω and the isolation resistor is $2Z_o = 100$ Ω. The impedance of the quarter-lambda transmission line split section is $\sqrt{2}Z_o = 70.7$ Ω. The optimised parameters of the designed power divider are as follows: $W_{50} = 3.5$ mm, $W_{70.7} = 1.9$ mm, $L_{f1} = 30$mm, $W_1 = 91.95$ mm, $L_{f2} = 41.2$ mm and the quarter-wavelength sections intended length is 23.56 mm. Fig. 5.9(a) shows S_{11} of the proposed power divider and Fig. 5.9(b) indicates its simulated isolation and insertion loss. As shown in Fig. 5.9, in the

(a)

(b)
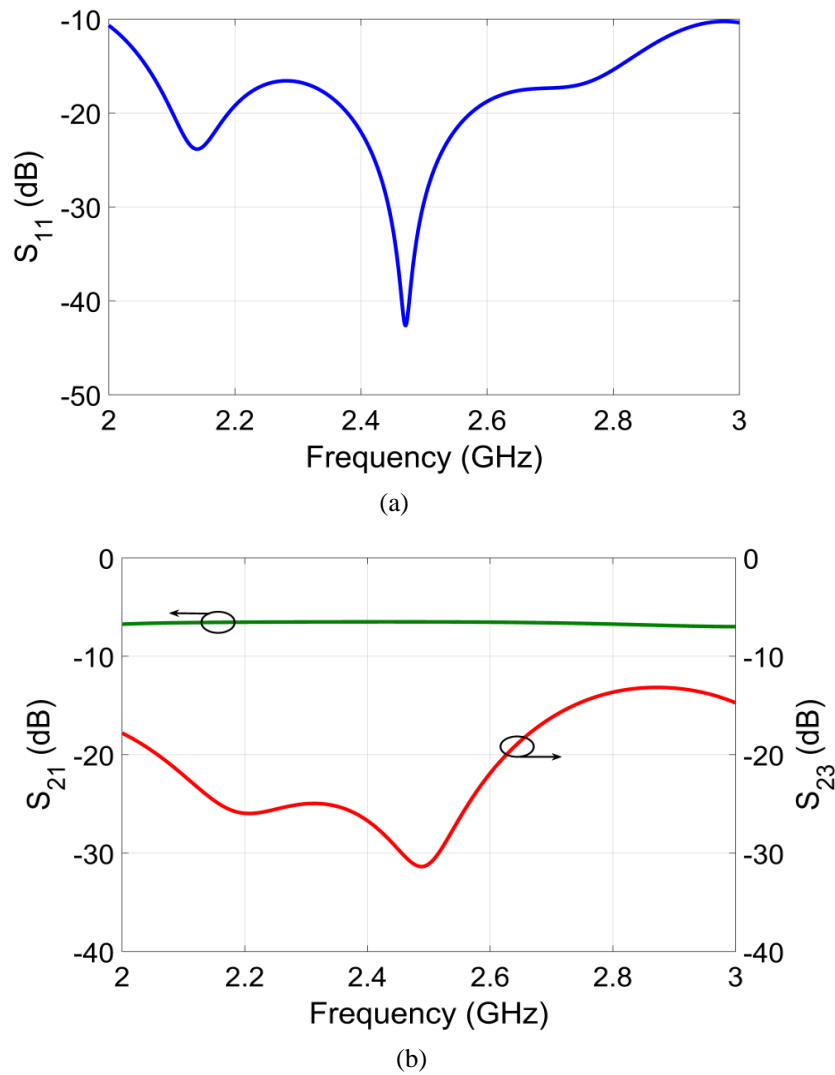
Figure 5.9 Simulated S-parameters of the designed Wilkinson power divider: (a) return loss (S_{11}) and (b) isolation (S_{21}) and insertion loss (S_{23}).

operating band from 2 GHz to 3GHz, the $S_{11}$is lower than -17 dB, in particular at 2.45

GHz it is less than -40 dB and output ports have almost equal power level with

insertion loss of -6.1dB.

5.4.2 2.45 GHz antipodal Vivaldi antenna array

This section presents the design of RAVA array antenna and study of its radiation

characteristics. The configuration of the single RAVA is already shown in Fig 4.1. A

4-element RAVA array was designed and connected to the proposed Wilkinson power

divider forming a 4-element linear antenna array. According to the theory of the

antenna array, the spacing between each element is a crucial parameter which

determines the directivity of the array. Wide spacing may result in a small mutual

coupling effect, narrow beam, but it becomes easier to generate grating lobe (Xu, H et

al. 2012). Therefore, the separation distance between the antenna elements are chosen

to be 0.76 λ at the 2.45 GHz to avoid grating lobes.

<div align="center">(a)   (b)</div>
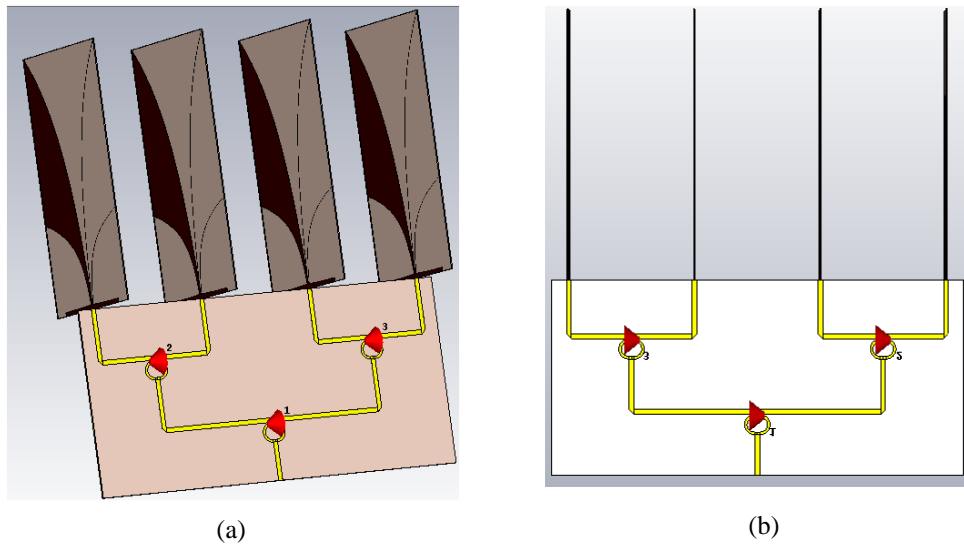
Figure 5.10 4-Element RAVA array with Wilkinson power divider feeding network:
(a) perspective view and (b) front view.

S_{11} of the RAVA array with Wilkinson power divider feeding network is shown in Fig. 5.11. It indicates that the array can operate from 2.3 GHz to 2.7 GHz with a magnitude of the reflection coefficient $< -10dB$.
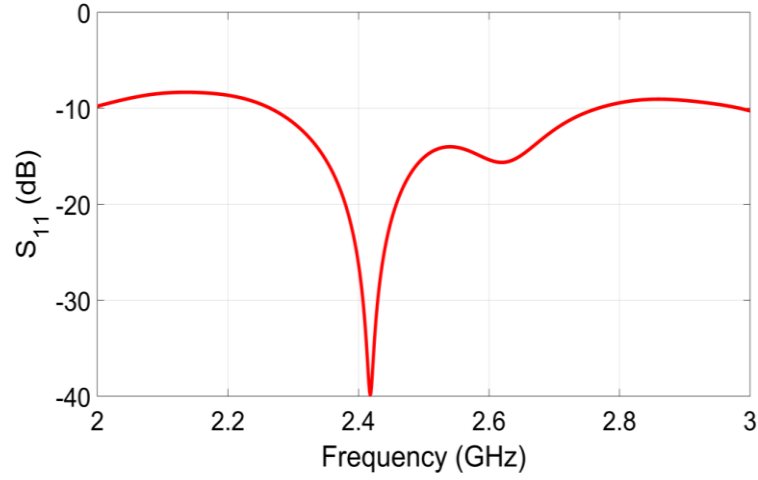
Figure 5.11 S_{11} of the RAVA array with Wilkinson power divider feeding network.

E- and H-plane radiation patterns of the single RAVA and the 4-element RAVA array with the feeding network are shown in Figs. 5.11 and Fig. 5.12, respectively. The use of the 4-element antenna array should add theoretically about 6 dB over the single element maximum gain. It can be seen from Figs. 5.11 and 5.12 that the gain is 6 dB higher in the array antenna than in the single RAVA.
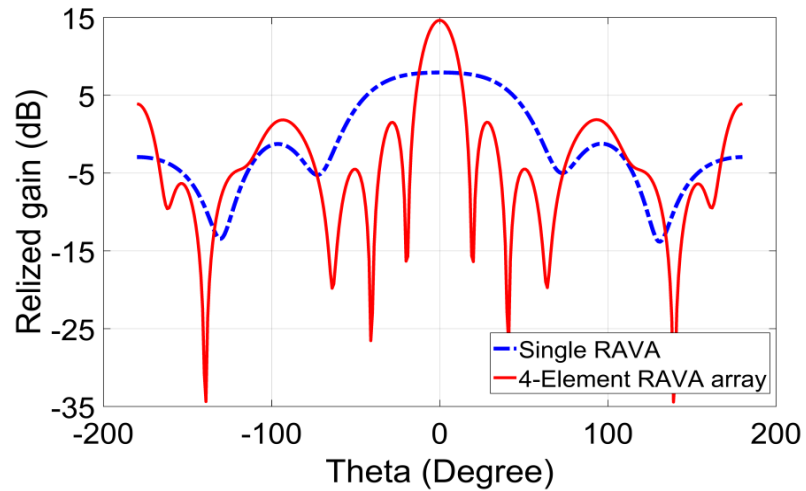
Figure 5.12 H-plane radiation pattern of the single RAVA and the RAVA array at 2.45 GHz.
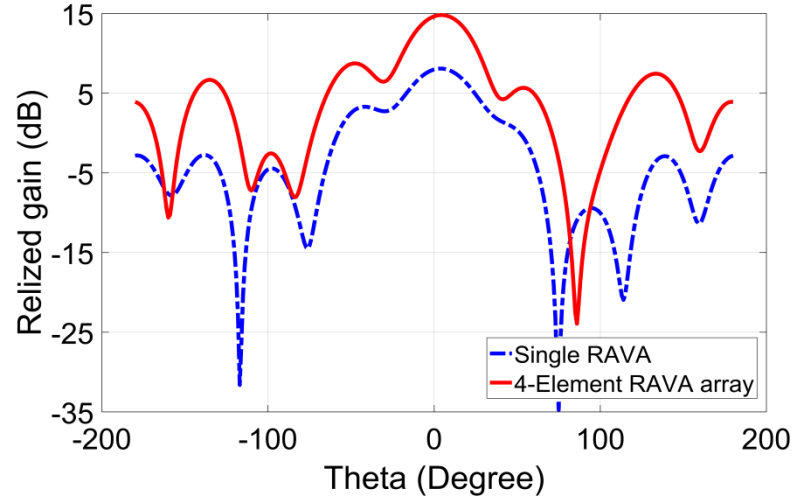
Figure 5.13 Realized gain of the RAVA and the RAVA array at 2.45 GHz.

5.5 Recharging battery of sensors embedded inside reinforced concrete slab and column using RAVA array

In this part, the RAVA array will be used as a transmitting antenna for recharging batteries of sensors embedded inside reinforced concrete. The RAVA array feed by the Wilkinson power divider is located at $L_1 = 0.6$ m and the rectenna consisting of the microstrip patch antenna along with a voltage doubler is placed at $L_2 = 85$ mm. The setup of the WPT system using array antenna is shown in Fig. 5.14. In CST DS, the power divider is connected to 3W power source with 50 Ω internal resistances. The optimise parameters of the voltage doubler are shown at Table 5.6.

The DC output voltage across the load while the rectenna is embedded inside DRCS and DRCC with the mesh period of 95 mm and 1% steel ratio, respectively, (see Fig. 5.4) is shown in Table 5.7. As can be seen from Table 5.7, the sufficient power can be achieved by proposed WPT system to recharge a 100 mAH ML 2430 series Sanyo lithium coin cell battery.
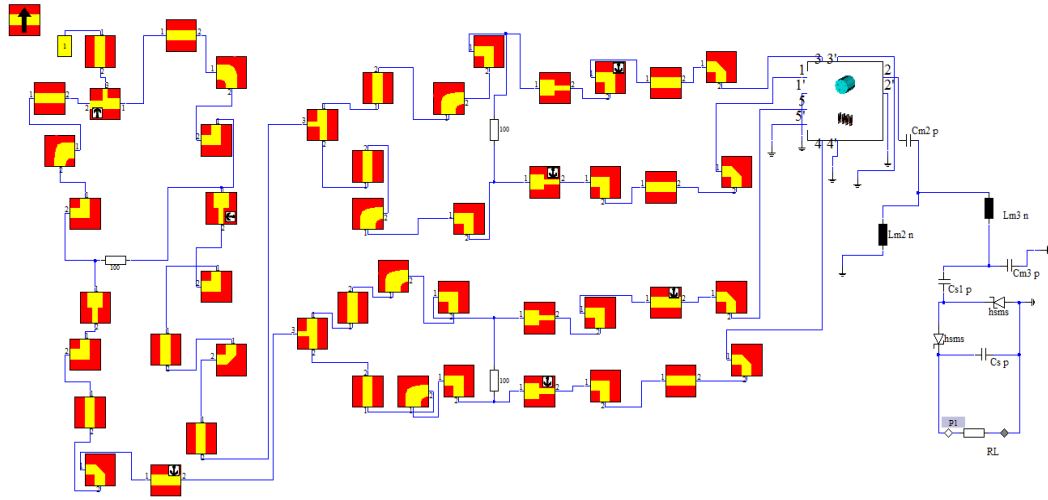
Figure 5.14 Simulated model of the WPT system in order to recharging battery of the sensor embedded inside reinforced concrete.

Table 5.6 Optimised parameter of the voltage doubler.

Parameter	value	Parameter	value
Lm2	14nH	Cm3	0.2pF
Lm3	4.5nH	Cs	40pF
Cm1	5.9 pF	RL	600Ω
Cs1	20pF		

Table 5.7 The DC output voltage across the load using the RAVA array.

Rectifier circuit / Dry concrete	Voltage doubler	
	V_{DC} (v)	P_{out} (mw)
Concrete slab	3.4	19.26
DRCS	5.44	49.32
Concrete column	5.23	45.6
DRCC (parallel)	5.4	46.8
DRCC (Vertical)	4.5	33.75

5.6 Summary

In this chapter, two WPT systems with the RAVA for recharging batteries of sensors embedded inside reinforced concrete slabs and columns with different configurations and moisture content were developed. For these systems, an embeddable rectenna with a microstrip patch antenna and relatively high efficiency rectified circuits was designed and applied. It was shown that one of the systems including the single RAVA as a transmitting antenna provided the DC output voltage sufficient for recharging commonly used battery at the distance between the transmitting antenna and the surface of reinforced concrete members of 0.12 m which can be too small in practice. A relatively high gain 4-element RAVA array along with Wilkinson power divider feeding network have been developed in order to increase the distance between a transmitting antenna and concrete surface. The results of the investigation of another WPT system with this antenna array as a transmitting antenna showed that it provided the sufficient DC output voltage at the distance between the transmitting antenna and the surface of reinforced concrete members of 0.6 m, which is 5 times longer that the distance achieved with the single RAVA. Finally, it can be concluded that to design optimum WPT systems for recharging batteries of sensors embedded inside reinforced concrete, the position of rectanna inside concrete and the position transmitting antenna in free space, and selection of rectification circuit type should be carefully considered.

Chapter 6 Conclusions and future work

6.1 Conclusions

The results of this thesis show that the developed modified Vivaldi antennas can be an effective part of microwave systems for IHM applications including the detection of defects such as air gaps inside concrete and wireless powering sensors or recharging their batteries embedded in concrete members such as reinforced concrete slabs and columns. The design of antennas, the results of the investigation into the reflection and transmission properties and wireless power transmission in reinforced concrete samples irradiated by the developed antennas are the main contributions of this thesis. The major outcomes and recommendations are outlined as follows:

1. A modified antipodal Vivaldi antenna (MAVA) operating at the frequency range of 0.65 GHz – 6 GHz, including three frequency bands of the Industrial, Scientific and Medical band with improved gain at low frequencies was developed, built and tested in free space and with concrete samples. There is a good agreement between measurement and simulation results. The developed antenna can be used for nondestructive testing and evaluation of construction materials and structures including concrete-based members, communication between wireless sensors and nodes, and for wireless powering sensors embedded in construction materials.

2. The reflection and transmission properties of concrete-based samples possessing air gap or rebars and irradiated by the developed MAVA are investigated numerically and experimentally. It is shown that the magnitude of reflection coefficient changes linearly when gap value increases at selected frequencies. This result can be used for the detection and evaluation of gaps in

127

concrete. The investigation into the influence of rebars on the reflection and transmission properties shows that it depends on the value of rebar cell parameter and the cell can act as a shield for microwaves if this parameter was less than the electrical half wavelength. At higher frequencies of the frequency range, microwaves can penetrate through the reinforced concrete samples with a rebar cell parameter used in practice. These results have been used for the investigation into the transmission of microwaves between the MAVA and a microstrip patch antenna embedded inside dry reinforced concrete samples near the location of the rebar cell at 2.45 GHz. It is shown that -15-dB coupling between the antennas can be achieved. Overall, the results show that the reflection and transmission properties of reinforced concrete structures depend on an operating frequency, radiation performance of antennas, rebar cell configuration and parameter, electromagnetic properties of concrete and localization of antennas with respect to boundaries of concrete members and rebars.

3. A relatively small and high-gain resonant antipodal Vivaldi antenna (RAVA) and a modified embeddable microstrip patch antenna as a transmitting and receiving antennas, respectively, were designed for wireless power transmission in concrete structures. The RAVA is based on a relatively small broadband conventional AVA but a resonance is added to get to the operating frequency at 2.45 GHz with reduced dimensions of the antenna and for potential applications such as wireless communication, sensing and/or power transmission. The two-antenna setup was used with reinforced dry and saturated concrete slabs and columns with different values of mesh period of rebars and steel ratio, respectively. It was shown that maximum coupling

between antennas is achieved at a practical value of mesh period of rebars in the slabs which is related to wavelength in concrete. The coupling between the antennas in the saturated concrete is always lower and reduces faster than in the dry concrete when the distance between the embedded patch antenna and the surface of concrete increases due to the increase of loss in concrete. It was also shown that in the case of reinforced concrete columns polarisation configuration of the two-antenna setup with respect to rebars and steel ratios as well as losses in concrete are the most important parameters. The coupling between antennas reduced faster by increasing the value of steel ratio at parallel than in vertical configuration due to the increase of the interaction between microwaves and rebars. This effect was more prominent in the saturated than in dry reinforced concrete columns.

4. A relatively high-gain 4-element resonant antipodal Vivaldi antenna array with a Wilkinson power divider feeding network was developed to be used as a relatively long-distance transmitting antenna. To satisfy requirements for recharging batteries of the embedded sensors, embeddable rectenna consisting of the microstrip patch antenna and a rectifier circuit is developed.

5. A comparative investigation of wireless power transmission systems with the developed single antenna and antenna array for recharging batteries of sensor embedded inside reinforced concrete slabs and columns with different configurations and moisture content was provided. The results show that the DC output voltagefor recharging a commonly used battery can be provided by the systems with the single RAVA and the system with the RAVA array at a distance between the transmitting antenna and the surface of reinforced concrete members of 0.12 m and 0.6 m, respectively, i.e. the distance achieved

with the array is 5 times longer than the distance achieved with the single antenna. Therefore, the developed RAVA array has a good potential as a relatively long-distance transmitting antenna for wireless power transmission in concrete.

6.2 Suggestions for future work

The recommendations for future research in this area are as follows:

1. The efficiency of wireless power transmission and/or depth of sensor localisation in concrete can be increased at the 902-928 MHz ISM band. For this purpose, the developed MAVA can be used or modified and a miniaturised embeddable rectenna should be developed.

2. CMOS based multi-stage rectifiers could be utilised to increase the RF to DC conversion efficiency and decrease the rectenna size.

3. This research can be extended to the development of systems involving communication with passive sensors without batteries using embedded integrated RFID tag antenna with sensory functions and an external reader with the developed antennas.

4. The investigation into the possibility of increasing the distance between a transmitting antenna and surface of concrete would be useful.

5. The developed antennas can be incorporated in microwave imaging systems for non-destructive testing and evaluation of concrete-based structures to detect flaws such as real cracks, impact damages and voids using their two- and three-dimensional images. It can be a valuable addition to recently developed antipodal Vivaldi antennas such as one presented in (Moosazadeh, Kharkovsky & Case 2016).

References

Airani, KC, Vinay, V, Kumar, PP & Kumaraswamy, H 2016, 'Rectangular and elliptical microstrip patch antennas for wireless power transmission', in *Wireless Communications, Signal Processing and Networking (WiSPNET), International Conference on*, pp. 1781-5.

Akbari, S 2014, 'Energy harvesting for wireless sensor networks review', in *Computer Science and Information Systems (FedCSIS), 2014 Federated Conference on*, pp. 987-92.

Ali, M, Yang, G & Dougal, R 2005, 'A new circularly polarized rectenna for wireless power transmission and data communication', *IEEE Antennas and Wireless Propagation Letters*, vol. 4, pp. 205-8.

Ali, M, Yang, G & Dougal, R 2005, 'A wideband circularly polarized rectenna for wireless power transmission to embedded sensors', in *IEEE Annual Conference on wireless and Microwave Technology*, pp. 11-.

Andringa, MM, Neikirk, DP, Dickerson, NP & Wood, SL 2005, 'Unpowered wireless corrosion sensor for steel reinforced concrete', in *Sensors, 2005 IEEE*, p. 4 pp.

Ashraf, MA, Jamil, K, Sebak, A, Shoaib, M, Alhekail, Z, Alkanhal, M & Alshebeili, S 2015, 'Modified Antipodal Vivaldi Antenna with Shaped Elliptical Corrugation for 1–18-GHz UWB Application', *Applied Computational Electromagnetics Society Journal*, vol. 30, no. 1, pp. 68-77.

Ba, HC, Shirai, H & Ngoc, CD 2014, 'Analysis and design of antipodal Vivaldi antenna for UWB applications', in *Communications and Electronics (ICCE), 2014 IEEE Fifth International Conference on*, pp. 391-4.

Bai, J, Shi, S & Prather, DW 2011, 'Modified compact antipodal Vivaldi antenna for 4–50-GHz UWB application', *IEEE Transactions on Microwave Theory and Techniques*, vol. 59, no. 4, pp. 1051-7.

Balanis, CA 2016, *Antenna theory: analysis and design*, John Wiley & Sons.

Bernhard, J, Hietpas, K, George, E, Kuchima, D & Reis, H 2003, 'An interdisciplinary effort to develop a wireless embedded sensor system to monitor and assess corrosion in the tendons of prestressed concrete girders', in *Wireless Communication Technology, 2003. IEEE Topical Conference on*, pp. 241-3.

Bhattacharyya, D, Kim, T-h & Pal, S 2010, 'A comparative study of wireless sensor networks and their routing protocols', *Sensors*, vol. 10, no. 12, pp. 10506-23.

Bhuiyan, MZA, Wang, G, Cao, J & Wu, J 2015, 'Deploying wireless sensor networks with fault-tolerance for structural health monitoring', *IEEE Transactions on Computers*, vol. 64, no. 2, pp. 382-95.

Bird, TS 2016, *Fundamentals of Aperture Antennas and Arrays: From Theory to Design, Fabrication and Testing*, John Wiley & Sons.

Biswas, MM, Zobayer, U, Hossain, MJ, Ashiquzzaman, M & Saleh, M 2012, 'Design a Prototype of Wireless Power Transmission System Using RF/Microwave and Performance Analysis of Implementation', *International Journal of Engineering and Technology*, vol. 4, no. 1, p. 61.

Brown, J & Jull, E 1961, 'The Prediction of Aerial Patterns From Near-Field Measurements', *IEE (London)*, pp. 635-44.

Brown, WC 1976, 'Optimization of the efficiency and other properties of the rectenna element', in *Microwave Symposium, 1976 IEEE-MTT-S International*, pp. 142-4.

—— 1980, 'The history of the development of the rectenna', in *Solar Power Satellite Microwave Power Transmission and Reception*, vol. 2141, p. 271.

—— 1986, 'A microwaver powered, long duration, high altitude platform', in *1986 IEEE MTT-S International Microwave Symposium Digest*, pp. 507-10.

Bruns, C, Leuchtmann, P & Vahldieck, R 2003, 'Analysis and simulation of a 1-18-GHz broadband double-ridged horn antenna', *IEEE Transactions on electromagnetic compatibility*, vol. 45, no. 1, pp. 55-60.

Buyukozturk, O 1997, 'Electromagnetic Properties of Concrete and Their Significancein Nondestructive Testing', *Transportation Research Record: Journal of the Transportation Research Board*, no. 1574, pp. 10-7.

Carkhuff, B & Cain, R 2003, 'Corrosion sensors for concrete bridges', *IEEE instrumentation & measurement magazine*, vol. 6, no. 2, pp. 19-24.

Chan, TH & Thambiratnam, DP 2011, *Structural health monitoring in Australia*, Nova Science Publishers.

Choi, K-K 2002, 'Reinforced Concrete Structure Design Assistant Tool for Beginners', UNIVERSITY OF SOUTHERN CALIFORNIA.

Congedo, F, Monti, G, Tarricone, L & Bella, V 2013, 'A 2.45-GHz Vivaldi Rectenna for the Remote Activation of an End Device Radio Node', *IEEE Sensors Journal*, vol. 9, no. 13, pp. 3454-61.

Daniel Tomicek, YHT, Winston K.G. Seah and Ramesh K. Rayudu 2013, 'Vibration-powered wireless sensors for structure monitoring during earthquake', paper presented to The 6th International Conference on Structural Health Monitoring of Intelligent Infrastructure, Hong Kong, 9-11 December 2013.

de Medeiros, R, Lopes, HM, Guedes, RM, Vaz, MA, Vandepitte, D & Tita, V 2015, 'A new methodology for Structural Health Monitoring applications', *Procedia Engineering*, vol. 114, pp. 54-61.

Deivasigamani, A, Daliri, A, Wang, CH & John, S 2013, 'A review of passive wireless sensors for structural health monitoring', *Modern Applied Science*, vol. 7, no. 2, p. 57.

Dhake, NB & Dandavate, AA 2012, 'Wireless Power Transmission Using Microwaves', *IJEIR*, vol. 1, no. 2, pp. 114-9.

Dobkin, D 2008, 'The RF in RFID passive UHF in practice', *United States of America, Newness*.

Epp, LW, Khan, AR, Smith, HK & Smith, RP 2000, 'A compact dual-polarized 8.51-GHz rectenna for high-voltage (50 V) actuator applications', *IEEE Transactions on Microwave Theory and Techniques*, vol. 48, no. 1, pp. 111-20.

Farinholt, KM, Park, G & Farrar, CR 2009, 'RF energy transmission for a low-power wireless impedance sensor node', *IEEE Sensors Journal*, vol. 9, no. 7, pp. 793-800.

Feucht, DL 2014, *Handbook of analog circuit design*, Academic Press.

Fioranelli, F, Salous, S, Ndip, I & Raimundo, X 2015, 'Through-the-wall detection with gated FMCW signals using optimized patch-like and vivaldi antennas', *IEEE Transactions on Antennas and Propagation*, vol. 63, no. 3, pp. 1106-17.

Gazit, E 1988, 'Improved design of the Vivaldi antenna', in *IEE Proceedings H-Microwaves, Antennas and Propagation*, vol. 135, pp. 89-92.

Gibson, P 1979, 'The vivaldi aerial', in *Microwave Conference, 1979. 9th European*, pp. 101-5.

Gilbert, RA & Volakis, J 2007, *Antenna engineering handbook*, Mc. Graw-Hill.

Goto, N 1990, *Slotted waveguide antenna*, Google Patents.

Hagerty, JA, López, ND, Popovic, B & Popovic, Z 2000, 'Broadband rectenna arrays for randomly polarized incident waves', in *Microwave Conference, 2000. 30th European*, pp. 1-4.

Han, S-M, Park, J-Y & Itoh, T 2004a, 'Active integrated antenna based rectenna using the circular sector antenna with harmonic rejection', in *Antennas and Propagation Society International Symposium, 2004. IEEE*, vol. 4, pp. 3533-6.

—— 2004b, 'Dual-fed circular sector antenna system for a rectenna and a RF receiver', in *Microwave Conference, 2004. 34th European*, vol. 2, pp. 1089-92.

Harrist, DW 2004, 'Wireless battery charging system using radio frequency energy harvesting', University of Pittsburgh.

Heljo, PS, Li, M, Lilja, KE, Majumdar, HS & Lupo, D 2013, 'Printed half-wave and full-wave rectifier circuits based on organic diodes', *IEEE Transactions on Electron Devices*, vol. 60, no. 2, pp. 870-4.

Hsin-Loug, L & Ta-Lun, L 2001, *Parabolic reflector antenna*, Google Patents.

Huang, Y & Boyle, K 2008, *Antennas: from theory to practice*, John Wiley & Sons.

Itoh, K 1984, *Study of rectenna as ground site of solar power satellite*, Tech. Rep. Grant-in-Aid Scientific Res.[Grant-in-Aid Sci. Res.(A)].

Itoh, K 2015, 'RF bridge rectifier and its good possibility for wireless power transmission systems', in *Radio-Frequency Integration Technology (RFIT), 2015 IEEE International Symposium on*, pp. 226-8.

Jamil, M, Hassan, M, Al-Mattarneh, H & Zain, MFM 2013, 'Concrete dielectric properties investigation using microwave nondestructive techniques', *Materials and structures*, vol. 46, no. 1-2, pp. 77-87.

Jiang, S & Georgakopoulos, SV 2010, 'Optimum power transmission of wireless sensors embedded in concrete', in *2010 IEEE International Conference on RFID (IEEE RFID 2010)*, pp. 237-44.

—— 2011, 'Optimum wireless power transmission through reinforced concrete structure', in *2011 IEEE International Conference on RFID*, pp. 50-6.

—— 2012, 'Optimum wireless powering of sensors embedded in concrete', *IEEE Transactions on Antennas and Propagation*, vol. 60, no. 2, pp. 1106-13.

Jiang, S, Georgakopoulos, SV & Jin, H 2012, 'Effects of periodic reinforced-concrete structures on power transmission', in *2012 IEEE International Conference on RFID (RFID)*, pp. 16-23.

Jiang, S, Georgakopoulos, SV & Jonah, O 2012, 'Power transmission for sensors embedded in reinforced concrete structures', in *Proceedings of the 2012 IEEE International Symposium on Antennas and Propagation*.

Jin, X & Ali, M 2009, 'Reflection and transmission properties of embedded dipoles and PIFAs inside concrete at 915 MHz', in *2009 IEEE Antennas and Propagation Society International Symposium*, pp. 1-4.

—— 2010, 'Embedded antennas in dry and saturated concrete for application in wireless sensors', *Progress in electromagnetics research*, vol. 102, pp. 197-211.

Jonah, O & Georgakopoulos, SV 2011, 'Wireless power transmission to sensors embedded in concrete via magnetic resonance', in *Wireless and Microwave Technology Conference (WAMICON), 2011 IEEE 12th Annual*, pp. 1-6.

Kanjaa, M, Mrabet, OE, Khalladi, M & Essaaidi, M 2015, 'Exponentially tapered antipodal Vivaldi antenna for breast cancer detection', in *Microwave Symposium (MMS), 2015 IEEE 15th Mediterranean*, pp. 1-3.

Kao, J-C, Tsai, Z-M, Lin, K-Y & Wang, H 2012, 'A modified Wilkinson power divider with isolation bandwidth improvement', *IEEE Transactions on Microwave Theory and Techniques*, vol. 60, no. 9, pp. 2768-80.

Kijewski-Correa, T, Haenggi, M & Antsaklis, P 2006, 'Wireless sensor networks for structural health monitoring: a multi-scale approach', in *ASCE Structures 2006 Congress*.

Knight, DW 1st Jan. 2016., 'Diode detectors for RF measurement; Part 1: Rectifier circuits, theory and calculation procedures.'.

Kraus, JD 1988, 'Antennas'.

Li, Z, Kang, X, Su, J, Guo, Q, Yang, YL & Wang, J 2016, 'A Wideband End-Fire Conformal Vivaldi Antenna Array Mounted on a Dielectric Cone', *International Journal of Antennas and Propagation*, vol. 2016.

Maierhofer, C & Wöstmann, J 1998, 'Investigation of dielectric properties of brick materials as a function of moisture and salt content using a microwave impulse technique at very high frequencies', *NDT & E International*, vol. 31, no. 4, pp. 259-63.

Mascareñas, D, Flynn, E, Todd, M, Park, G & Farrar, C 2008, 'Wireless sensor technologies for monitoring civil structures', *Sound and Vibration*, vol. 42, no. 4, pp. 16-21.

McSpadden, JO, Fan, L & Chang, K 1997, 'A high conversion efficiency 5.8 GHz rectenna', in *Microwave Symposium Digest, 1997., IEEE MTT-S International*, vol. 2, pp. 547-50.

Milligan, TA 2005, *Modern antenna design*, John Wiley & Sons.

Moosazadeh, M & Kharkovsky, S 2015, 'Development of the antipodal Vivaldi antenna for detection of cracks inside concrete members', *Microwave and Optical Technology Letters*, vol. 57, no. 7, pp. 1573-8.

Moosazadeh, M, Kharkovsky, S & Case, JT 2016, 'Microwave and millimetre wave antipodal Vivaldi antenna with trapezoid-shaped dielectric lens for imaging of construction materials', *IET Microwaves, Antennas & Propagation*, vol. 10, no. 3, pp. 301-9.

Nassar, IT & Weller, TM 2015, 'A Novel Method for Improving Antipodal Vivaldi Antenna Performance', *IEEE Transactions on Antennas and Propagation*, vol. 63, no. 7, pp. 3321-4.

Natarajan, R, George, JV, Kanagasabai, M, Lawrance, L, Moorthy, B, Rajendran, DB & Alsath, MGN 2016, 'Modified antipodal Vivaldi antenna for ultra-wideband communications', *IET Microwaves, Antennas & Propagation*, vol. 10, no. 4, pp. 401-5.

Ni, Y, Wong, K & Xia, Y 2011, 'Health checks through landmark bridges to sky-high structures', *Advances in Structural Engineering*, vol. 14, no. 1, pp. 103-19.

Nikolaou, S, Marcaccioli, L, Ponchak, GE, Papapolymerou, J & Tentzeris, MM 2005, 'Conformal double exponentially tapered slot antennas (DETSA) for UWB communications systems' front-ends', in *2005 IEEE International Conference on Ultra-Wideband*, pp. 196-200.

Pozar, DM 2012, *Microwave engineering*, Addison-Wesley.

Priya, S 2005, 'Modeling of electric energy harvesting using piezoelectric windmill', *Applied Physics Letters*, vol. 87, no. 18, p. 184101.

Raghunathan, V, Kansal, A, Hsu, J, Friedman, J & Srivastava, M 2005, 'Design considerations for solar energy harvesting wireless embedded systems', in *Proceedings of the 4th international symposium on Information processing in sensor networks*, p. 64.

Ro, H-S, Park, G-M, Kim, S-t, Lee, S-Y, Mi-Kyung, S, Kang, H-Y & Choi, Y-S 2014, *Log periodic antenna*, Google Patents.

Ruvio, G, Gaetano, D, Ammann, MJ & McEvoy, P 2012, 'Antipodal Vivaldi antenna for water pipe sensor and telemetry', *International Journal of Geophysics*, vol. 2012.

Salama, R & Kharkovsky, S 2013, 'An embeddable microwave patch antenna module for civil engineering applications', in *2013 IEEE International Instrumentation and Measurement Technology Conference (I2MTC)*, pp. 27-30.

Savant, CJ 1987, *Electric circuit design: an engineering approach*, Benjamin-Cummings Publishing Co., Inc.

Sazonov, E, Li, H, Curry, D & Pillay, P 2009, 'Self-powered sensors for monitoring of highway bridges', *IEEE Sensors Journal*, vol. 9, no. 11, pp. 1422-9.

Schaubert, D, Kollberg, E, Korzeniowski, T, Thungren, T, Johansson, J & Yngvesson, K 1985, 'Endfire tapered slot antennas on dielectric substrates', *IEEE Transactions on Antennas and Propagation*, vol. 33, no. 12, pp. 1392-400.

Shaari, A, Millard, S & Bungey, J 2004, 'Modelling the propagation of a radar signal through concrete as a low-pass filter', *NDT & E International*, vol. 37, no. 3, pp. 237-42.

Shams, KM & Ali, M 2007, 'Wireless power transmission to a buried sensor in concrete', *IEEE Sensors Journal*, vol. 7, no. 12, pp. 1573-7.

Shams, KM, Ali, M & Miah, AM 2006, 'Characteristics of an embedded microstrip patch antenna for wireless infrastructure health monitoring', in *2006 IEEE Antennas and Propagation Society International Symposium*.

Shams, KM, Miah, AM & Ali, M 2007, 'Gain and transmission properties of an embedded microstrip patch antenna for structural health monitoring application', in *2007 IEEE Antennas and Propagation Society International Symposium*, pp. 908-11.

Shao, W & Adams, RS 2016, *Antipodal vivaldi antenna array for biomedical imaging*, Google Patents.

Shibata, T, Sasaya, T & Kawahara, N 2001, 'Development of in-pipe microrobot using microwave energy transmission', *Electronics and Communications in Japan (Part II: Electronics)*, vol. 84, no. 11, pp. 1-8.

Shinohara, N 2011, 'Power without wires', *IEEE Microwave Magazine*, vol. 12, no. 7, pp. S64-S73.

Shinohara, N, Kunimi, S, Miura, T, Matsumoto, H & Fujiwara, T 1998, 'Open experiment of microwave power experiment with automatically target chasing system', *IEICE Trans. B-II, J81-B-II (6)*, pp. 657-61.

Siddiqui, J, Antar, Y, Freundorfer, A, Smith, E, Morin, G & Thayaparan, T 2011, 'Design of an ultrawideband antipodal tapered slot antenna using elliptical strip conductors', *IEEE Antennas and Wireless Propagation Letters*, no. 10, pp. 251-4.

Singh, I & Tripathi, DV 2011, 'Micro strip patch antenna and its applications: a survey', *Int. J. Comp. Tech. Appl*, vol. 2, no. 5, pp. 1595-9.

Sodano, HA, Simmers, GE, Dereux, R & Inman, DJ 2007, 'Recharging batteries using energy harvested from thermal gradients', *Journal of Intelligent Material Systems and Structures*, vol. 18, no. 1, pp. 3-10.

Soutsos, M, Bungey, J, Millard, S, Shaw, M & Patterson, A 2001, 'Dielectric properties of concrete and their influence on radar testing', *NDT & E International*, vol. 34, no. 6, pp. 419-25.

Studio, M 2015, 'Computer Simulation Technology (CST)', *Online: www. cst. com*.

Tesla, N 1904, 'The transmission of electrical energy without wires', *Electrical World and Engineer*, vol. 1.

Volakis, JL & Johnson, R 1755, *Antenna Engineering Handbook, 2007*, McGraw-Hill Professional.

Wang, D-H & Liao, W-H 2006, 'Wireless transmission for health monitoring of large structures', *IEEE transactions on instrumentation and measurement*, vol. 55, no. 3, pp. 972-81.

Wang, Y & Fathy, AE 2008, 'Design of a compact tapered slot Vivaldi antenna array for see through concrete wall UWB applications', *Proceedings of the XXIXth URSI General Assembly in Chicago*.

Wang, Y, Zhang, F, Fang, G, Ji, Y, Ye, S & Zhang, X 2016, 'A Novel Ultrawideband Exponentially Tapered Slot Antenna of Combined Electric-Magnetic Type', *IEEE Antennas and Wireless Propagation Letters*, vol. 15, pp. 1226-9.

Wang, Z & Xie, X 2012, 'Design and optimization of the antenna applied for detecting the voids in tunnel lining by GPR', in *Ground Penetrating Radar (GPR), 2012 14th International Conference on*, pp. 131-6.

Wang, Z, Yin, Y, Wu, J & Lian, R 2016, 'A Miniaturized CPW-Fed Antipodal Vivaldi Antenna With Enhanced Radiation Performance for Wideband Applications', *IEEE Antennas and Wireless Propagation Letters*, vol. 15, pp. 16-9.

Waterhouse, R 2007, *Printed antennas for wireless communications*, Wiley Online Library.

Wu, J, Yuan, S, Ji, S, Zhou, G, Wang, Y & Wang, Z 2010, 'Multi-agent system design and evaluation for collaborative wireless sensor network in large structure health monitoring', *Expert Systems with Applications*, vol. 37, no. 3, pp. 2028-36.

Wu, K, Choudhury, D & Matsumoto, H 2013, 'Wireless power transmission, technology, and applications [Scanning the issue]', *Proceedings of the IEEE*, vol. 101, no. 6, pp. 1271-5.

Xu, H, Zhao, G, Zhang, Z, Sun, H & Lv, X 2012, 'Antipodal Vivaldi antenna for phased array antenna applications', in *Proceedings of 2012 5th Global Symposium on Millimeter-Waves*.

Xu, N, Rangwala, S, Chintalapudi, KK, Ganesan, D, Broad, A, Govindan, R & Estrin, D 2004, 'A wireless sensor network for structural monitoring', in *Proceedings of the 2nd international conference on Embedded networked sensor systems*, pp. 13-24.

Yang, Y, Wang, Y & Fathy, AE 2008, 'Design of compact Vivaldi antenna arrays for UWB see through wall applications', *Progress in electromagnetics research*, vol. 82, pp. 401-18.

Zhang, F, Liu, X, Meng, F-Y, Wu, Q, Lee, J-C, Xu, J-F, Wang, C & Kim, N-Y 2014, 'Design of a Compact Planar Rectenna for Wireless Power Transfer in the ISM Band', *International Journal of Antennas and Propagation*, vol. 2014.

Zhou, W 2015, 'Autonomous smart antenna systems for future mobile devices'.